

Hydrodynamic analysis for the *Undaria pinnatifida* (Wakame)

Technische Universiteit Delft

Rui Zhu

Hydrodynamic analysis for the *Undaria pinnatifida* (Wakame)

by

Rui Zhu

to obtain the degree of Master of Science
at the Delft University of Technology,
to be defended publicly on Wednesday September 27, 2017 at 11:00 AM.

Student number: 4521137
Project duration: October 1, 2016 – September 27, 2017
Thesis committee: Prof. dr. A. Metrikine, TU Delft - Chairman
Dr. ir. A. Jarquin Laguna, TU Delft - University supervisor
Dr. F. Pisanó, TU Delft
Ir. R. Lindeboom, MARIN - Company supervisor
Ir. E. Brouwers, Noordzeeboerderij - Company supervisor

This thesis is confidential and cannot be made public until September 27, 2022.

An electronic version of this thesis is available at <http://repository.tudelft.nl/>.

Summary

With the depletion of traditional energy sources, development of renewable energy is turning into a necessity. Besides wind energy and solar energy, another alternative renewable energy is biomass. Seaweed is seen as one of the most promising marine plants that can produce the biomass needed to partly satisfy of our future energy requirements. Seaweed cultivation is deemed as sustainable and environmentally friendly because it does not need fresh water, fertilizer and agricultural land. Furthermore, it converts greenhouse gases into oxygen and uptakes inorganic nitrogen and phosphorus from the seawater to avoid eutrophication.

Stichting Noordzeeboerderij and MARIN (Maritime Research Institute The Netherlands) are working together to develop floating seaweed cultivation platforms for offshore. For this project, the loadings on the cultivation platform is interested. To accomplish this, this thesis will study the hydrodynamic characteristics of the seaweed, as they are the main contributors to the loading on the cultivation platform. Then the loading on the single blade of the seaweed is required to be predicted. In this research, two most common and highly economic value seaweed species are chosen, *Undaria pinnatifida* (Wakame) and *Laminaria saccharina*.

This thesis describes an experiment that was conducted in the TU Delft Environmental Fluid and Mechanics laboratory. In this experiment, a current flume was used to investigate the hydrodynamic coefficients for the chosen types of seaweed. Before this, the physical and mechanical features such as density, geometrical and the flexural rigidity for the algae of interest were tested in MARIN workshop. Based on these feature parameters, an accurately designed surrogate (has the same or similar magnitude of parameters with the prototype) was constructed in order to imitate fresh algae for the flume experiments. During the experiment, the behavior of *L.saccharina* was found to be characterised by complex three-dimensional movement that is heavily influenced by the chaos pattern of the surrounding flow. Because the motions of Wakame are more planar so that easier to be simulated, Wakame was chosen to be the species to be studied in detail.

Two numerical models, were written in MATLAB language, were computed for two movement phases in order to predict the loading and movement of an individual Wakame plant in a current. The first model is suitable for low velocities (0 to 0.57m s^{-1}) and simulates a swinging motion of the seaweed in the current. During this process, hydrodynamic force, hydrostatic force, friction and gravity is taken into account. The steady-state position that is predicted by the model in steady fluid is well matched with the results that were measured in the experiment in the same situation.

The second model is used for large velocities (0.57m s^{-1} to 2.5m s^{-1}), when the structure is designed to have a horizontal position as its initial position and equilibrium position. A stable motion was simulated when the velocity vary from 0.57m s^{-1} to 0.81m s^{-1} . Furthermore, when the velocity exceeds 0.81m s^{-1} , the structure experiences a flutter instability and larger loading. In this procedure, a nonconservative inviscid force that is applied on the structure tip and its influence is discussed in detail. Based on the second model, the ultimate of the total moment of the individual *Undaria pinnatifida* thallus is predicted for five typical growing phases (with different length, density and stiffness) for accomplish the purpose of this thesis.

These two numerical models could be further used on other engineering time-domain simulation software as a package to simulate and predict the movement of *Undaria pinnatifida* (Wakame) and the loads that works on it. It could be also used for other seaweed species with similar morphology by inputting stiffness, size parameters and the number of sections that separate the whole seaweed blade in the model. In this way, the motions and loads of other, similar species could also be predicted by the models.

Acknowledgments

This graduation thesis is the final step of the Master of Science Degree in Offshore & Dredging Engineering at the Delft University of Technology, which has been supported not only by TU Delft but also MARIN and Stichting Noordzeeboerderij.

I take this opportunity to express my sincere thanks to the people who encouraged me and motivated me during my thesis work and my whole Master's Program. First of all, I would like to thank my parents, Shuting and Yongqing, for their effort to help me come to Delft and pursue my Master's degrees. You always try your best to help me realize my ideal regardless of return from the beginning to the end.

Thanks to my thesis committee chairman, Prof. dr. A. Metrikine, who is always pushing me to challenge my results and thinking further and further. One of the most important things that I think you really help me improve myself is your education methods. You never tell me what exactly I should do but you always guide me to the correct direction to let me decide what I should do and more importantly what I want to do. It is totally different compared to all teachers that I met in China. Also thanks to Antonio, my university daily supervisor and congratulation for your accomplish your doctoral degree.

Thanks to my university supervisor René. Whenever I need someone to talk about my progress and ask suggestions, you are always the first guy come to me. Even once I felt lost and depression because of the pressure, it was you to comfort me on the train and encourage me to go further. Also Eef, without of you, I cannot even start this exciting project. You give me lots of information of the practical part of seaweed field. I appreciate that.

My thanks are due to my friend Yang, your professional advises and encouragement for me at the most tough time of my thesis saved me. Special thanks should also be paid to Prof. Timmermans, your recommendation on the storage of the fresh seaweed and your biology expertise support me successfully conducted the surrogate design experiment.

I would really like to thanks my friend Reinier who helped me edit the thesis in language aspect. Thanks the guys in TU Delft water laboratory, Sander, Jaap, Frank and Hans, and guys in MARIN workshop, Anton and Martin, you did your best to help me experimenting and made me feel warmly welcome. And Jan Kruijssse from De Zeeuwse Zeewierhandel who supplied me fresh and high-quality seaweeds from Zeeland. Furthermore, I would like to thank all my fellow students and colleagues in MARIN and TU Delft for your encouragement and all enjoyable time that we shared.

Last but absolutely not the least, I want to thank my girlfriend Yaxi. You have unusual ways to help me restore my confidence like your sincere praise and your long time accompany.

I could say, without even one guy who is mentioned above, I could not finish my thesis and get my Master degree. I hope all the best for all of you.

*Rui Zhu
Delft, September 2017*

List of Figures

1.1	The seaweed species of interest in this study	2
1.2	Sketch of the seaweed cultivation platform model with buoys (yellow bars) and proxies of seaweed (blue objects) held by a mooring system used by MARIN [16]	3
2.1	The concept of the SVC that includes advanced offshore biorefineries for the production of food, platform chemicals, and biofuels [25]	8
2.2	Potential for daily production of bio-energy over the world's oceans [33]	9
2.3	Typical horizontal ropes cultivation platform by [40]	10
2.4	Typical vertical ropes cultivation platform by [40]	10
2.5	Plastic cage and rope net comparison	11
2.6	<i>L.saccharina</i> blade width and length by [5]	12
3.1	Apparatus for three-point bending test	14
3.2	Mechanical analysis for three-point-bending test	14
3.3	Surrogate materials	15
3.4	Surrogate schematic	16
4.1	Photos of the flume and introduction of experiment set-up	20
4.2	Velocity distributions along the depth of the flume (The water surface is at level $-2cm$ and the bottom of the flume is at level $-37cm$ reading from paper scales)	20
4.3	Form drag and skin friction by [45]	21
4.4	Hydrodynamic forces on Seaweed and definition of the attack angle	22
4.5	Axial skin frictional drag analysis	24
4.6	Current flume results for form drag	25
5.1	Diagram of the simplify strategy and coordinates systems: The whole structure is evenly divided into n sections. For each section, it consists of a lumped mass, a rotational spring and an imaginary dashpot (the dash pots are not shown in the figure but it works at the same place of the spring). In the figure, m_i , l_i , and k_{r_i} are mass, length, and rotational spring constant for i^{th} section respectively. θ_i is the rotational angle for i^{th} section. v_c is the current direction and velocity	28
5.2	Fluid force acting on n^{th} mass. The specific meaning for each force is in the text.	29
5.3	Hydrostatic force on a cylindrical body, separated in normal and axial directions	29
5.4	The accuracy of the approximation	31
5.5	Steady-state positions comparison for different velocities	33
5.6	One group of velocity series and generated forces from experiment	34
5.7	Comparison of the measured forces and simulated forces	34
6.1	Surrogate position and movement in axial flow	37
6.2	Diagram of the simplify strategy and coordinates systems for the second phase motion	38
6.3	Vibration analysis (last section): case I: $f = 1$ (<i>i.e.</i> $F_{nc} = 0$) blue curves; case II: $f = 0$ (<i>i.e.</i> F_{nc} is maximum) red curves	43
6.4	Structure fluttering outlines observed from different velocities	44
6.5	Vibration when Case I fluttering and Case II stable	44
6.6	Maximum displacement analysis for two cases	45
6.7	Comparison of moment contributions by different forces	45
7.1	Ultimate loads on the surrogate for different velocities	48
7.2	Ultimate moment on the single blade for different growing phases in DNS	50
7.3	Ultimate forces on the single blade of <i>Wakame</i> in different growing phases in DNS	51

A.1	Surrogate of seaweed <i>Laminaria saccharina</i> (Left) <i>Undaria pinnatifida</i> (right)	58
B.1	Several groups raw data of the experiment	59
C.1	Matching between model result and experiment (Group 1)	61
C.2	Matching between model result and experiment (Group 2)	62
C.3	Matching between model result and experiment (Group 3)	62
C.4	Matching between model result and experiment (Group 4)	63
C.5	Matching between model result and experiment (Group 5)	63
E.1	Vibration of first six sections when $v_c = 0.57ms^{-1}$	69
E.2	Vibration of first six sections when $v_c = 0.70ms^{-1}$	70
E.3	Vibration of first six sections when $v_c = 0.77ms^{-1}$	70
E.4	Vibration of first six sections when $v_c = 0.80ms^{-1}$	71
E.5	Vibration of first six sections when $v_c = 0.82ms^{-1}$	71
E.6	Vibration of first six sections when $v_c = 1.50ms^{-1}$	72
E.7	Vibration of first six sections when $v_c = 2.00ms^{-1}$	72
E.8	Vibration of first six sections when $v_c = 2.50ms^{-1}$	73

List of Tables

3.1	Comparison of prototype and model sizes for two types of seaweed of interest. The describing for parameters are in text.	16
3.2	Properties of fresh seaweed and selected abiotic materials (\pm standard deviation)	17
5.1	Parameters that are used when n is equal to seven	33
6.1	Relationships among shape parameter f , nonconservative inviscid force F_{nc} and tip shape . . .	40
6.2	Simulation results at interface velocity $0.57ms^{-1}$	41
6.3	Parameters that are used when n is equal to seven in the second model	42
7.1	Morphology of <i>Undaria pinnatifida</i> for different growing phase (note: a. The numbers with superscript ‘*’ are cited from [19] b. The numbers with superscript ‘+’ are as measured in the surrogate design experiment c. The numbers with superscript ‘#’ are assumed, because of lack of information, by some specific reasons which are explained in the text)	48
7.2	Mechanical properties of <i>Undaria pinnatifida</i> for different growing phases (note: a. The numbers with superscript ‘+’ were measured in the surrogate design experiment b. The numbers with superscript ‘#’ are assumed, because of lack of information, by some specific reasons which are explained in the text)	49
7.3	Moment and horizontal force comparison of $0.2ms^{-1}$ and $0.1ms^{-1}$ (first model) and $1.25ms^{-1}$ (second model)	51
A.1	Physics parameters for tubes and tubes combinations	57
A.2	Physics parameters for plastic sheets (\pm standard deviation)	57

Contents

List of Figures	vii
List of Tables	ix
1 Introduction	1
1.1 Background	1
1.1.1 Introduction of seaweed	2
1.1.2 Introduction of seaweed platform	3
1.2 Problem statement	4
1.3 Objectives.	4
1.4 Approach	4
1.5 Roadmap of this thesis	5
2 Existing literature	7
2.1 An overview of history of using seaweed	7
2.2 Present seaweed industrial situations	7
2.3 Seaweed cultivation platform	9
2.4 Seaweed bio-mechanics and hydrodynamic characteristics	10
2.5 Summary	12
3 Surrogate design experiment	13
3.1 Experiment methodology	13
3.2 Surrogate materials	15
3.3 Parameters of chosen surrogate materials.	17
4 Flume experiment	19
4.1 Experiment set-up	19
4.2 Surrogate behavior in the current	19
4.3 Data analysis methodology	21
4.3.1 Form drag	22
4.3.2 Axial skin frictional drag	23
4.4 Experiment results	23
4.4.1 Axial frictional drag force	23
4.4.2 Form drag	24
5 Numerical model	27
5.1 The structure model	27
5.2 External forces	29
5.2.1 Hydrostatic forces	29
5.2.2 Hydrodynamic forces	30
5.3 Derivation of the equations of motion	30
5.3.1 Generated forces (moments) of the system	30
5.3.2 Application of Lagrangian equations.	31
5.4 Matching with experiment results.	32
5.4.1 Steady-state position comparison	33
5.4.2 Force comparison	34
6 Numerical model for further motions	37
6.1 The structure model	37
6.2 External forces	38
6.2.1 Hydrostatic force.	38
6.2.2 Drag forces.	39
6.2.3 Inviscid hydrodynamic forces	39

6.3	Linearized equations of motion	40
6.4	Simulation results	41
6.4.1	Interface velocity between two models.	41
6.4.2	Movement analysis	42
6.4.3	Influence of nonconservative inviscid force	42
7	Prediction of the moment on Undaria pinnatifida single blade	47
7.1	Ultimate loads on the surrogate.	47
7.2	Geometrical and mechanical properties of Undaria pinnatifida for typical growing phases	48
7.3	Ultimate loads on Undaria pinnatifida for different growing phases	49
8	Discussion and conclusion	53
8.1	Discussion	53
8.2	Main conclusions	54
8.2.1	Hydrodynamic coefficients	54
8.2.2	Two numerical models.	54
8.2.3	Influence of nonconservative force	54
8.2.4	Prediction of the ultimate moment and loads on Undaria pinnatifida	55
A	Physics parameters for surrogate materials	57
B	Raw data from the experiment	59
C	Matching between model results and experiment results	61
D	EOM derivation by Lagrangian mechanics	65
D.1	Lagrangian mechanism for the first model	65
D.2	Lagrangian mechanism for the second model.	66
E	Vibration graphs for all sections	69
F	User guide and the script of models	75
G	Notation and acronyms	87
	Bibliography	91

Introduction

1.1. Background

Seaweed is the most promising marine plants that will significantly contribute to the future of human beings. Its products have a broad range of usefulness, such as human food, animal feed, medicines, cosmetics, nutrition and biomass fuel due to former research that has been done by [12] and [16]. Seaweed cultivation is deemed sustainable because it does not require fresh water, fertilizer, agricultural land, nor even human care during the growing process. Furthermore, marine plants are seen as environmentally friendly energy resource because they convert the greenhouse gas CO₂ into oxygen through its efficient photosynthetic systems. The absorb of CO₂ increase pH level in the water according to [6]. Additionally, it uptakes inorganic nitrogen or phosphorus (which potentially cause eutrophication at sea) and produces valuable biomass. Because of these benefits, the demand for sustainable seaweed production is increasing rapidly, and also the need for improving the efficiency of macroalgae cultivation.

In recent years, a Seaweed Value Chain (SVC) has been developed significantly according to [16]. This is a method that support seaweed cultivation from planting to selling. It specifically consists of six steps: cultivation, harvesting, transport, storage, biorefinery and applications of the consumer products. All components are essential in the SVC, but in this thesis, I will focus on the cultivation part. In the past, seaweed was commonly planted in marine agriculture farms in shallow water along the shoreline and harvested by hand. Particularly in Asia, the main production area for seaweed, this is still done even now. However, due to the increase in the occupancy rate of the coastal zone, algae cultivation tends to move offshore where space is not an issue. As a result, for algae culture offshore, seaweed farming platform is required to hold the plants and keep them in place instead of floating away. Implied by [12], nowadays, most of the algae platforms are built based on floating mooring buoys or other simple floating structures. Seaweeds are fixed on ropes which are connected between platform floaters by its holdfasts or held by cage shape carriers on the platforms.

In order to archive and improve SVC by means of increasing algae production or harvesting speed, more and more companies have been founded and a large amount of research has been conducted in recent years with regard to cultivation of seaweed. Stichting Noordzeeboerderij is one of the companies that work on sustainable seaweed cultivation at sea. They are also one of the sponsors for this thesis, as their aim to research the loading on the cultivation platform which includes the direct fluid loading and loading transfer from cultural seaweeds. Furthermore, MARIN (Maritime Research Institute The Netherlands) is a maritime research company that famous on its hydrodynamic research and maritime technology. They are also interested in seaweed cultivation offshore recently so that they are investing in this thesis for the same purpose as Stichting Noordzeeboerderij.

At the same time, research was carried out in universities and institutes, for example, by [4] on the study of drag coefficients of *Laminaria saccharina*, [12] on the investigation about macroalgae biomass technological achievements and challenges, and [15] on the research about impingement forces on cultured *Egria menziesii* (Turner) based on a field experiment method. Further research on various aspects of various algal species such as [18], [23], [25] and [40] will be introduced in Chapter 2.

1.1.1. Introduction of seaweed

Seaweed is usually known as a large algae. It is a multicellular marine plant that includes some types of green, red and brown algae. More than 10,000 types of seaweed are discovered in all the oceans of the world [43]. In this thesis, two most common species of seaweed are studied, *Undaria pinnatifida* and *Laminaria saccharina*. They are both common species of marine plant that have high utility value and wide range usefulness. This section mainly develops their distribution, the values of these two types of algae and their normal morphology.

- ***Undaria pinnatifida***

Undaria pinnatifida which is also known as Wakame is a most common seaweed species which widely distributed around the world. It consists of three parts, a quite stiff stalk which throughout the whole body, a strong holdfast at the base and thin leaves. A simple illustration of Wakame morphology is shown in Figure 1.1a. The stalk of Wakame is usually stiffer than its leaves, especially on the base part close to the holdfast. On the other hand, leaves are soft and pliable but flat. The aspect ratio (length-to-width ratio) of matured Wakame is around 6.52 (from the experiment that described in Chapter 3) and length up to 2m.



(a) *Undaria pinnatifida* (Wakame).
Photo source: [7]



(b) *Laminaria saccharina* (Sea belt).
Photo source: [3]

Figure 1.1: The seaweed species of interest in this study

Studies conducted at Hokkaido University have found that a compound in Wakame known as fucoxanthin can help burn fatty tissue such as [27]. This feature is in line with the needs of modern human beings. On the other hand, Wakame is a rich source of eicosapentaenoic acid, an omega-3 fatty acid which is good for health reported by [21].

Wakame leaves have a crispy texture and are favored by a bewildering amount of people all over the world. It is usually boiled and cooked to be served in salad or soup. From my own experience, The price of Wakame salad is three times and two times higher than the common salad vegetables (such as lettuce and carrot) in the supermarkets in Netherlands and China respectively. This implies popularity and short supply.

- ***Laminaria Saccharina***

Laminaria saccharina belongs to the brown macroalgae (Phaeophyceae) and is also known under its common names 'Saccharina latissima', 'sea belt' or 'sugar kelp'. It is found on rocks and stones located in the inter-tidal zone in the northeast Atlantic Ocean, Barents Sea and south to Galicia in Spain. The species is also found in the open North Sea because the cold water temperature there is preferred by

the kelp. It also contains three parts, a tiny but powerful holdfast, a thin, smooth, flexible stem and a wave shape, narrow and undivided leaf with the brown color shown in Figure 1.1b. It can grow up to 220cm in length, and the aspect ratio is around 5 in its final growth phase reported by [5].

Major constituents of high value in *L.saccharina* are carbohydrates and mannitol base on research [1]. They can be up-taken by drying, powdering and extracting. Mannitol is a water-soluble sugar alcohol used in medication. For example, base on the first research [44] in this aspect, it plays a fundamental role in decreasing intraocular pressure for glaucoma patients. It also has a broad use for food industry as sweetener such as [29] mentioned that it is the main sugar alternatives in food and beverages.

1.1.2. Introduction of seaweed platform

The cultivation platform which is recently widely used for planting both of these two species of seaweed in the offshore environment will be described and sketched here. In general, an offshore seaweed cultivation platform is designed based on the living characteristics of different species of seaweed. Almost all of the farming platform in offshore are based on a floating structure with mooring systems referenced by [12], but the carriers for the algae are different. The most common carriers include I. horizontal ropes II. vertical ropes III. cages and IV. rope nets.

The horizontal ropes are suited for seaweed species that are highly dependent on sunlight. All points in a horizontal setup lie close to the water surface, exposing the plants to sufficient amounts of sunlight. On the other hand, seaweeds like *Palmaria palmata* are planted on vertical ropes, in order to more efficiently use the available space. Cages and rope nets suit for the seaweed which without holdfast such as *Ulva* and *Gracilaria tikvahiae*. The rope net is lighter and decreases the loading on the platform. This makes it a more popular solution than plastic or steel cages. But one of the advantages of cages is its excellent protection against attacks by marine animals. More introduction and pictures or advantages and disadvantages of different platform carriers are discussed in Section 2.3 based on existing literature.

The seaweed cultivation platform which is considered into this thesis is based on a mooring system with horizontal ropes because two algae species that interested in this thesis like sunlight (or at least not against sunlight) and have their strong holdfasts. Figure 1.2 shows the model of the type of cultivation platform that was used by MARIN for the experiment. The yellow bars in the figure are buoys which are held by a mooring system. The blue objects are plastic plates or sheets which function as the surrogate imitating seaweeds during the experiment. They were fixed on the horizontal connecting ropes between buoys. In nature, seaweeds will fix themselves on ropes by taking advantage of their holdfasts.

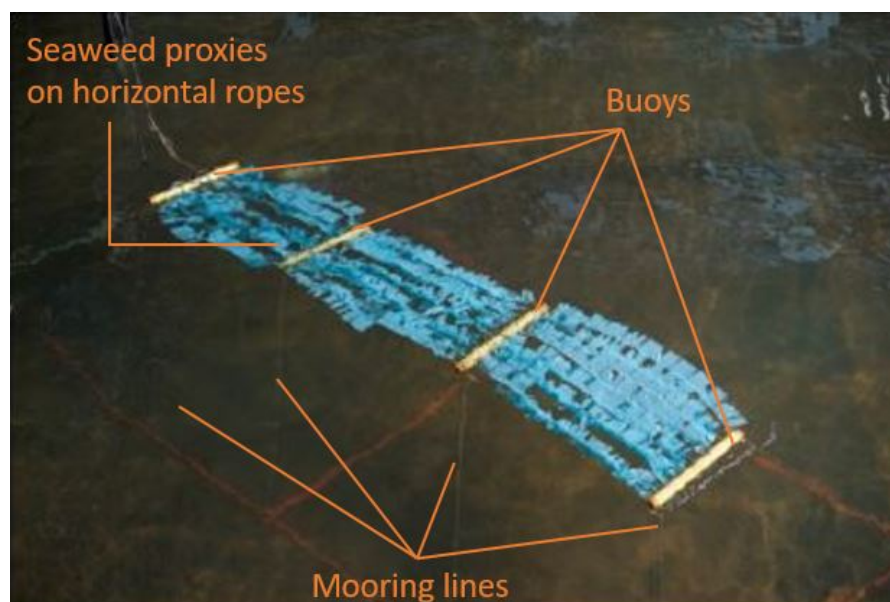


Figure 1.2: Sketch of the seaweed cultivation platform model with buoys (yellow bars) and proxies of seaweed (blue objects) held by a mooring system used by MARIN [16]

1.2. Problem statement

As we explained above, the agricultural platform is a fundamental part of seaweed cultivation. To guarantee successful harvesting, the stability of the platform is necessary to be studied. Effects such as motions and the loading of seaweeds due to the interaction with currents or waves, might significantly influence the motions and stability of the platform. Therefore, this influence is become important if one wants to study the stability of the cultivation platform. How great the loading on the platform that is transferred from the seaweed is and what kind of movement does algae have in the fluid are two aspects that interested by our sponsor Stichting Noordzeeboerderij and will be answered in this thesis.

However, studies about the physical and hydrodynamic features of individual seaweed thallus alone is not sufficient but it is a vital for study the influence that is mentioned above. The researchers in [8] inferred a new drag equation which has invariant constants that makes it not be affected by the attack angle or the velocity change. Some research of seaweed hydrodynamic characteristic using a field experiment method has been done for different species of macroalgae such as [5] and [15]. But the hydrodynamic characteristics for seaweed species which wanted for their high economic values are not sufficiently studied. Examples of these species are the two popular kinds of algae that we have presented above. On the other hand, when we completely revise the features of individual algae thallus, we need to design a numerical model to simulate their movements and foresee their loadings. Then this model would be expected to be an additional package that can contribute to the prediction of the movement of the farming platform when we associate it with the entire platform model.

1.3. Objectives

One of the objectives is to address. The hydrodynamic characteristics by means of describing hydrodynamic coefficients of the two types of seaweed that mentioned above are required. In this process, the physical features like density and morphology size for the algae of interest should be tested. Based on these feature parameters, it is expected that a suitable surrogate will be designed and constructed in order to imitate fresh algae for the potential flume experiments.

Next, a numerical model is required to develop a simulation of an individual seaweed plant's movement in the experiment. To achieve this, the force applied on the simulated body must be clear. This may include hydrodynamic force, hydrostatic force, friction, gravity etc. During this process, a nonconservative inviscid force that is applied on the structure tip should be studied in detail.

In the end, through the model, the total moment and loading on the individual seaweed is expected to be predicted for achieving the target of Stichting Noordzeeboerderij.

1.4. Approach

The surrogate needs to be designed firstly. Based on a theoretical study [37], a three-point-bending test is the most appropriate method for measuring the bending stiffness for the chosen seaweed species. In addition, the same approach must be implemented on surrogate materials such as plastic sheets and silicon tubes. Combining all selected materials together will build a proxy with a good resemblance to the actual seaweed. This experiment will be fulfilled in MARIN workshop with a perfect and wide range of tools and accurate measuring equipment.

Hydrodynamic characteristics will be studied through an experimental method in Delft University of Technology (TU Delft) Environmental Fluid and Mechanics Laboratory. A current flume is used to generate a uni-direction fluid with different velocities in the experiment. During the test, the surrogate will be hanged in the flume instead of fresh seaweed. The force and velocity sensors will be mounted in appropriate positions to record the experiment data. After this, the hydrodynamic coefficients will come from two derivation approaches. One is used by previous research, and another one is a new approach. In the end the results from both will be compared.

We expect to find two phases of motion for the surrogate in the current: one for a small velocity and one for a larger velocity situation. Both movement phases need a numerical model respectively. For the aim structure, the surrogate in the experiment, the equations of motion will be deviated by the Lagrangian method. The coordinate angle for the first model is θ which is likely to be a big angle that can not be linearized, but for another for second motion phase, φ is considered as a small angle. In order to be able to solve these equations, we chose to use MATLAB ordinary differential equations solver, specifically, ODE45 solver. Theoretically, this solver calculates the displacements, velocities, and accelerations for each time spans and

they will be used again as an input for the computation of the next time interval. Once we get the simulation result, we can validate the reliability by matching with the experiment values.

1.5. Roadmap of this thesis

The points described above includes objectives and approaches are elaborated in detail in the following chapters. To be specific, in this thesis, the reader is guided from the review of the existing literature in order to have a first sense of the history and the present development of the seaweed industry, as well as the previous valuable research on algae in Chapter 2. Chapter 3 shows the design experiment for the surrogate, including the apparatus features, calculation methods and results for seaweed physical characteristics, coupled with Appendix A. The current flume experiment that was conducted in TU Delft's fluid laboratory and was aimed at testing the hydrodynamic coefficient is described in Chapter 4. After this, Chapter 5 goes into detail on the design and validation for the first motion numerical model, associating with Appendix C. Chapter 6 describes another model for the second phase movements and analyzes the influence of the nonconservative inviscid force. After that, Chapter 7 shows the prediction of the ultimate loads on a single blade of the plant in current. The thesis finalizes with discussions, and the main conclusions are presented in Chapter 8.

2

Existing literature

This chapter will offer a quick overview of the existing literature related to seaweed cultivation platform, seaweed bio-mechanics and seaweed hydrodynamic characteristics. First of all, an overview of brief history of the use of seaweeds will be introduced resourced from Wikipedia and some anonymous articles. In the second section, an introduction of existing literature of present seaweed industrial situations are shown. After that, a summary of the common seaweed cultivation platforms are described in detail for the extended of the same content in Chapter 1. Then the existing research of seaweed hydrodynamics and seaweed bio-mechanics are introduced.

2.1. An overview of history of using seaweed

Seaweed is using as food for the first time has been tracked back to the fourth or fifth century A.D in China and Japan. According to folk legend, seaweed was used for hemostasis in China even in B.C. years. Gradually, eating sea-grass has spread across East Asian, such as the Korean peninsula. After that, seaweed consumption spread to South Asia countries like Thailand, Indonesia, and Vietnam. Since then, eating sea plants has gotten more and more popular around the coastal area in Asia. In the beginning, fishers ate seaweeds to replace vegetables, to decrease hunger, or increase the flavor of other food. Progressively, they started treating sea kelp as one of the indispensable parts for their daily diet.

As people from countries of East Asia or South Asia immigrate to all parts of the world, seaweed has been accepted by more people in different countries as food. According to [28], the demand of sea-grass for food over last fifty years increase rapidly in the United States of America and South America.

Today, people believe seaweed is not only valuable as food but also by its therapeutic application. Brown seaweeds are used to extract sugar, agar, alginate, mannitol, and carrageenan. Mannitol was introduced in Chapter 1 for decrease eyes pressure. Alginate is a water-insoluble substance that can be used for entrapment of enzymes and to form artificial seeds in plant tissue culture. Carrageenans, which are broadly utilized in the food industry, was firstly used by Chinese around 400 B.C, fulfilling their gelling, thickening, and stabilizing properties to meat products and care products such as dentifrice and shampoo.

2.2. Present seaweed industrial situations

As described in Chapter 1, global population growth and needs for higher quality of life boost our need for the development of clean energy and new food resources. Seagrass fullfills these requirements because of its marine-botany characteristic: it does not need for fresh water or land resources. Furthermore, it transfers greenhouse gases to oxygen, generates biomasses for application on human food, animal feeds and even biomass fuel by [12]. Seaweed cultivation and application is a promising industry that has been developing recently. Except [12], [25] and [28] are two typical research for the present development.

According to the works of [28], a total annual value of seaweed production is estimated at almost 6 billion US dollar. Out of this, 5 billion US dollars is present for food products of human consumption. The industry uses approximately 8 million tons of wet seaweed annually, which is harvested from both natural growth and farming seaweed, for pharmaceuticals and health care products. He pointed out that China is the largest manufacturer of seaweeds for usage of food now, to be specific, harvesting about 5 million wet tons per year. The biggest part of this is for kombu which from the family Laminariaceae (same as our interested species

Laminaria saccharina). South Korea plants around 800,000 wet tons of three different species. About 50 percent of this is brown macroalgae *Undaria pinnatifida* (Wakame) which is another interesting species in this thesis. Their neighbor Japan, also one of the most important countries in seaweed industry produces approximately 600,000 wet tons and most of them are *Porphyra* (Nori). Nori is a high-value product and used as one of the raw materials for seaweed sushi and soup. Its economic value is increasing because of its popularity which is about USD 16,000/dry ton, compared to kombu at USD 2,800/dry ton and Wakame at USD 6,900/dry ton.

In addition,[28] mentioned Norway is the first country in Europe to collected, dried and milled seaweed into the powder which is used as an additive to animal feed in the 1960s. After that, more and more countries in Europe, especially who has coastal lines of Mediterranean such as France and Spain or Atlantic ocean like Netherlands, United Kingdom, and Germany investing an enormous amount of money into seaweed cultivation offshore to reduce the pressure of land shortage.

Some scientists like [25] did some research for the potential of macroalgae biorefinery using a metabolism and growth rate model for *Ulva* genus. Some of his theories are excellent supplementary for describing the SVC in Chapter 1. His graph shown in Figure 2.1 is clearly demonstrated all steps in SVC. Seaweed is planted on ropes offshore and harvested by a robotic crane on the platform. New technologies nowadays guide engineers install biorefinery facilities on the platform which allows converting raw seaweeds to food, biofuels, and other applications immediately after harvesting. Then, the harvested seaweed is transported by ships to nearby harbors, and then into markets. In this procedure, not only renewable energy has been produced but also jobs opportunities are created. However, SVC shown in this graph is an optimized plan based on advanced refinery technologies which are not fully achieved in the present. In most of the European countries that are interested in seaweed industry, building a biorefinery on-shore is currently the best choice.

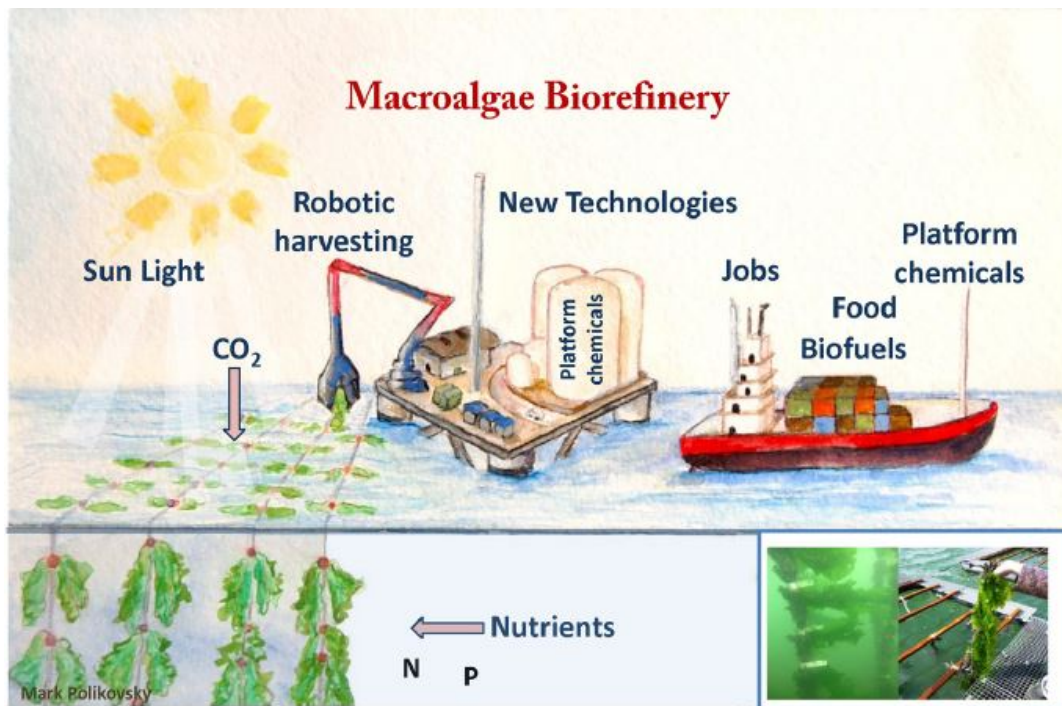


Figure 2.1: The concept of the SVC that includes advanced offshore biorefineries for the production of food, platform chemicals, and biofuels [25]

From his paper, [25] also predicted the potential for daily production of bio-energy over the world's oceans by taking an optimum biomass stocking density for *Ulva* genus of 4kg m^{-2} which is suggested by [33]. Specific daily production distribution is shown in Figure 2.2, where we can see that highest production rate is located in South Pacific Ocean and South Atlantic Ocean near Namibia. Additionally, North Pacific Ocean, South part of Norwegian Sea and North part of Celtic Sea has decent production rate per day as well. Bioenergy production values will change if one considers a different stocking density or other species of seaweed with

different living habits in the simulation.

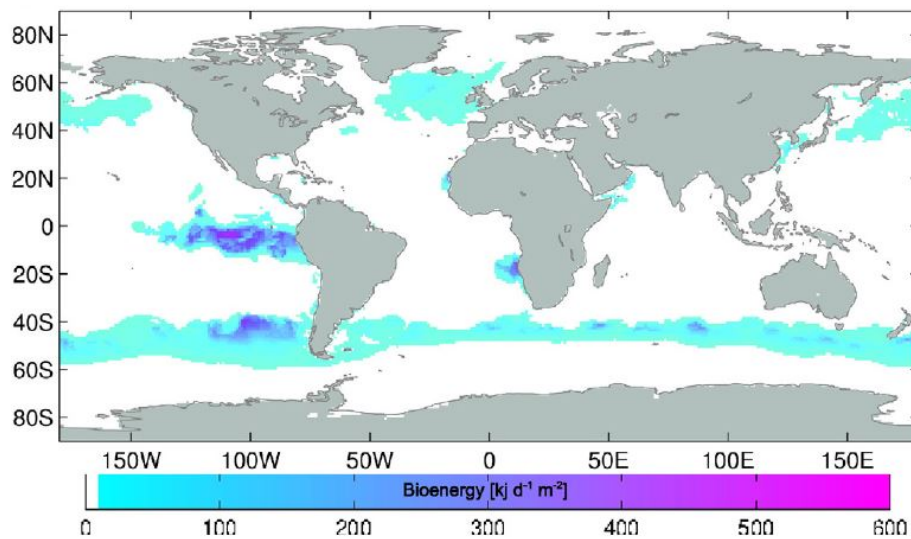


Figure 2.2: Potential for daily production of bio-energy over the world's oceans [33]

This research gives us a basic perspective of the potentiality of the seaweed industry. As 4 kg m^{-2} stocking density, the global theoretical production is forecasted as 10^{11} dry ton annually, which is equal to generating 2052 EJ per year. It means that the biomass produced by seaweed has the potential to provide some of the basic products required for human society in the coming decades includes entire displacing the use of fossil fuels in the transportation sector summarized by [25] in the end.

From previous studies listed above, seaweed industry is well developing not only in the Asia countries of origin, but has also become popular in other parts of the world in the past 20 years. Although the technologies in the present for advanced biorefinery is not perfect, and it is not possible to farm seaweed across the world like in simulations [25], we can still be impressed that the promising of seaweed cultivation to the future.

2.3. Seaweed cultivation platform

Seaweed cultivation platforms are mostly based on a floating structure offshore. The four main types of cultural platform that were mentioned in Chapter 1 will be discussed in detail, including their advantages and disadvantages based on existing research by [23] and [40]. As we already discussed in the last chapter, almost all of the farming platforms now based on mooring systems with buoys and cultural lines, but the carriers for the algae are different. The most common carriers include I. Horizontal ropes II. Vertical ropes III. Cages and IV. Rope nets.

Two floating rafts with horizontal (Figure 2.3) or vertical culture ropes (Figure 2.4) respectively were used in [40] experiment to figure out (1) the most suitable season for *Undaria pinnatifida* planting as well as (2) the most appropriate cultivation methodology to the chosen species at North Western Atlantic coast near Galician. From his experiment relative results and other scientists research such as [18], [31] and [41] suggested, we could summarize a comparison between two farming methods.

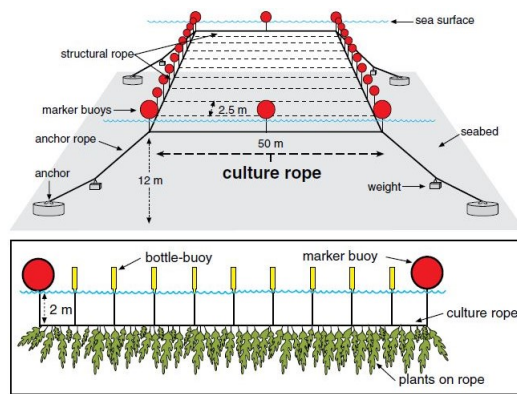


Figure 2.3: Typical horizontal ropes cultivation platform by [40]

II. Vertical ropes cultivation platform

Advantages

- Vertical ropes can increase the tension in the rope which will enhance water movement around sporophytes [31].
- Easier assembly compared to horizontal ropes [40].
- Seaweed nutrient and carbon dioxide uptake faster because water movement around the platform reduces the diffusion boundary layer [18].

Disadvantages

- Light on the rope is less due to the increasing depth, which causes biomass production difference for seaweeds growing in different depth [40] [41].

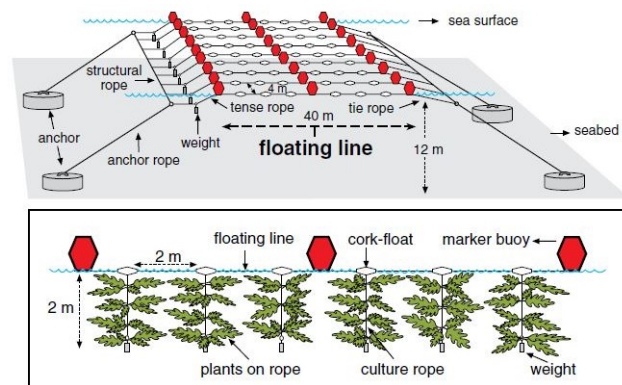


Figure 2.4: Typical vertical ropes cultivation platform by [40]

Cage carriers are commonly used for macroalgae which do not have holdfasts such as red edible algae *Gracilaria tikvahiae*, *Ulva rigida* (Sea lettuce) or *Ulva prolifera*. Recently, [23] carried out an experiment to study the growth rate of *Ulva* and *Gracilaria* by plastic cage carriers attached to the fish net in Israel, as shown in Figure 2.5a. Differently, cages also be hooked on horizontal lines or other types of platforms in some marine farms. For cage carriers, its solid surface supplies a perfect and secure living space to non-holdfast sea plants to growing without interference by other marine animals. On the other hand, small cages like Figure 2.5b showing will make an easy harvesting process.

Rope nets for carrying sea plants is described by [26] in Figure 2.5d for the cultivation of *Porphyra yezoensis*. An aquaculture raft, which consists of ropes and bamboo poles, was used here. Compared to a cage, a rope net is convenient to produce, and lighter. However, it is suitable only for calm water.

2.4. Seaweed bio-mechanics and hydrodynamic characteristics

Biomechanics is the field of study that investigates the structure of biological systems such as animals or plants through mechanics methods. [32] is the representative study among research of plant mechanics. It mainly deals with the effect of geometry on mechanical behavior. Engineers generally focus on the geometry, size, material properties and loading conditions of the structure to simplify them as ideal beams or columns. However, for plant organs, they can not be considered as ideal members because their morphology is normally heterogeneous and changes all the time. Thus, [32] studied the applicability and limitation of traditional mechanical formulations on plant bodies. One of the contributions from [32] to our research is the

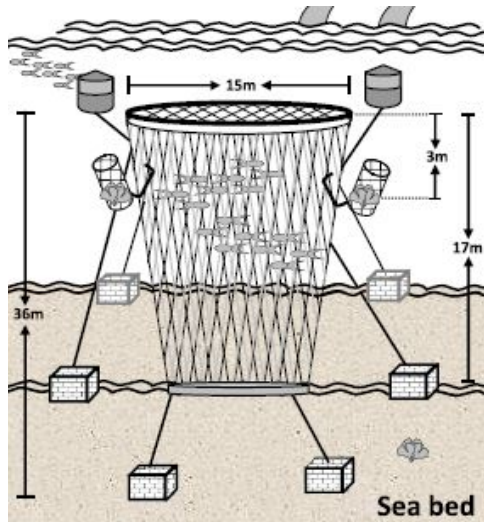
I. Horizontal ropes cultivation platform

Advantages

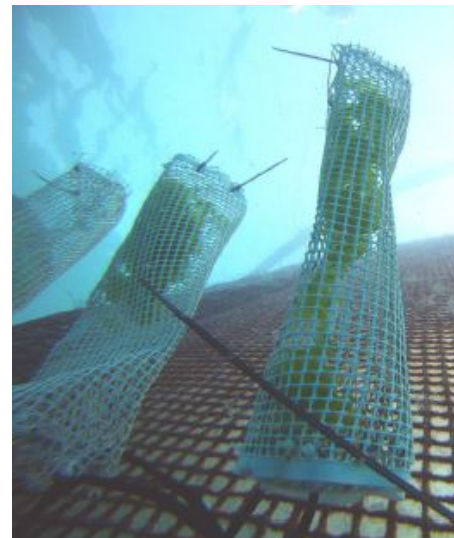
- Decrease the available substrate along the rope to preventing fouling by large and epiphytic seagrass which will effect biomass production of farm [40].
- Increases sporophyte density [40].
- Lower total rope length requirement [40].

Disadvantages

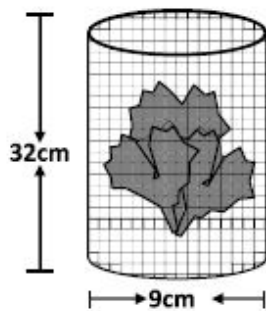
- Only or be more suited for exposed areas (offshore) because of its long lines [40].



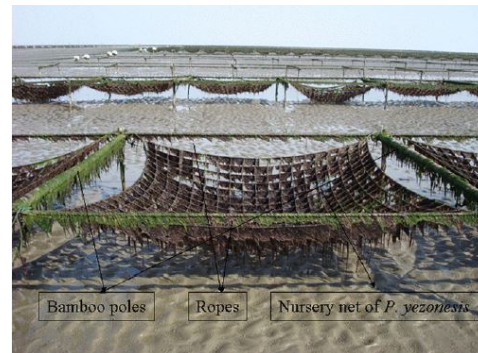
(a) Sketch of the fish cage (large one in the middle) and the algal culture cages (small ones that hooked on the fish cage) by [23]



(b) Photo of algal culture cages (small cages in 2.5a) on fish net in Israel by [23]



(c) Sketch of an algal culture cage (small cage in 2.5a) by [23]



(d) Rope net with bamboo poles cultivation platform by [26]

Figure 2.5: Plastic cage and rope net comparison

suggested method for calculation of the flexural rigidity of plant organs. When one performs a three-point-bending test for a solid body such as steel bar or concrete to trial its flexural, the sample is placed on two supporting pins. But for plant organs, a soft and flexible body, both ends of the samples should be clamped for the stability of the sample during application of force. Clamped ends are different, which will result in additional shear and tensile stresses which influence the calculation of bending modulus of the body. [32] suggests that for deflections less than 10% of cantilever length, these two stresses can be neglected so that beam theory is applicable. This finding has been used in the surrogate design for the experiment, which will be discussed in Chapter 3.

Seaweed hydrodynamic characteristics have been studied by researchers over the past two decades for several species. Most of their works follow the experimental method in different bays of the world, with advanced apparatus to record plant's growth and their applied forces. From these studies, [5] is one of the studies that investigated the response of cultivated or wild *Laminaria saccharina* in the North Sea. The derivation of the drag coefficient is a key step in describing the hydrodynamic characteristics of the objective body, which is why it was included in that study.

In [5], the morphology of the plant was analyzed by measuring large quantities (1300 thallus) wild and cultured *L.saccharina* samples from the German North Sea region near Enlarged island of Helgoland. The blade length and width relationship are showing on Figure 2.6, where functions for the different growing phase of the plant are separated. The last growing phase is the reference that we consider in this thesis when the aspect ratio of *L.saccharina* is around 5.

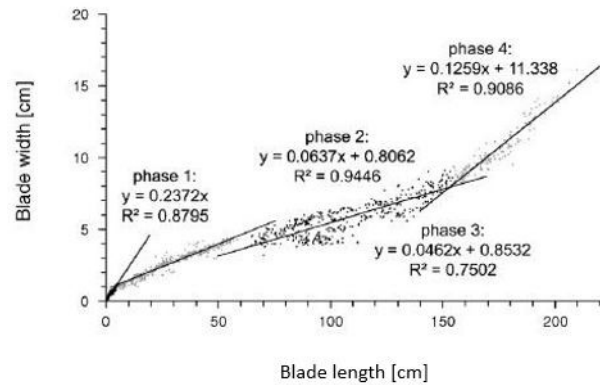


Figure 2.6: *L.saccharina* blade width and length by [5]

After this, [5] used some samples for the coefficient test that using a towing tank. In order to generate a unidirectional flow, he mounted seaweed samples on a drop-like shape beam on a towing tank which applied a uniform motion with known velocity (v). As suggestions from [14], [22] and [42], [5] used the full frontal area (A_a) of the thallus to calculate the drag coefficient ($C_d = f(A_a, v^2)$) for flexible plants. In the end, the results were figured out for drag coefficients not only for individual thallus but also for bunch groups. For the cultivated samples, the drag coefficient is around 0.05 when the current speed is equal to 0.5 m s^{-1} and it remains constant with approximately 0.025 at velocity larger than 1 m s^{-1} because of the reorientation of the algae body into a streamlined shape. Furthermore, the coefficients for the same shape wild samples are four times larger than the cultured one. Additionally, whether samples are tested by a bunch or not, the resultant coefficients are influenced. This study [5] compared all kinds of influences on the drag coefficient, such as sample sources (wild and cultivated) and the effect of bunch samples. In our research, we decided using projected area for each phase of motion for the interested algae to calculate the drag coefficients. However, we will also use the same method by him as a reference to analyze which one is preferable.

2.5. Summary

The existing literature and research related to seaweed also contains the aspects of biology, nutrition, environmental science, etc. but they are not introduced here. As we discussed in this Chapter, the development of seaweed industry is moving forward rapidly with great promise. Still, we have a long way to optimization and improvement. An example is integrating biorefinery technology on the offshore platform.

The previous research of biomechanics and seaweed hydrodynamic characteristics like described above do not entirely answer the question of the features of the seaweed species of interest in this thesis. However, not only their results but also their suggested methods will be referred to this thesis, such as the suggestion by [32] for the calculation of flexural rigidity and morphology information from [5].

3

Surrogate design experiment

The loading on the planting seaweed is the aim to investigating in this research. The most important loading is contributed by drag force. Thus, seaweed drag coefficient is a parameter that needs to be tested in this research to describe the drag force on plant body. Additionally, behaviors of seaweed in a current need to be tested and observed because these could then be used as a reference when simplifying the algae body to a simple model and then simulated numerically. To achieve these, it is necessary to design a surrogate to imitate the plant in the flume experiment.

When one is investigating or analyzing the interaction between aquatic organisms and the hydrodynamic environment, it is often necessary to use surrogates instead of the prototype organisms. Especially when one cannot keep living organisms for the duration of the experiment or the organisms have no time to acclimatize in the flume set up, suggested by [39]. Additionally, using surrogate is allow the morphology of organisms to be simplified and avoids concerns about organism husbandry [13]. In our case, in the laboratory flume, only the fresh water is available, but most of the marine plants cannot be kept alive in lower salinity water even in short test duration. This means that in the fresh water, macro-algae will almost certainly not show the same characteristics as in sea water. Consequently, an abiotic surrogate should be designed and produced to imitate seaweed during the experiment.

Therefore in this chapter, the method of measuring physical characteristics of seaweed is elaborated, and the designed surrogates are described. Specifically, the seaweed properties such as geometry, density and bending stiffness of the sea-grass are listing in tables. This experiment was conducted in MARIN workshop.

3.1. Experiment methodology

There are two types of seaweed that have been chosen in the surrogate design experiment, *Undaria pinnatifida* (Wakame) and *Laminaria saccharina*. First of all, separately collected 5 – 10 specimens of different kinds of seaweeds from Dutch North Sea near Zeeland and analyzed for their physical properties in the laboratory within 48h of the collection. During this measuring period, the macro-algae were stored in large net bags which supply favorable ventilated and salt moisture environment by putting in the ice bags and few salt water to keep the seaweed fresh. The net bags were placed in the refrigerator when not being used and samples of the experiment were kept under damp cloths between tests.

The seaweed thallus are divided into many pieces as specimens. To be specific, stalks were used in 15cm per piece, segmented from the base to the tip of the seaweed. Leaves were cut into strips of 15cm long and 5cm wide. First of all, we measure the morphology size for specimens. It is worth mentioning that, for individual seaweed thallus, the morphology is inhomogeneous, but for the specimens which are small pieces that cut from the plant, the degree of heterogeneity decrease. Therefore, for simplification, the specimens using here are assumed has an even shape. Diameter (D_o, D_i), thickness(t), width(w) and length(l) of stalks and leaves were measured with a caliper gauge with the precision of $\pm 0.01(mm)$. Each specimen was dried to remove excess water before the test and weight it as m with a precision of $\pm 1(g)$ using scales. One may calculate the density of the stalks by Equation 3.1. It is worth noting that, when we are computing the density of the whole blade, the best method for obtain the volume is to measure the volume change (ΔV) after we put individual thallus in measuring bottle with appropriate amount of water.

$$\rho = \frac{m}{V} = \frac{m}{wlt} \quad (3.1)$$

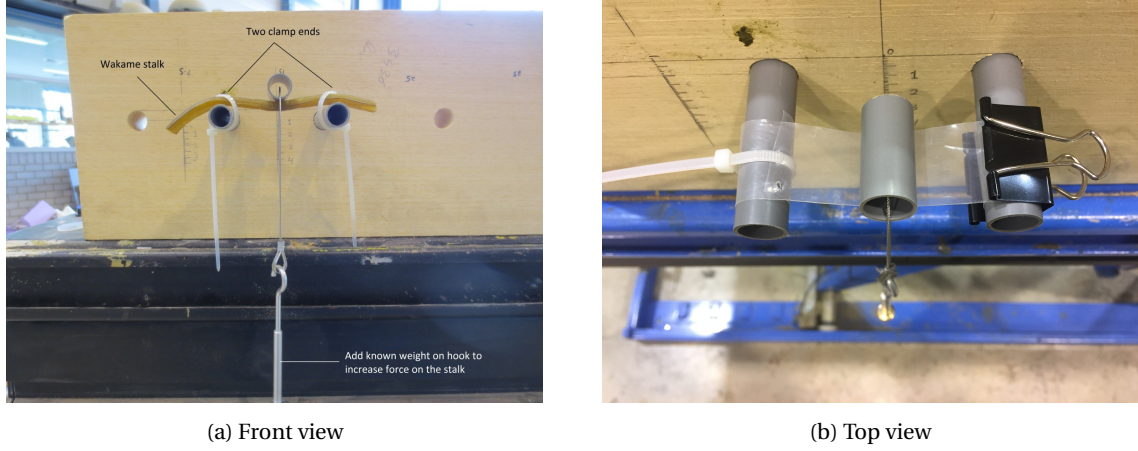


Figure 3.1: Apparatus for three-point bending test

In order to quantify the stiffness of kelp, a three-point-bending test was performed for stalks and leaves separately. Samples are clamped horizontally between two thin PVC pipes and the distance between them is 7.5cm . A ring shape device to apply force at the center of the sample was mounted. To increase force, known weights were hanged on the ring. The deflection by the scale on the background was also recorded. The experiment apparatus is shown in Figure 3.1.

During the experiment, the flexural rigidity (J) was derived according to beam theory for a cantilever. As Figure 3.2a showing, the deflection δ_{max} of a cantilever beam is defined by

$$\delta_{max} = \frac{Pl^3}{3EI} \quad (3.2)$$

where l is the cantilever beam length, P is the applied force, EI is bending modulus of the beam. For experiment situation, it needs to calculate the deflection δ_{max} in the middle of clamped-clamped beam (as shown in 3.2b), the equation may be written as Equation 3.3

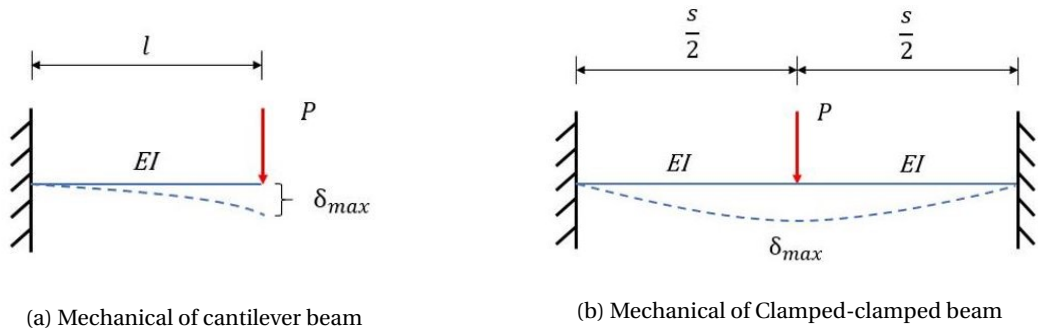


Figure 3.2: Mechanical analysis for three-point-bending test

$$\delta_{max} = \frac{(\frac{P}{2})(\frac{s}{2})^3}{3EI} \quad (3.3)$$

Therefore the flexural rigidity J could be defined as Equation 3.4 if the deflection is smaller than 10% of cantilever length suggested by [32].

$$J = \frac{(\frac{s}{2})^3 P}{6h} \quad (3.4)$$

Where s is the distance between clamped ends of the sample, P is the applied force and h is the resulting vertical deflection. Furthermore I is the area second moment of inertia, and E stands for the bending modulus which can be easily computed by flexural rigidity divided by area second moment of inertia.

The shape of the cross-section of the seaweed stalk is assumed as a regular ellipse. The major radius a is the half of the stem width and the minor radius b is the half of the stalk thickness. Then the inertia of moment I_e of an ellipse is calculated as:

$$I_e = \frac{\pi}{4} ab^3 \quad (3.5)$$

The shape of the leaf's cross-section is a rectangular, if w is the sample width and t is the sample thickness, the inertia of moment of rectangular I_r is showing as:

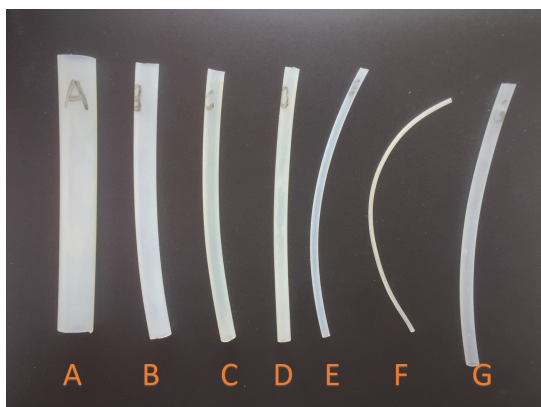
$$I_r = \frac{wt^3}{12} \quad (3.6)$$

The shape of the cross-section of the silicon tube (as a surrogate of the stalk) is a hollow and circular, the inertia of moment of it I_c is derived as below, where d_0 and d_i is the outer diameter and inner diameter separately.

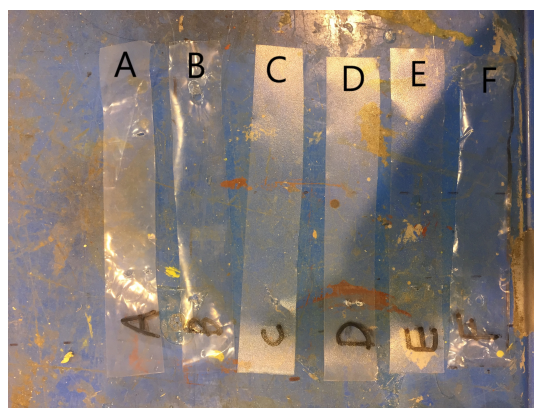
$$I_c = \frac{\pi((d_0)^4 - (d_i)^4)}{6} \quad (3.7)$$

3.2. Surrogate materials

Several types of surrogate materials were tested using the same method as applied to the fresh seaweed had been done. Basically speaking, different diameter of silicon tubes (Figure 3.3a) and plastic sheets (Figure 3.3b) are the target proxy materials for imitating stalks and leaves separately. In the test, surrogate materials are segmented as the same size as the fresh algae specimen.



(a) Target material for imitate stalks: silicon tubes



(b) Target material for imitate leaves: plastic sheets

Figure 3.3: Surrogate materials

The design strategy is to combine the most suitable materials together to build the surrogate. The plan is showing in Figure 3.4. From the results of fresh Wakame measurement, we understand that the stiffness of the stalk is similar except the base part (around 20cm) of the plant. Therefore the surrogate for *Undaria pinnatifida* (Wakame) stalk will be constructed or combined by two parts with different stiffness, part A and Part B as shown in Figure 3.4a. The stalk is built by setting up and sticking a series of flexible tubes with different diameters. Leaf part (C in Figure 3.4a) using a suitable plate-shape plastic starts from one-fifth of the blade length from the base. On the other hand, the stalk (part A) for *L.saccharina* (Figure 3.4b) is just a

short piece between the base and the leaf. Finally, some clay will be pasted on surrogates to match the density of fresh seaweed.

The aspect ratio of *L.saccharina* is around 5 for the final phase of its growing period reported by [4]. Also, the aspect ratio of *Wakame* is 6.52 from the results of the experiment for surrogate design. The handmade surrogates which will imitate real seaweed in the flume test also following these two aspect ratios. The detail sizes of the surrogate are annotated in the Figure 3.4. The comparison of prototype and model sizes are listed in Table 3.1. In the table, stem stands for the base part of the stalk, which is 5 cm for *Wakame* and 4 cm for *L.saccharina*. The sizes for the prototype are chosen of the average number of the specimens. The scale between prototype and model is 4 and 5 for *Wakame* and *L.saccharina* respectively. However, the diameter of the proxy is not follow that scale due to the limitation of the materials.

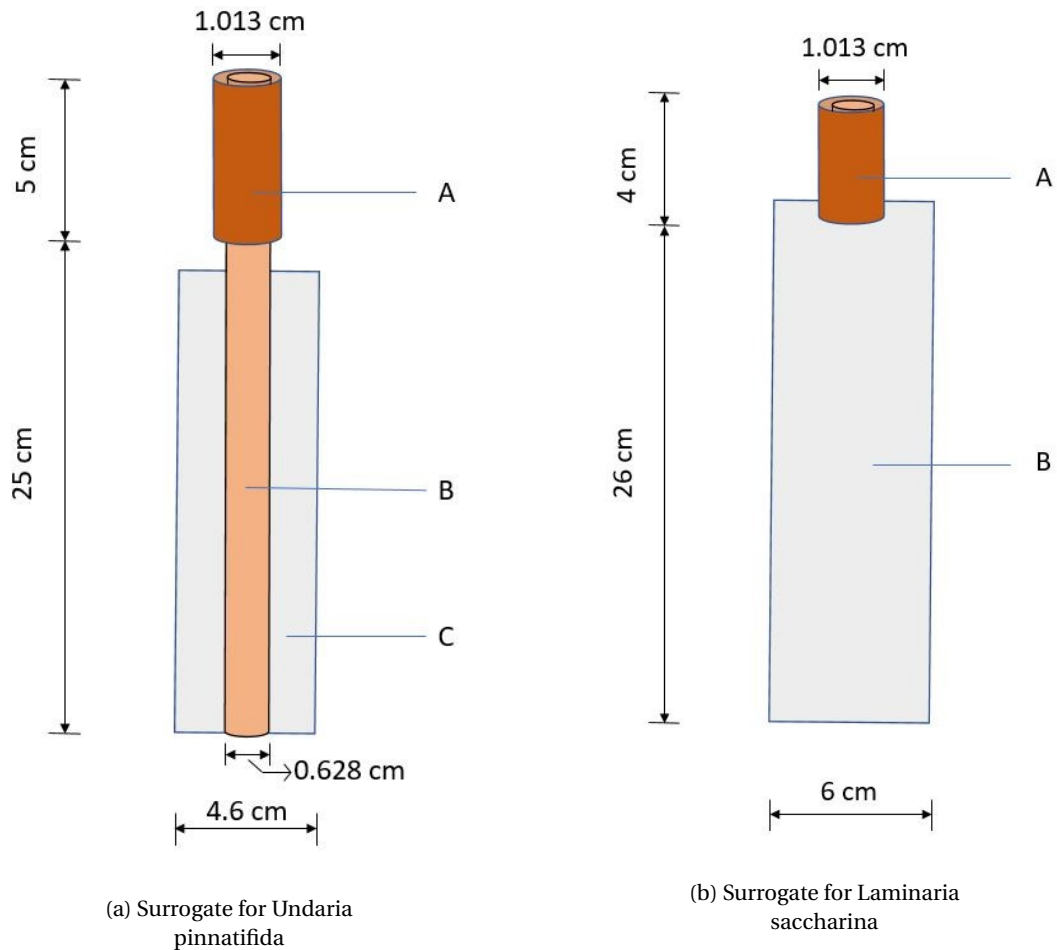


Figure 3.4: Surrogate schematic

Species of seaweed		Undaria pinnatifida		Laminaria saccharina	
Scale		4		5	
		Prototype	Model	Prototype	Model
Stem	Length (cm)	20	5	20	4
	Diameter (mm)	6.58	10.13	7.8	10.13
Whole blade	Length (cm)	120	30	150	30
	Width (cm)	18.4	4.6	30	6

Table 3.1: Comparison of prototype and model sizes for two types of seaweed of interest. The describing for parameters are in text.

3.3. Parameters of chosen surrogate materials

As information on the characteristics for *Laminaria saccharina* is lacking, a set of feature parameters from *Laminaria digitata* is used, based on results from [38]. This is deemed acceptable because the features of the two species from the *Laminaria* genus are similar. To be specific, the results and the parameters comparison between prototype and chosen surrogates are listing in the Table 3.3 where Silicon tube I is the Tube B in the Figure 3.3a; Silicon tube II is the combination of Tube B, E, F, and G; Silicon tube III is combination of Tube E, F, and G. On the other hand, Plastic sheet I is double layer of sheet A in Figure 3.3b; Plastic sheet II is sheet F. The densities in the table are the whole density for the combined surrogates with tubes, plastic sheets, glue and added clay. The plus-minus sign in Table 3.3 stands for the standard deviation of the parameter which showing the dispersion of data values.

Parameters	Outer diameter (Inner diameter)	Thickness	Density	Flexural rigidity	Bending modulus
Symbols	$D_o(D_i)$	t	ρ	J	E
Units	(mm)	(mm)	(kgm^{-3})	($\times 10^{-4} Nm^2$)	(Mpa)
L.saccharina stalk Silicon tube I	7.8 ± 1.4 10.13(1.53)	- -	1001.50 ± 102.70 990.82	28.88 ± 7.06 26.70 ± 4.95	28.67 ± 13.22 31.76 ± 5.89
L.saccharina leaves Plastic sheet I	- -	0.50 0.38	1001.50 ± 102.70 990.82	51.96 ± 30.35 41.75 ± 7.18	13355.75 ± 8385.60 22825.00 ± 3925.20
Wakame stalk base Silicon tube II	6.58 ± 0.14 10.13(1.53)	- -	1076.2 ± 173.78 1132.45	29.78 ± 19.48 29.02 ± 1.06	12.17 ± 8.64 22.47 ± 0.82
Wakame stalk tip Silicon tube III	3.61 ± 0.84 6.28(1.53)	- -	1076.2 ± 173.78 1132.45	2.68 ± 1.15 3.80 ± 0.31	8.67 ± 7.5 19.97 ± 1.65
Wakame leaves Plastic sheet II	- -	0.20 0.14	1076.2 ± 173.78 1132.45	1.52 ± 0.07 2.18 ± 0.79	10418.41 ± 507.81 23885.98 ± 8268.78

Table 3.2: Properties of fresh seaweed and selected abiotic materials (\pm standard deviation)

From the table, we can observe that seaweed's physical characteristics have a significant standard deviation, especially for leaves part, which means that our specimen's morphology is variant. Explanations can be a discrepancy in growing phase or in the ability to uptake nutrients. Additionally, the experiment apparatus for the three-point-bending test will cause errors. On the other hand, the chosen silicon tubes have acceptable characteristic parameters magnitude with fresh seaweed stalks and have a small standard deviation. However, for selected plastic sheets, values still lie within the standard deviation range of the leaves.

In the end, surrogates for two types of plant are designed and constructed. Figure A.1 shows two types of surrogate respectively. The specific parameters for each type of materials are listed in Appendix A.

4

Flume experiment

The purpose of the flume experiment is to get the hydrodynamic coefficients and loading on the surrogate. Furthermore, observing the behavior of two types of seaweed surrogates in the affection of current is required. In the first section of this chapter, the experimental method will be elaborated on. After that, a simple description of the behavior of two seaweed surrogates will be included. The last but not the least part is the analysis of the experimental data. The experiment was conducted in a water flume in Delft University of Technology (TU Delft) Environmental Fluid and Mechanics Laboratory in Civil Engineering Faculty.

4.1. Experiment set-up

The flume that was used in this experiment is a current generating flume with 45cm width and 40cm depth in TU Delft fluid laboratory like its overview showing in Figure 4.1a. As shown in the picture, current is generated or controlled by an upstream valve at position A (Figure 4.1a and 4.1b). At the other end of the flume (position B shown in Figure 4.1a), a dam that can adjust the water level was installed in order to control the velocity of the current by coordinating with the valve.

The entire experiment procedure was recorded by Sony DSC-HX50 (side view, was located at C in Figure 4.1a) and Go-pro 4 silver (front view in the water, was located at D in Figure 4.1a). Location E zone in Figure 4.1a is the experimental test site. A side view is shown in Figure 4.1c and details of apparatus position illustrated in Figure 4.1d. The seaweed surrogates, which were designed and constructed as described in Chapter 3, were fixed on the platform. A force sensor (Utilcell Load cell M104) based on double bending beams structure with a precision of $\pm 0.24\text{g}$ was mounted between the surrogate stalk and platform to recording the horizontal force along the flume. Two paper rulers were also posted on the water flume's front window for the position reference.

At the same time, an electro magnetic flow velocity sensor (EMS), with a precision of $\pm 0.0244\text{ms}^{-1}$, was installed in the flume at a front cross-section of the seaweed surrogate to record the current velocity ($v_c(t)$). Figure 4.2 displays the velocity distributions along the depth of the flume. It is apparently seen that between the depth of -2cm and -32cm , fluid speed is almost the same. Therefore I assume the fluid velocity of the water particles in the volume which fully encompass the surrogate can be represented by the velocity that was tested by the speed sensor.

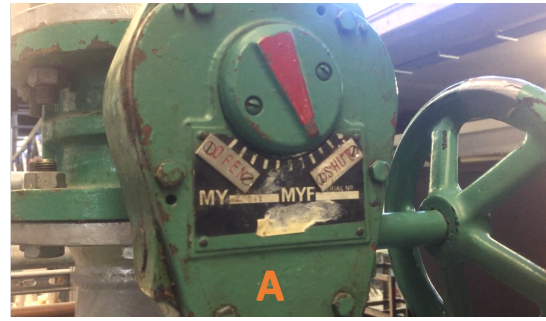
During the experiment, a couple of groups of tests with different current velocities from small to large were conducted. Reading and recording the forces and velocities as a function of time separately from sensors by a graphically programmable data acquisition system DASyLab 13.0. Attack angle is the angle between the central line of the surrogate body and the incoming fluid direction. It is shown in Figure 4.4 and will be explained in detail in Section 4.3. It will be measured by observing the depths ($h_1, h_2, h_3\dots$) through the drawing points on the stalk and leaves of surrogates. Then the project area which against the fluid incoming direction for each moving phase can be calculated.

4.2. Surrogate behavior in the current

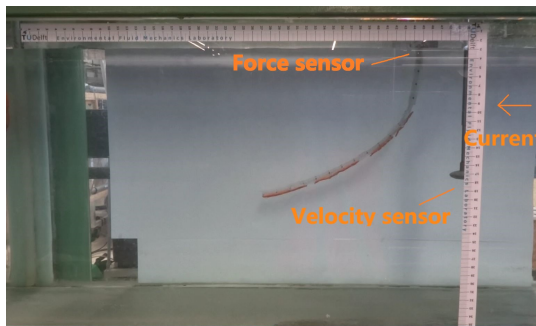
During the test, the current speed was controlled up to 0.6ms^{-1} due to the limit of the flume size and the current generator. The surrogate of *Undaria pinnatifida* (Wakame) swings up and down when the current velocity increase and decrease respectively. It is relatively simple behavior, but one thing should be noticed that



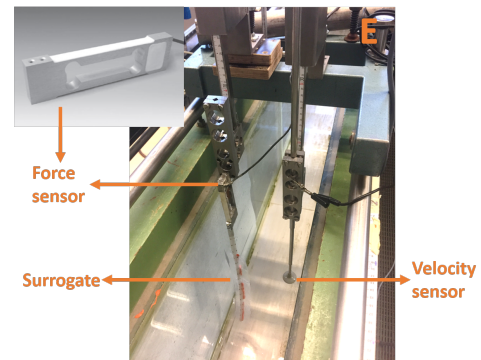
(a) Overview of the current flume and experiment set-up



(b) Upstream water valve that can control the current velocity



(c) Side view of experiment flume



(d) Force sensor, surrogate (left) and velocity sensor (right)

Figure 4.1: Photos of the flume and introduction of experiment set-up

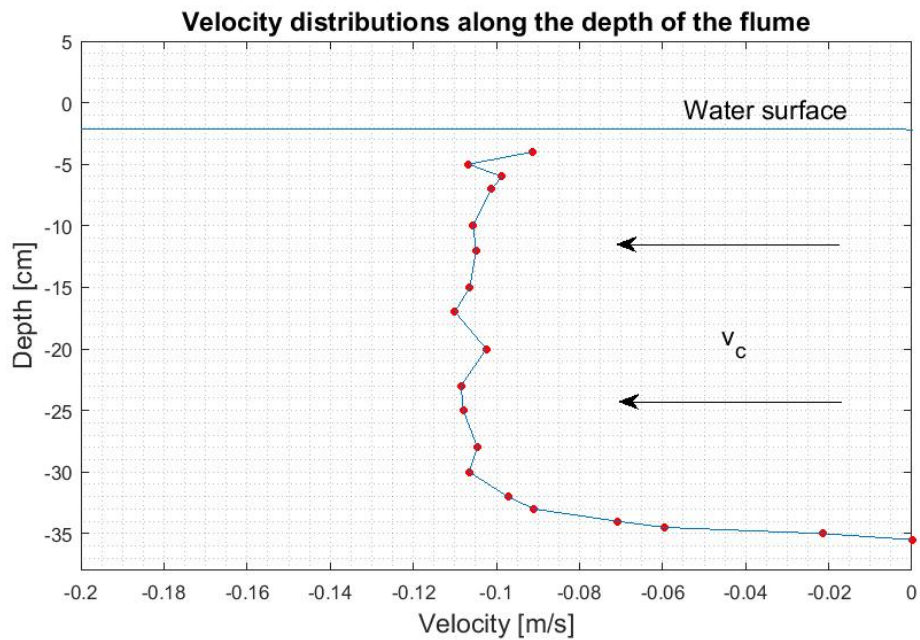


Figure 4.2: Velocity distributions along the depth of the flume (The water surface is at level -2cm and the bottom of the flume is at level -37cm reading from paper scales)

when the object is going into a situation that looks kind of like ‘steady-state’ condition. In this situation, it apparently does not move relative to the fixation point, but instead shakes itself chaotically. This phenomenon might be because of the slight change of the velocity or it could also be caused by the shielding vortex surrounding the object. This phenomenon will be further discussed later. As observed from the front view, the surrogate does not have too much movement perpendicular to the flume walls. Accordingly, the motion of the surrogate in the uni-direction fluid is understood as a two-dimensional movement.

During the experiment, the movement of *Laminaria saccharina* proxy is more complicated than *Wakame*, when the current velocity is controlled between 0 and 0.6ms^{-1} . Even at small velocity changes, the behavior of the surrogate changes significantly. From 0 to 0.02ms^{-1} , the blade of *L.saccharina* floats easily, but when the speed is changed to 0.05ms^{-1} , it swings for a quarter of a circle and starts flapping and shaking irregularly because of the pliability of the material. If its fixation point is close to the water surface, its movement will overlap with the surface of the water and then, no matter how large the velocity increase to, the leaf will neither swing up outside the water nor swing back. This behavior is caused by a comprehensive impact from water pressure, shedding vortex impact, and the low stiffness of the object.

Due to the behavior of *L.saccharina* being too irregular and complex, *Undaria pinnatifida* (*Wakame*) has been chosen here as the species of the seaweed to be analyzed. To be specific, data gathered in the experiment is analyzed, and the method is elaborated below.

4.3. Data analysis methodology

It is easy to predict that the drag force is an important force in an uni-direction flow like a current. From the Merriam-Webster Dictionary [9], drag is defined as a force acting parallel but opposite to the relative motion of a body moving with respect to a surrounding fluid.

Types of drag are usually divided into two categories: form drag and skin friction. Form drag is also known as pressure drag which is caused by the pressure difference. It arises due to the shape and size of the object. Bodies with a larger cross-section area will experience a higher drag than smaller bodies if they are in the same flow. Furthermore, if the frontal area of the bodies are the same, the higher the velocity of the fluid, the larger the drag on the body (in terms of the drag equation).

Skin friction drag occurs when the fluid comes in contact with the surface of the objects. It depends on the surface area of the body that contact with the fluid. The degree of roughness on the body surface decide the bigness of the friction. In general, larger surface roughness, higher velocity and larger contact surface area mean greater friction drag.

As shown as the first situation in Figure 4.3, if the body thickness is small enough and is placed parallel of the fluid moving direction, the skin friction drag is largest and no form drag occurs. On the other hand, the last row in the Figure 4.3, when the body is placed perpendicular against the fluid, the form drag is largest and no skin drag occurs.


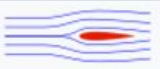


Shape and flow	Form Drag	Skin friction
	0%	100%
	~10%	~90%
	~90%	~10%
	100%	0%

Figure 4.3: Form drag and skin friction by [45]

In our case, when fluid hits the surrogate, it will cause a form drag and a skin friction at the same time. Due to the definition from [9], drag is acting opposite to the relative motion of the object with respect to surrounding fluid. Thus, here, the form drag is treated as drag that follows the definition. Because of the attack angle, when we handle the measured velocity, it will be divided into two components, one in the normal direction of the surrogate blade and the other one along the axial direction of the blade. Apparently, it will give surrogate two forces F_N and F_{Af} (i.e. form drag force in normal direction of the body and skin frictional drag force in axial direction of the body) respectively.

The exact direction of drag force is unknown because we have no information about the relative motion direction from the information we know. However, the horizontal components of these two forces is approximately equal to the force that tested from the force sensor in the experiment. In that way, we can investigate the relationship between drag and velocity.

The drag coefficient is a dimensionless quantity that is usually used to described the quantity of drag. For

the drag coefficient calculation for the seaweed, some previous research such as [5] have not divided it into form drag and skin friction. According to [5], for flexible organisms like macro-algae, the maximum plant area (single-side) of the thallus and the incoming fluid velocity could be used in the calculation. In this procedure, the calculation followed the traditional drag force equation (drag part of the Morison equation [30] which is shown in Equation 4.1), that drag force (F_d) depends on the fluid density, project area, velocity, and drag coefficient.

$$F_d = \frac{1}{2} C_d \rho_w A v_c^2 \quad (4.1)$$

Where C_d is the drag coefficient, ρ_w is the fluid density, and v_c is the velocity. Furthermore, A is the full frontal area of the seaweed thallus.

However, in actuality, the frontal area that perpendicularly contact with the fluid is changing all the time. This is likely be a significant influence on the drag coefficient results. Additionally, the separation of the drag to two components is more accurately. Therefore, in this chapter, two components of the drag will be considered separately and the project area will be implemented. The results will also be compared with the results from [5] method.

4.3.1. Form drag

As we discussed above, the form drag is caused by the shape of the body and its direction opposes the relative motion of the body and fluid. In our case, the body is flexible and changes its position and shape frequently. An assumption is here that, in order to reduce difficulty, we assume that the form drag acts on the normal direction of the body of the seaweed surrogate. In this way, the form drag is entirely contributed by the velocity component on the same direction. When we want to use the project area (as a function of time) to calculate the drag, the Equation 4.1 should be rewritten as,

$$F_d = \frac{1}{2} C_d \rho_w A(h) v_c^2 \quad (4.2)$$

where, the project area $A(h)$ is changing with the attack angle α variation, and attack angle is changing as a function of new depth (h) for each point on the surrogate. Attack angle α is the angle between the line which from fixing point to tip of surrogate and the horizontal line. An illustration is shown in Figure 4.4a.

From the experiment, we only know the horizontal force on the fixed point, thus to find the drag coefficient, we have to divide the form drag (F_N) into horizontal component (F_D) and vertical component (F_L) respectively. The Figure 4.4a is shown for the forces that working on the model.

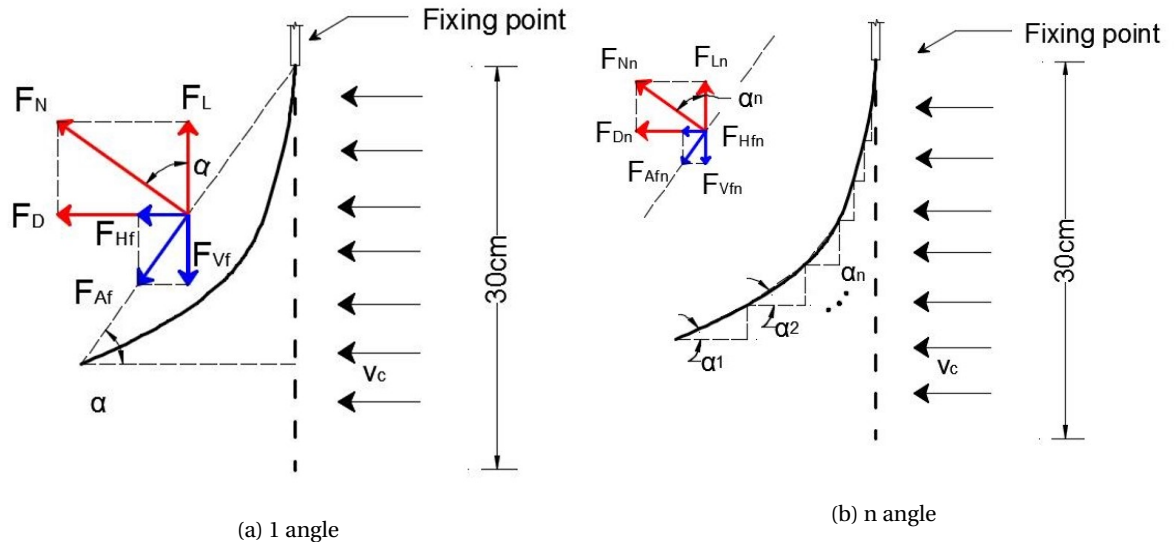


Figure 4.4: Hydrodynamic forces on Seaweed and definition of the attack angle

The relationship between velocity and horizontal component F_D of the form drag F_N could also be described by an 'coefficient'. This 'coefficient' is easy to get in our case, but this is not the 'real' drag coefficient. We would like to define it as 'horizontal drag coefficient C_{HD} ' and it could be written as

$$C_{HD} = (C_D)_{90} \sin^3(\alpha) \quad (4.3)$$

where $(C_D)_{90}$ stands for the maximum coefficient that happens when the surrogate was hanging straight down. This means that attack angle α is equal to 90° . The relationships of forces in Figure 4.4a could be help us demonstrating the derivation of the Equation 4.3. The form drag F_N which is normal to the surrogate is calculated by the component of the velocity in the same direction as

$$F_N = \frac{1}{2} \rho_w A_{full} (v_c \sin(\alpha))^2 (C_D)_{90} \quad (4.4)$$

where the term $v_c \sin(\alpha)$ is the velocity component on the normal direction of the test body. A_{full} is the full frontal area of the body. In this case, the normal velocity component is perpendicular to the body, so the attack angle is 90° then $(C_D)_{90}$ is used here. After this F_N is divided into two components in horizontal direction as a horizontal drag force F_D and vertical direction as a vertical drag force F_L . These forces can be described by Equation 4.5 and 4.6 separately.

$$F_D = F_N \sin(\alpha) = \frac{1}{2} \rho_w A_{full} v_c^2 \sin^3(\alpha) (C_D)_{90} \quad (4.5)$$

$$F_L = F_N \cos(\alpha) = \frac{1}{2} \rho_w A_{full} v_c^2 \sin^2(\alpha) \cos(\alpha) (C_D)_{90} \quad (4.6)$$

Then the Equation 4.3 can be obtained. On the other hand, the other fluid force which is generated by another component in the axial direction of the surrogate will be introduced in Section 4.3.2.

4.3.2. Axial skin frictional drag

Axial skin frictional drag (F_{Af}) is caused by the friction and roughness on the surrogate surface which is controlled by an axial direction component of the velocity ($v_c \cos(\alpha)$). Its direction and components are shown as blue arrows in Figure 4.4a. The equation is as similar as the Equation 4.4 and written as:

$$F_{Af} = \frac{1}{2} \rho_w A_{full} (v_c \cos(\alpha))^2 C_f \quad (4.7)$$

Where C_f is skin frictional drag coefficient. Also, the horizontal (F_{Hf}) and vertical (F_{Vf}) component of the skin frictional drag are:

$$F_{Hf} = F_{Af} \cos(\alpha) = \frac{1}{2} \rho_w A_{full} v_c^2 \cos^3(\alpha) C_f \quad (4.8)$$

$$F_{Vf} = F_{Af} \sin(\alpha) = \frac{1}{2} \rho_w A_{full} v_c^2 \cos^2(\alpha) \sin(\alpha) C_f \quad (4.9)$$

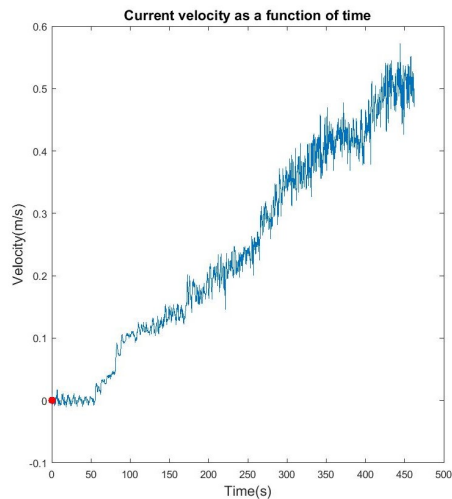
4.4. Experiment results

In this section, the axial skin frictional drag coefficient and the horizontal drag coefficient are shown and discussed in detail. The morphology parameters that used in the analysis follow the numbers of model in Table 3.1. Furthermore, the raw trial data in Appendix B shows the time series of velocity and drag force during the experiment.

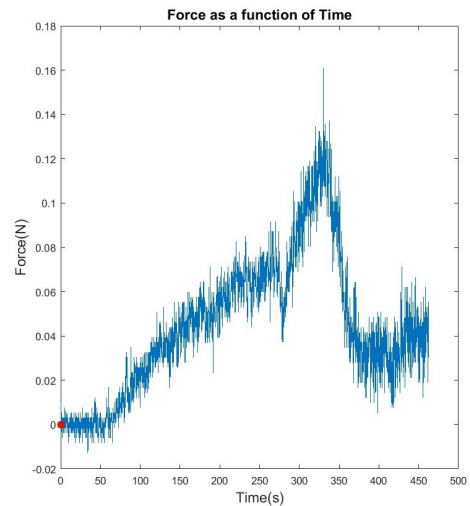
4.4.1. Axial frictional drag force

During the experiment, an interesting phenomenon happens when the velocity increase to one critical velocity or when the water surface level decrease. The whole body of the surrogate will move together with the water surface streamline displayed in Figure 4.5c. In Figure 4.5a and Figure 4.5b, abscissas stand for the experiment time, and ordinates stand for velocity and the force which are measured by two sensors. We can observe that when the time reaches around 335s, the velocity keeps increasing, but the force has a dramatic fall. And 335s is also the time when the surrogate reaches the horizontal position. Thus, experiment data from 335s to 440s is dragged out and clearly shown Figure 4.5d.

We have a reason to believe that the force suddenly falls is because the form drag is not playing a role when a surrogate body moves to horizontal position due to the attack angle α in the Equation 4.4 becoming equal to zero. Therefore, in this situation, the only force that can be measured by the force sensor in horizontal direction on the body is the axial skin frictional drag (in other words, it is the dominant force in this



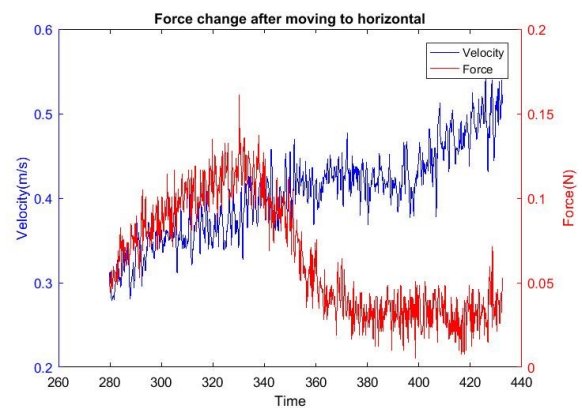
(a) Current velocity as a function of time
(experiment data that was measured by the velocity sensor)



(b) Horizontal force as a function of time
(experiment data that was measured by the force sensor)



(c) When the velocity increase to one limitation or when the water surface level decrease, the proxy get to a horizontal position and moving with water surface



(d) Force suddenly falls down after the body gets into a horizontal position

Figure 4.5: Axial skin frictional drag analysis

case). Then the measured force from the experiment is equal to skin friction. Thus, the skin frictional drag coefficient will be easily computed as C_f is equal to 0.037 through substituting attack angle $\alpha = 0$ into the Equation 4.8.

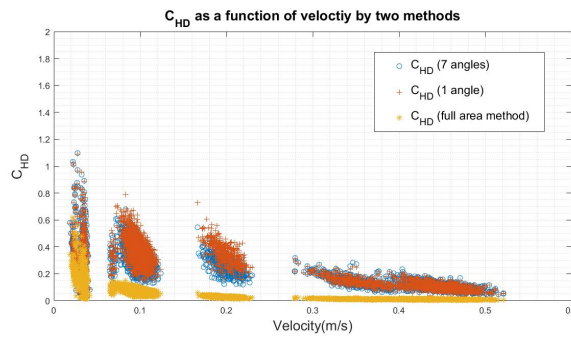
4.4.2. Form drag

In the experiment, 19 groups with different velocities have been chosen to study the relationship between horizontal drag coefficient and attack angles. The used test velocities were controlled changing slightly during the period of each group to help the front of the surrogate stream be normal to the incident flow. The mean value of the velocities was calculated separately for these groups. The horizontal drag coefficients based on both the full frontal area method and the projected area method was computed. At the same time, for the project area method, each group should be calculated by one angle (α showing in Figure 4.4a) and by n angles (α_n showing in Figure 4.4b, $n = 7$ has been chosen as an example here) respectively. The results from the latter two will be compared with each other to see the influence coming from different angle simplification methods that describe the configuration of the structure. In this procedure, in the horizontal direction, the measured

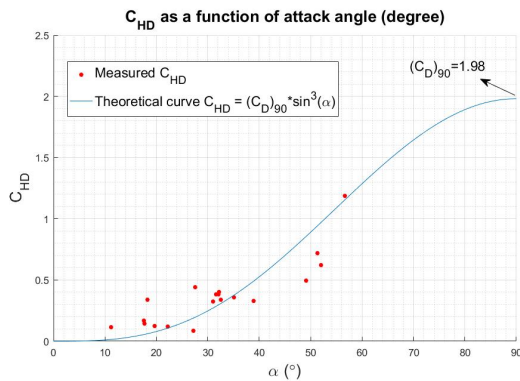
force (F_m) is equal to the horizontal component (F_D) of normal drag force plus the horizontal component (F_{Af}) of axial frictional drag force as

$$F_m = F_{Hf} + F_D = \frac{1}{2} \rho_w A_{full} v_c^2 \cos^3(\alpha) C_f + \frac{1}{2} \rho_w A_{full} v_c^2 \sin^3(\alpha) (C_D)_{90} \tag{4.10}$$

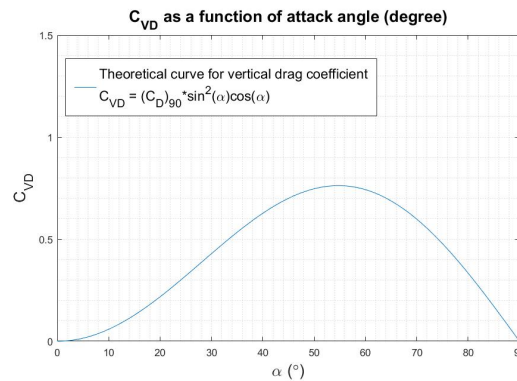
In this case, attack angle (α and α_n) is measured by recorded videos of the experiments. The horizontal drag coefficient C_{HD} is calculated by project area method (Equation 4.10) and full area method (Equation 4.1). The results are shown in Figure 4.6a. In the graph, the blue circles and the red dots are coefficients that were calculated by taking seven angles and one angle into account respectively. The yellow dots are the results based on entire area that was followed the changeless area method that was also implemented by [5]. It is clear that the horizontal drag coefficients that were calculated based on the full area is apparently smaller than the others. Furthermore, when comparing the two groups that used the project area method, (for one angle method and seven angles method), they are almost overlapping with each other, or the difference between them is tiny. It is mean that the number of n is not influence the results of the coefficient. So I assume these two horizontal drag coefficients are the same. This allows us looking for a relationship between horizontal drag coefficient and one angle α .



(a) Horizontal drag coefficient based on both the full frontal area and the projected area



(b) C_{HD} as a function of angle, compared with measured C_{HD}



(c) Vertical drag coefficient C_{VD} as a function of angle

Figure 4.6: Current flume results for form drag

According to [17], the drag coefficient for a plate that has a rectangular shape and high aspect ratio (length : width ratio) has been found around 1.98. Therefore, here, I assume $(C_D)_{90}$ is equal to 1.98. The theoretical curve is shown and also the measured horizontal drag coefficients of the surrogate based on one angle were marked as red dots in Figure 4.6b separately. It is able to be noticed that the theoretical curve is approximately matching the measured data. However, the dots on top of the theoretical curve between 10° and 40° are scattered. Considering the quite large sensitivity to error due to

$$\frac{dC_{HD}}{d\alpha} = 3(C_D)_{90} \sin(\alpha)^2 \cos(\alpha) \quad (4.11)$$

which is mean that if angle has an error of 1° at around 30° , horizontal drag coefficient will have an error with 1.29. Therefore, it is reasonable to determine the data from experiment results are matching well with theoretical curve.

On the other hand, after horizontal drag coefficient has been defined, the 'vertical drag coefficient' C_{VD} for the vertical component F_L that could be deviated by Equation 4.6. It can be expressed as following and its curve are shown in 4.6c

$$C_{VD} = (C_D)_{90} \sin^2(\alpha) \cos(\alpha) \quad (4.12)$$

5

Numerical model

We described the flume experiment and obtained the ‘horizontal drag coefficient’ curve and ‘axial skin frictional drag coefficient’ for the specific shape of the surrogate in the previous chapter. In this chapter, the simplified method of the seaweed mechanical structure is elaborated, and a structural model is designed for simulation of the movement in the experiment. This model is expected to be used later on the simulation and for prediction of the movements and loading of various algae prototypes. To be specific, kinetic energy and potential energy are deviated for the aimed object and along with this, external forces such as hydrostatic forces and drag forces are analyzed and formulated. Then in the last section, a validation simulations have been done by comparing model predictions with the experimental results.

5.1. The structure model

In the experiment it was observed that there were no significant motions of the surrogate in the direction perpendicular to the fluid movement. Therefore, we can consider the motions of the system to be planar.

The body of the surrogate is simplified as a mass-rotational-spring system like shown in the Figure 5.1. The coordinate system x, y is also shown in the graph. The whole structure is evenly divided into n sections. For each section, it consists of a lumped mass, a rotational spring and an imaginary dashpot. The rotational spring is a flexible elastic object that stores potential energy when it is rotated. It exerts a torque that is proportional to the rotated angle (θ_n) but in the opposite direction. The spring constant is related to the model bending modulus E , the inertia of moment I , and the length l of each section. There is an imaginary dashpot which works at the same place in each section of each spring to generate viscous damping (the dash pots are not shown in the figure). Furthermore, the lumped masses and the lengths are same for each section.

As a simulated current incidents and attacks the seaweed structure in the model, a reaction of fluid and structure will be caused. The simulated structure will be expected swing up as be attacked by the fluid. This means that each section of the structure will rotate and the new coordinate of the i^{th} mass block is equal to Equation 5.1 and 5.2, where θ_i is the rotational angle for the i^{th} section.

$$x_i = \sum_{j=1}^i l_j \sin(\theta_j) \quad (5.1)$$

$$y_i = - \sum_{j=1}^i l_j \cos(\theta_j) \quad (5.2)$$

Thus, velocities for each mass block can be written as Equation 5.3 and 5.4. They are calculated by find the derivative of x_i and y_i of time t .

$$\dot{x}_i = \sum_{j=1}^i l_j \cos(\theta_j) \dot{\theta}_j \quad (5.3)$$

$$\dot{y}_i = \sum_{j=1}^i l_j \sin(\theta_j) \dot{\theta}_j \quad (5.4)$$

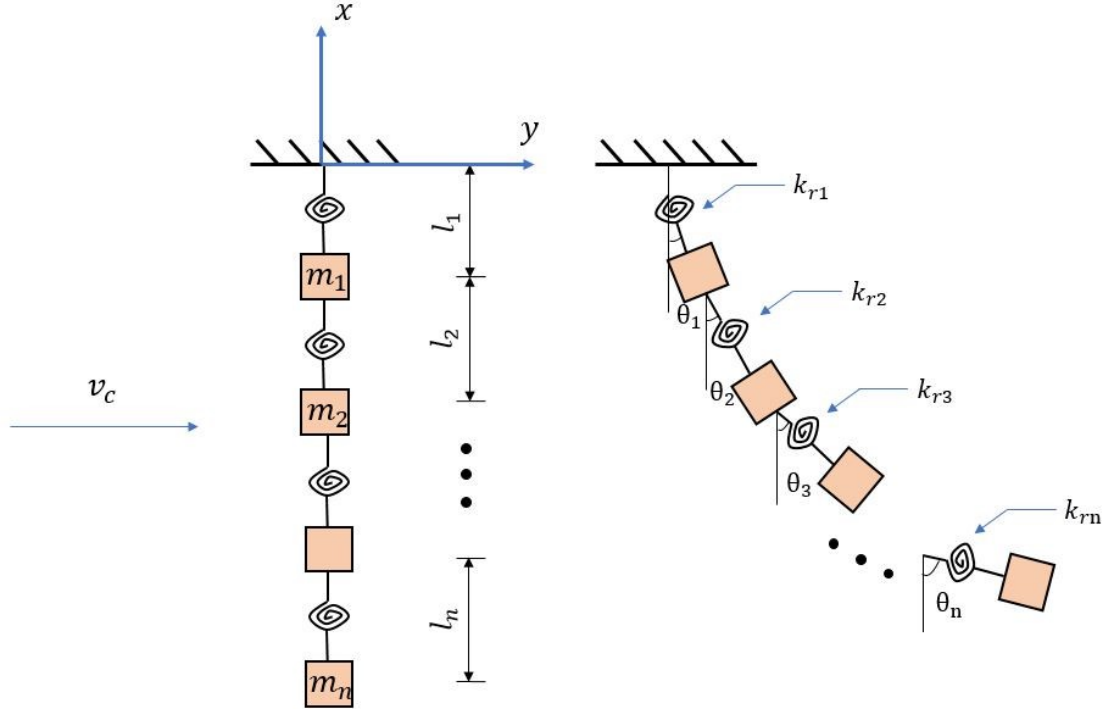


Figure 5.1: Diagram of the simplify strategy and coordinates systems: The whole structure is evenly divided into n sections. For each section, it consists of a lumped mass, a rotational spring and an imaginary dashpot (the dash pots are not shown in the figure but it works at the same place of the spring). In the figure, m_i , l_i , and k_{r_i} are mass, length, and rotational spring constant for i^{th} section respectively. θ_i is the rotational angle for i^{th} section. v_c is the current direction and velocity

where dot denotes differentiation with respect to time, t , so that the term $\dot{\theta}$ is the rotational velocity for each mass. Hence, the kinetic energy of the i^{th} mass block is equal to half of the product of the mass and the square of the speed as

$$T_{si} = \frac{1}{2} m_i (\dot{x}_i^2 + \dot{y}_i^2) \quad (5.5)$$

where m_i is mass of the i^{th} mass block and the subscript 's' stands for 'structural'. Hence the total kinetic energy T_s of the structure (the summation of kinetic energy T_{si} of each section) is

$$T_s = \frac{1}{2} \sum_{i=1}^n m_i (\dot{x}_i^2 + \dot{y}_i^2) = \frac{1}{2} \sum_{i=1}^n m_i \left(\sum_{j=1}^i l_j \dot{\theta}_j \right)^2 \quad (5.6)$$

where n is the total number of the separated mass blocks. The rotational springs constant is related with the bending modulus E , the inertia of moment I , and the length l of each section and is shown as following

$$k_{r_i} = \frac{EI}{l_i} \quad (5.7)$$

In our case, the flexural rigidity EI , is not the same for each section. It follows the values for different parts of the model as measured in our experiment. These values are shown in Table 3.3 and the results of k_{r_i} are illustrated in Table 5.1. Therefore, the potential energy could be found as Equation 5.8 which consists of a component due to rotational spring and a component due to the gravitational force

$$V_s = \sum_{i=1}^n m_i g \sum_{j=1}^i l_j (1 - \cos(\theta_j)) + \frac{1}{2} \sum_{i=1}^n k_{r_i} (\theta_i - \theta_{i-1})^2 \quad (5.8)$$

5.2. External forces

The external forces working on the structure are all fluid forces which will be determined in two parts: hydrostatic forces and hydrodynamic forces. Forces acting on the n^{th} mass is showing in Figure 5.2

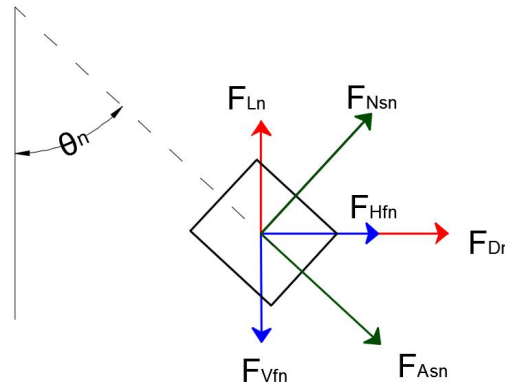


Figure 5.2: Fluid force acting on n^{th} mass. The specific meaning for each force is in the text.

In the graph, F_{Ln} is the vertical component of form drag and F_{Dn} is the horizontal component of form drag. F_{Hfn} and F_{Vfn} are the horizontal and vertical components of skin frictional drag, respectively. F_{Nsn} and F_{Asn} are hydrostatic forces on the normal and axial directions, separately. On the structure, the hydrostatic force in axial direction F_{Asn} just works on the last section (tail) and the first section (nose), because the sections in between do not touch the water directly on their cross-section. The subscript 'n' in each term stands for the force working on the last section, section 'n'. In the following subsections, the specific to calculate these forces will be described.

5.2.1. Hydrostatic forces

Hydrostatic forces on the structure can be divided into two parts, in the axial direction and normal direction of the body. Because of the thickness of the plate part of the structure is very small, the volume can be neglected. This means that the hydrostatic pressures on both side of the plate are the same, thus, here we assume that the hydrostatic force on the plate part can be omitted. Therefore, only the hydrostatic force on the cylindrical part of the structure is considered. The cylindrical part of the structure is shown in Figure 5.3.

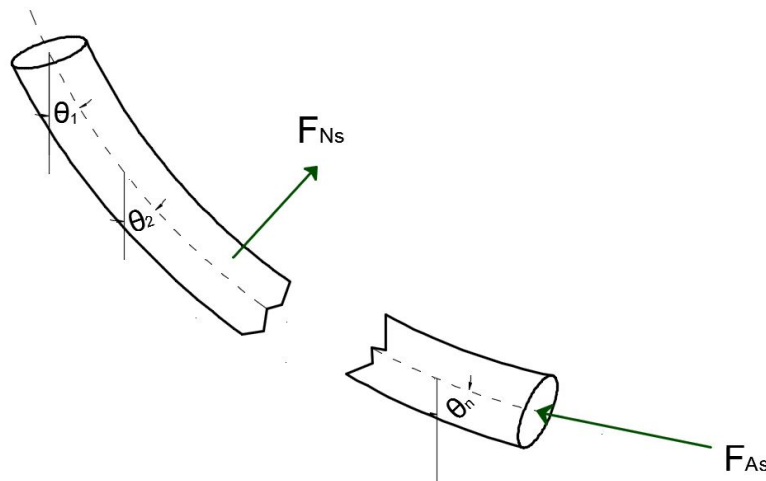


Figure 5.3: Hydrostatic force on a cylindrical body, separated in normal and axial directions

As described before, the axial hydrostatic force F_{As} works on the nose and tail sections of the structure. In this case, the nose of the structure was fixed on the platform near the water surface. Near the surface the pressure is assumed to be zero, which would mean that the axial hydrostatic force is also equal to zero. On the other hand, the axial hydrostatic force on the tail (the n^{th} section) can be express as the pressure on the tail times the area

$$F_{As} = \frac{\pi}{4} D^2 \rho_w g \sum_{i=1}^n l_i \cos(\theta_i) \quad (5.9)$$

where D is the cross-section diameter of the cylinder body, ρ_w is the density of water. It is assumed here that in each section, the body is straight. Additionally, hydrostatic force on normal direction of each section of the structure is equal to the difference of pressure between upper and lower semi-cylindrical surface. Accordingly, for the i^{th} section, it may be expressed as

$$F_{Nsi} = \frac{\pi}{4} D^2 \rho_w g l_i \sin(\theta_i) \quad (5.10)$$

5.2.2. Hydrodynamic forces

The hydrodynamic forces that work on the structure can also be separated into two parts: form drag and skin frictional drag. Both of them can be further divided into two directions as shown in Figure 5.2. In horizontal direction, the drag force F_{Hi} on the i^{th} mass can be written as

$$F_{Hi} = F_{Di} + F_{Hfi} = \frac{1}{2} \rho_w A_{full} v_c^2 \cos^3(\theta_i) (C_D)_0 + \frac{1}{2} \rho_w A_{full} v_c^2 \sin^3(\theta_i) C_f \quad (5.11)$$

where $(C_D)_0$ is the maximum horizontal drag coefficient when $\theta = 0^\circ$ (equivalent to $(C_D)_{90}$ in Chapter 4 for $\alpha = 90^\circ$) and C_f is frictional drag coefficient. A_{full} is the full thallus area of the i^{th} section. In vertical direction, also for the i^{th} section, the total drag force F_{Vi} is shown as follow

$$F_{Vi} = F_{Li} - F_{Vfi} = \frac{1}{2} \rho_w A_{full} v_c^2 \cos^2(\theta_i) \sin(\theta_i) (C_D)_0 - \frac{1}{2} \rho_w A_{full} v_c^2 \sin^2(\theta_i) \cos(\theta_i) C_f \quad (5.12)$$

5.3. Derivation of the equations of motion

In this section, non-linear equations of motion of the structure have been derived by Lagrangian equations by the combination of energies and external moments for large displacement angles. The details for a three-DOF system (i.e. separating the structure into three parts) has been shown in the 5.3.2 as an example.

5.3.1. Generated forces (moments) of the system

The generated forces (or more accurate, generated moments) Q_i on the i^{th} mass may be determined by the forces time its force arms. The arms for the horizontal forces (a_{hi}) and vertical forces (a_{vi}) on the i^{th} mass can be expressed as Equation 5.13 and 5.14 respectively

$$a_{hi} = \sum_{j=1}^i l_j \cos(\theta_j) \quad (5.13)$$

$$a_{vi} = \sum_{j=1}^i l_j \sin(\theta_j) \quad (5.14)$$

then generalized moment on the i^{th} mass is given by combining Equation 5.9 to 5.14 as

$$Q_i = a_{hi} [F_{Hi} + F_{Nsi} \cos(\theta_i) + F_{As} \sin(\theta_i)] + a_{vi} [F_{Vi} + F_{Nsi} \sin(\theta_i) - F_{As} \cos(\theta_i)] \quad (5.15)$$

Where the term F_{As} is only working on the last section (tail). The other parameters have been described in Section 5.2.

5.3.2. Application of Lagrangian equations

Lagrangian mechanics is widely used to analyze mechanical problems when Newton's formulation of classical mechanics is not convenient. According to [20], Lagrangian mechanics were introduced by the Italian-French mathematician Joseph-Louis Lagrange in 1788 as [24]. It is a reformulation of classical mechanics.

In Lagrangian mechanics, the displacements of particles in the system are derived by solving the Lagrange equations in one of two equation forms. The first kind of Lagrange equations, according to [11], usually use Lagrange multipliers and treat constraints explicitly as extra equations. The second kind of the Lagrange equations use generalized coordinates to incorporate the constraints. In both cases, a so-called 'Lagrangian' mathematical function is used. This function is often indicated by L . It is a function that summarizes the dynamics of the system and includes the kinetic energy T and the potential energy V as follow

$$L = T - V \quad (5.16)$$

In our case, the second form of Lagrangian which incorporates the constraints by generalized coordinates is used. It is also known as Euler-Lagrange equations. It can be written as

$$\frac{d}{dt} \left(\frac{\partial L}{\partial \dot{q}_i} \right) = \frac{\partial L}{\partial q_i} \quad (5.17)$$

In the equation, the vector q is a point in the configuration space of the system. The \dot{q} is a generalized velocity that comes from the time derivatives of the generalized coordinates. The final equations of motion are often linearized by assuming that rotational angles are small in solid mechanical problems. It is done by using the first few terms of the Taylor series of sine and cosine angles. To be specific, the following equations are usually used in the final non-linear EOM obtained from the Lagrangian derivation.

$$\sin(\theta) = \theta - \frac{\theta^3}{3!} + \frac{\theta^5}{5!} - \dots \approx \theta - O(\theta^3) + O(\theta^5) \quad \Rightarrow \quad \sin(\theta) \approx \theta \quad (5.18)$$

$$\cos(\theta) = 1 - \frac{\theta^2}{2!} + \frac{\theta^4}{4!} - \dots \approx 1 - \frac{\theta^2}{2} + O(\theta^4) \quad \Rightarrow \quad \cos(\theta) \approx 1 \quad (5.19)$$

The above linearization equations on the right hand side can only be made when the displacement angles are small enough. The accuracy of the approximation can be seen in Figure 5.4. As the angle approaches zero, it is clear that the gap between the curves vanishes. In Figure 5.4b, the approximation that is calculated by maintaining two terms ($1 - \theta^2/2$) of the series is better than one term (1).

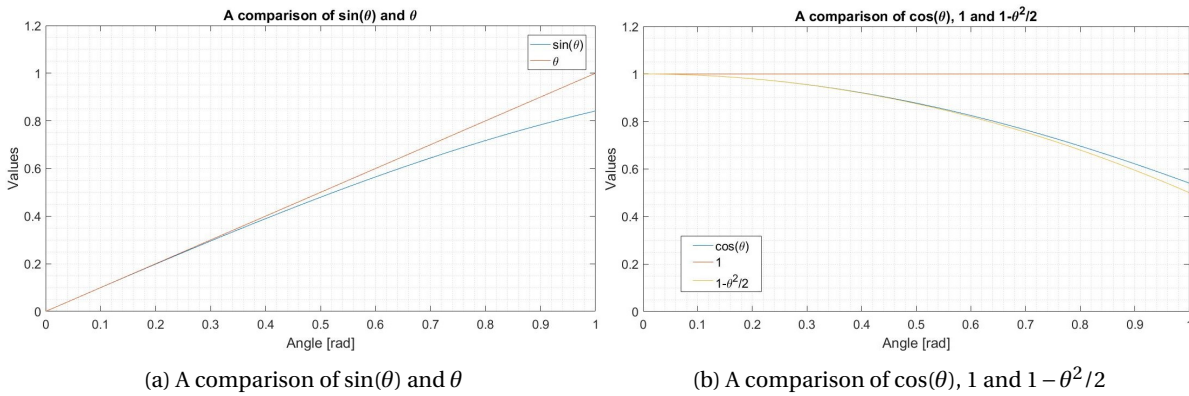


Figure 5.4: The accuracy of the approximation

In our case, the flexible structure is considered. Thus, the prerequisite of a small angle for the assumption of linearization, does not be satisfied. So, an non-linear EOM is expected after implement Lagrangian derivation. However, this approximation will be implementing in Chapter 6.

After Substituting Equation 5.6, 5.8, 5.15, and 5.16 into 5.17, the Euler-Lagrange equations are rewritten as follows

$$Q_i = \frac{d}{dt} \left(\frac{\partial T_s}{\partial \dot{\theta}_i} \right) - \frac{\partial T_s}{\partial \theta_i} + \frac{\partial V_s}{\partial \theta_i}, \quad i = 1, 2, 3 \dots n \quad (5.20)$$

For a system of n degrees of freedom (i.e. separating the structure into n sections), we can obtain n equations. Apparently the larger of n , the better it matches the practical reality.

Now, as an example, let's consider a simple case where the structure is separated into three sections (i.e. $n = 3$) and one lumped mass block for each section. The length l_i and mass m_i are the same for each section (then using l and m for each section in following equations). The equations of motion for this three-DOF system are expressed as:

$$J\ddot{\Theta} + C\dot{\Theta} + K_1\Theta + K_2\sin(\Theta) = Q \quad (5.21)$$

where

$$\ddot{\Theta} = [\ddot{\theta}_1 \quad \ddot{\theta}_2 \quad \ddot{\theta}_3]^T \quad \dot{\Theta} = [\dot{\theta}_1 \quad \dot{\theta}_2 \quad \dot{\theta}_3]^T \quad \Theta = [\theta_1 \quad \theta_2 \quad \theta_3]^T \quad (5.22)$$

$$Q = [Q_1 \quad Q_2 \quad Q_3]^T \quad \sin(\Theta) = [\sin(\theta_1) \quad \sin(\theta_2) \quad \sin(\theta_3)]^T \quad (5.23)$$

$$J = ml^2 \begin{bmatrix} 3 & 2 & 1 \\ 2 & 2 & 1 \\ 1 & 1 & 1 \end{bmatrix} \quad C = c_r \begin{bmatrix} 2 & -1 & 0 \\ -1 & 2 & -1 \\ 0 & -1 & 1 \end{bmatrix} \quad (5.24)$$

$$K_1 = k_r \begin{bmatrix} 2 & -1 & 0 \\ -1 & 2 & -1 \\ 0 & -1 & 1 \end{bmatrix} \quad K_2 = mgl \begin{bmatrix} 3 & 0 & 0 \\ 0 & 2 & 0 \\ 0 & 0 & 1 \end{bmatrix} \quad (5.25)$$

Generally speaking, in the above equations, J is so-called inertia matrix which determines the torque needed for an aimed angular acceleration. It is related to the mass of the body and the distance between the mass center and the rotational axis. The larger the mass or the distance, the larger the moment that's needed to give the body the desired acceleration. K_1 is the rotational stiffness matrix. From the equation of this, we can see that the movement of the one section is not only decided by the stiffness in this section, but also influenced by the stiffness of its two adjoining sections. For example, the displacement angle between the second spring (θ_2) and the equilibrium position is not the effective angle for the second rotational spring. However, the difference of two angles ($\theta_2 - \theta_1$) is. C is the damping matrix which stands for the energy dissipation and vibration reduction by viscous damping that happens when the structure has rotational movement. K_2 is the another type of stiffness matrix that shows the contribution of the gravity in the system. Because the angles that are dealt with here are big angles which can not be linearized, thus, K_2 is multiplied by a sine angle in EOM.

5.4. Matching with experiment results

In this section, the simulation results of the model are compared with the results that come from the experiment. In the experiment analysis, seven angles were tested from the recorded videos to describe the positions and configurations in the 'seven angles method' in Section 4.4.2. Thus in the model, we also chose to separate the whole structure into seven sections (i.e. $n = 7$). Then, the steady-state positions of the structure which are tested by experiment and simulated by the model are comparable. Also, the simulated forces could be compared with the measured force for proving the matching between the results from model and test. Some parameters are shown in the Table 5.1 with n is equal to seven.

Parameters	Mass (m)	length (l)	k_r for the first section	k_r for the other sections	c_r
Unit	g	cm	Nm	Nm	Nms
Values	$\frac{17.1}{7}$	$\frac{30}{7}$	0.05804	0.0152	0.013

Table 5.1: Parameters that are used when n is equal to seven

5.4.1. Steady-state position comparison

As described in 4.4.2, we have already got the steady-state positions (or angles for each section) for 19 different velocity groups. Because in each group, velocity does not change during the group period, we can input the velocities for each group and compare the steady-state position from the model with the steady-state position that was measured in the experiment. In Figure 5.5, shows the comparison when the velocity are $v_c = 0.10ms^{-1}$, $v_c = 0.20ms^{-1}$, $v_c = 0.32ms^{-1}$, and $v_c = 0.42ms^{-1}$ respectively. From these graphs, the model's predictions and the measurements match each other quite well.

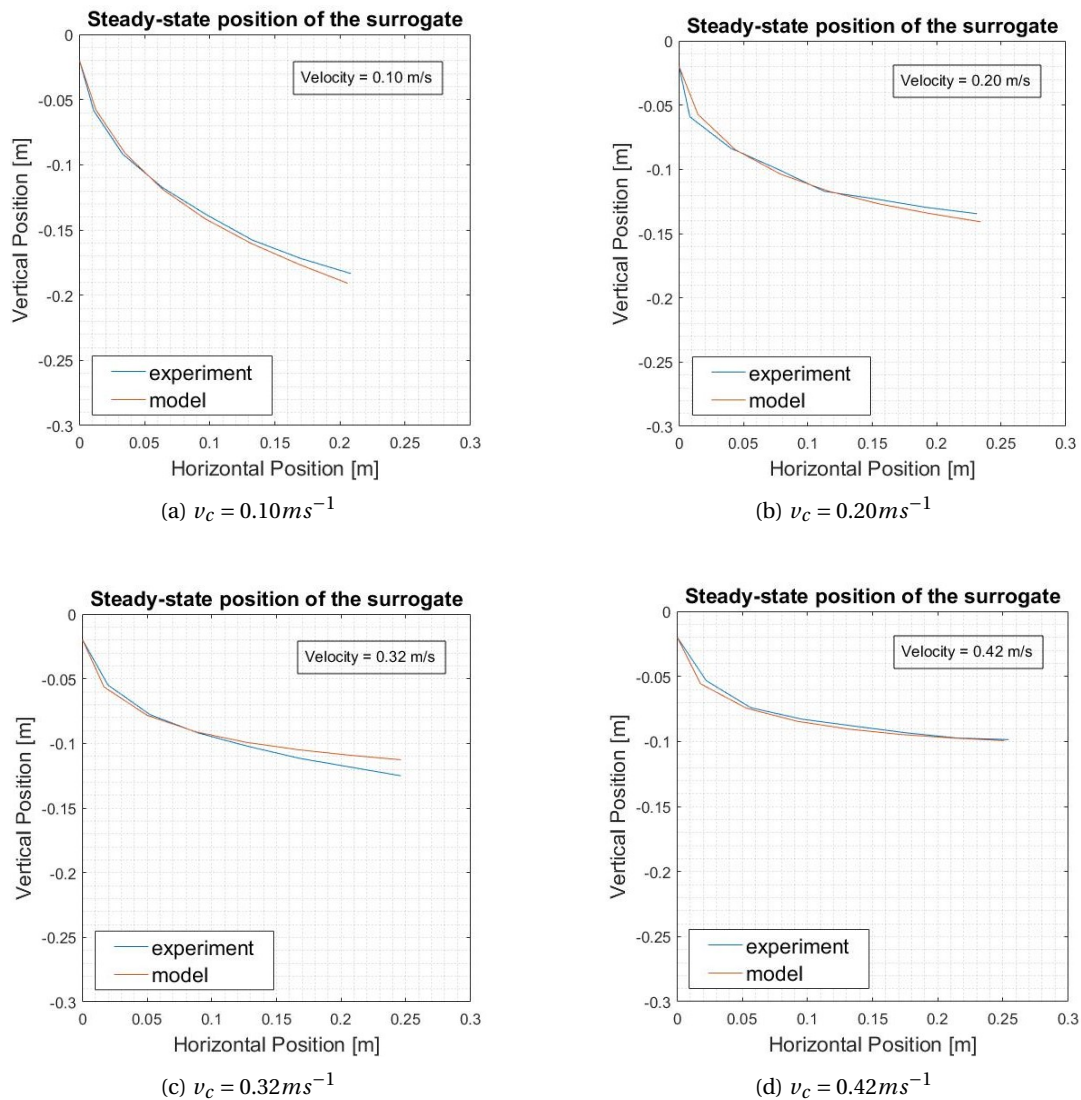


Figure 5.5: Steady-state positions comparison for different velocities

5.4.2. Force comparison

During the experiment, some groups have also been done with variable velocities. In these cases, the velocity as recorded by the velocity sensor in the experiment has been inputted into the model. The resulting output was the motion of the structures. In this process, the results of the total forces in the horizontal direction have been compared with the data that recorded by force sensor for the same velocity series. Experiment results that are based on such a velocity series are shown in Figure 5.6.

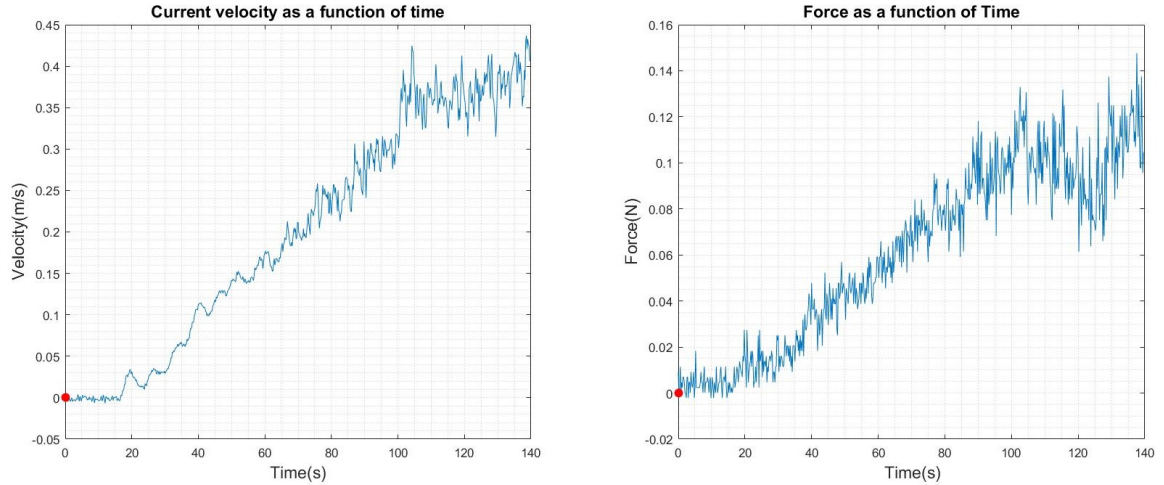


Figure 5.6: One group of velocity series and generated forces from experiment

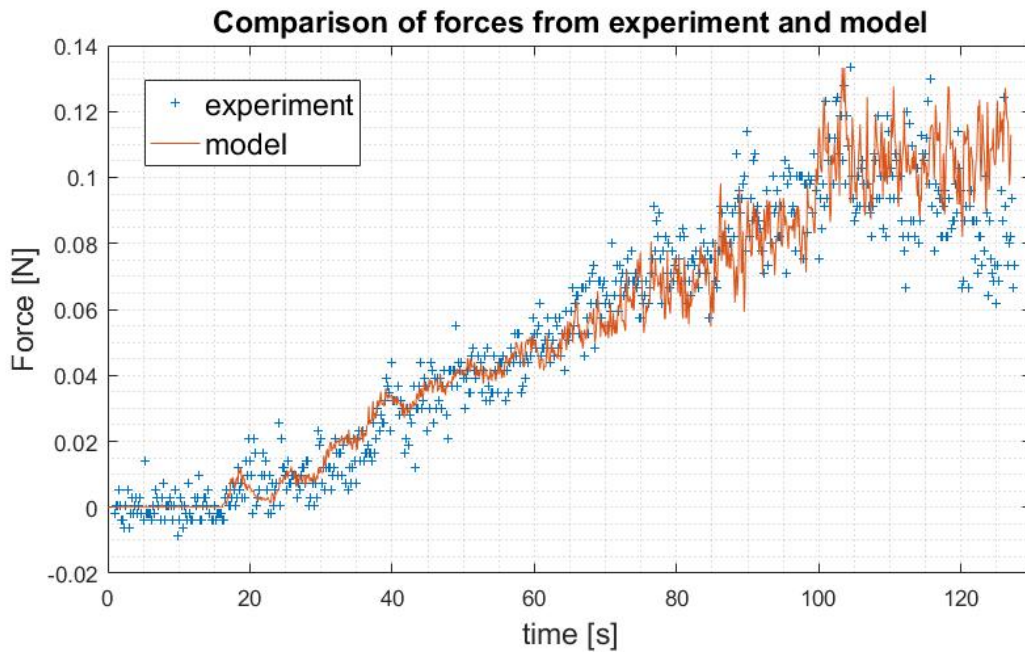


Figure 5.7: Comparison of the measured forces and simulated forces

A comparison of the measured force with the simulated model forces is shown in Figure 5.7. Basically speaking, the results from experiment have more scatter than the simulated one. It could be caused by the accidental error because of the instability and uncertainty of the experiment. However, the scatter is not large. On the other hand, the overall trend is similar and the most values from both are close. Therefore, we could say that two forces are matching favorably and the model makes an accurate prediction.

More matching between model results and experiments data to indicate the model's validity are shown in Appendix C.

6

Numerical model for further motions

As we can imagine, when the velocity of incoming flow is relatively small, the surrogate in unidirectional flow (in other words, seaweed in a natural current) will have a movement similar to the simulated movement that described in the previous chapter. We could say that this behavior is like the motion of a swing (we shall call this the first phase motion). However, if we think further, the surrogate body will get to a horizontal position when the velocity is increased to one interface velocity. In this case, the simulation model from the last chapter is not suitable anymore. This is because the motion will no longer be like a swinging motion, but more like a flutter (we shall call this the second phase motion), when the current flows in the axial direction of the body. An everyday example of this phenomenon is the flutter of the flags in the wind. In our case, the surrogate will move like Figure 6.1 showing. The geometrical characteristics of the surrogate is the same as we described in previous chapters.

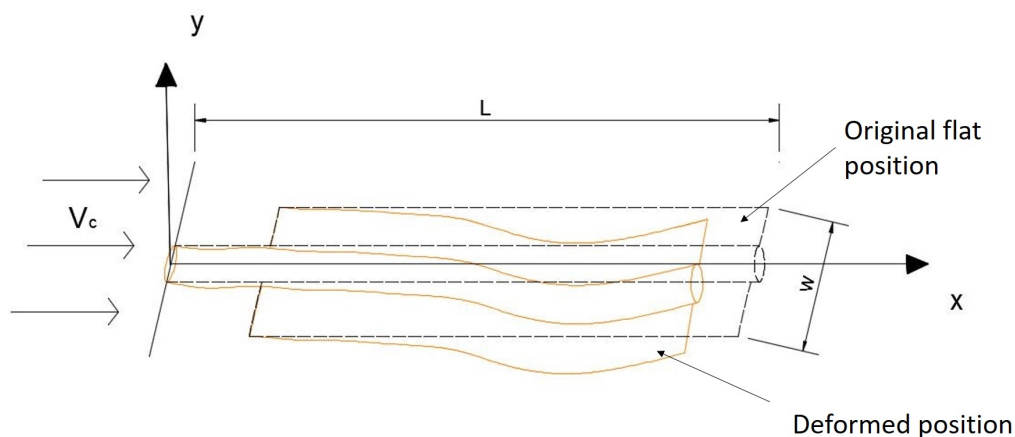


Figure 6.1: Surrogate position and movement in axial flow

These motions could be more typical for seaweeds in nature because the ocean current has a high and variable velocity. Therefore in this chapter, we will design the structure model and discuss the simulation of the surrogate body in an axial flow, along with analysis simulation results to describe the motions. On the other hand, as a cantilevered system, a nonconservative force (which is omitted in first phase motion simulation) that works on the tip of the body will be included in this model to understand how important this force is.

6.1. The structure model

The structure model is similar as the one in Chapter 5, only turned 90 degrees counterclockwise, as displayed in Figure 6.2. The horizontal position is the original flat position (initial position) of this model is as shown in

Figure 6.1 and Figure 6.2. A new coordinate system φ which stands for the angle between the central line of the body and horizontal direction, has been implemented. In this model, small displacements are assumed, so that the linear relationship which was introduced in Section 5.3.2: $\sin(\varphi) \approx \varphi$ and $\cos(\varphi) \approx 1$ are satisfied and implemented here. Similarly, for each section of the structure, it consists of a lumped mass, a rotational spring and an imaginary dashpot (not shown in the figure, but working at same location as rotational spring). When the spring rotates, it stores potential energy and exerts torque.

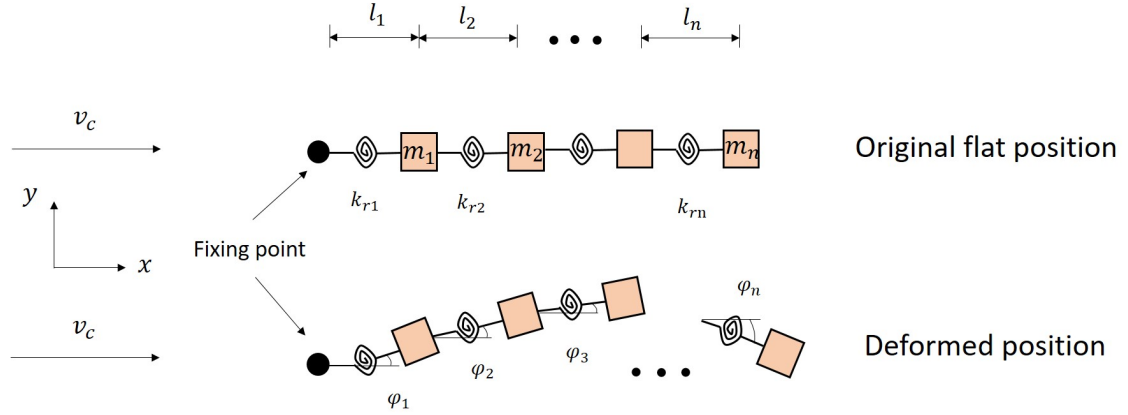


Figure 6.2: Diagram of the simplify strategy and coordinates systems for the second phase motion

The kinetic energy is the energy that the structure possesses due to the body's motion and can be represented by half of the body's mass times speed square. In this second phase motion, the kinetic energy for the structure is written as the similar form as the Equation 5.6.

$$T_{s2} = \frac{1}{2} \sum_{i=1}^n m_i \left(\sum_{j=1}^i l_j \dot{\varphi}_j \right)^2 \quad (6.1)$$

The potential energy here is stored in the spring as elastic potential energy during rotation and stored in the body as gravitational potential energy during position changes. For each section of the spring, the 'effective rotational angle' is the the angle difference between this section and last section ($\varphi_i - \varphi_{i-1}$). Based on the small angle assumption, the potential energy is decided by follow

$$V_{s2} = \sum_{i=1}^n m_i g \sum_{j=1}^i l_j \varphi_j + \frac{1}{2} \sum_{i=1}^n k_{ri} (\varphi_i - \varphi_{i-1})^2 \quad (6.2)$$

For the two equations above, subscript 's2' stands for the structural model for the second phase motion. n is the total number of the separated masses. m_i , l_i is the mass and length of the i^{th} section respectively. k_{ri} which is equal to EI/l_i is the rotational spring stiffness of the i^{th} section. Damping occurs when the rotational spring is working, thus, it will be added directly in the final EOM.

6.2. External forces

The external forces on the structure for the second phase motions can be separated into three parts. Hydrostatic forces is one of them. Another one is drag forces (form drag and skin frictional drag) which are the same as Chapter 5 described. Additionally, an inviscid hydrodynamic forces should be considered in this model which will be described in this section.

6.2.1. Hydrostatic force

As shown in the Figure 6.2, the body's motion in this phase is basically a fluttering movement, and for each section, their rotational angles are assumed to be small. Therefore, the difference of the height of each point on the structure is approximately treated as the same. In this way, the hydrostatic force for the body can be assumed to be equal to the buoyancy and does not need to be divided as demonstrated in Subsection 5.2.1. The buoyancy is directed in a vertical, upwards direction. Hence the hydrostatic forces (F_{si}) for the i^{th} section

is shown in Equation 6.3, also omitting plate part hydrostatic force due to its small thickness. In the equation, D is the cross-section diameter for the cylinder and l_i is the length of the specific section.

$$F_{si} = \frac{\pi}{4} D^2 \rho_w g l_i \quad (6.3)$$

6.2.2. Drag forces

Drag forces that are working on the structure here also include two parts, form drag (F_N in the normal direction) and skin frictional drag (F_A in the axial direction). According to small angle assumption, the expression of them working on i^{th} section may easily be found respectively as follows

$$F_{Ni} = \frac{1}{2} \rho_w A_{full} v_c^2 \sin^2(\varphi_i) (C_D)_0 \simeq \frac{1}{2} \rho_w A_{full} v_c^2 \varphi_i^2 (C_D)_0 \quad (6.4)$$

$$F_{Ai} = \frac{1}{2} \rho_w A_{full} v_c^2 \cos^2(\varphi_i) C_f \simeq \frac{1}{2} \rho_w A_{full} v_c^2 C_f \quad (6.5)$$

The meanings of parameters are the same as the description in Section 5.2.2. The only difference is the addition of the new coordinate φ here.

6.2.3. Inviscid hydrodynamic forces

The inviscid hydrodynamic forces acting on the structure has not been considered in phase one model because for phase one motions, fluid velocity is small, and hydrostatic forces dominate the whole procedure. However, they should be taken into consideration here due to the potential dynamic motion (flutter) of this phase. The inviscid force may be defined by kinetic energy (T_f) of the surrounding flow.

$$T_f = \frac{1}{2} \sum_{i=1}^n [M_{ni} (\sum_{j=1}^i l_j \dot{\varphi}_j + v_c \varphi_i)^2 + M_{Li} v_c^2] \quad (6.6)$$

Where M_{ni} is the virtual or added mass of the i^{th} section in the normal direction, and M_{Li} is the equivalent quantity for axial direction. Because the structure will be simulated in unconfined water and density of structure is just slightly larger than the water density, hence the added mass M_{ni} is assumed as 80% of the solid mass of the structure. Because we evenly separate the structure and the same mass for each section, then, the added mass is also equivalent for each section.

It is worthwhile to note that, if the both ends of the structure are fixed, the Equation 6.6 represents the entire inviscid component of the hydrodynamic forces. However, the structure that is considered here is only fixed on one end and free to move on the other. This means that we can treat this as a cantilever beam. In this case, the system is nonconservative due to the free end of the body, and hence there will be work done at the tip by a nonconservative inviscid hydrodynamic force according to [2] and [34]. It could be explained by two reasons (I) the vortex surrounding the tip of the structure and (II) the boundary layer effect at the tip of the structure. For a less-than-ideally streamlined shape, this force F_{nc} may be generated by lateral momentum and expressed as following suggested by [35] and [36].

$$F_{nc} = (1 - f) M_n v_c (\sum_{i=1}^n l_i \dot{\varphi}_i + v_c \varphi_n) \quad (6.7)$$

where M_n is the added mass for the tip section and the term in brackets is the relative velocity between structure and fluid. f is the shape parameter that can describe the degree to which the end is streamlined. It follows the relationships in Table 6.1.

From the first row of the table, for a body has an ideally streamlined end, there is no jump in velocity after the fluid passes by the cross section of the structure's tip. In this case, the nonconservative inviscid force F_{nc} does not occur because $f \rightarrow 1$ then $F_{nc} \rightarrow 0$. However in practice, the ideally streamlined shape does not exist, thus the shape parameter will variant ranging from 1 to 0. The other extreme of shape is blunt which f is equal to 0 and F_{nc} will be the largest. The shape information and flow pattern is shown in the second line of the table. Again, when the flow passes the cross-section of the structure's tip, a vortex will be generated because of the boundary layer effect. At the same time, the flow pattern will change due to the blunt end. Both of these are the sources or the determinants of the nonconservative inviscid force F_{nc} .

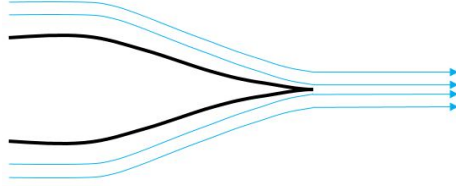
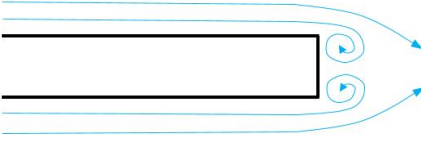
Shape of the structure tip	Graphing of the tip shape and water pattern	Shape parameter f	F_{nc}
Ideally streamlined		1	0
Blunt		0	Maximum

Table 6.1: Relationships among shape parameter f , nonconservative inviscid force F_{nc} and tip shape

6.3. Linearized equations of motion

The generalized forces (or moments) Q_i on the i^{th} mass for small angles can be determined by the force times the relative force arm as follows. This equation combines Equation 6.4, 6.5 and 6.7.

$$Q_i = a_{vi}[F_{Ai}\varphi_i - F_{Ni}\frac{\varphi_i}{|\varphi_i|} - F_{nc}] - a_{hi}[F_{Ai} + F_{Ni}\varphi_i\frac{\varphi_i}{|\varphi_i|} + F_{nc}\varphi_n] \quad (6.8)$$

where term $\frac{\varphi_i}{|\varphi_i|}$ is added here for the sign of the term and F_{nc} just works on the last section. Force arms a_{hi} and a_{vi} on the i^{th} mass can be expressed as equations below for small angles

$$a_{hi} \approx \sum_{j=1}^i l_j \varphi_j \quad (6.9)$$

$$a_{vi} \approx \sum_{j=1}^i l_j \quad (6.10)$$

Substituting Equation 6.1, 6.2, 6.6 and 6.8 into Lagrangian equation as shown below, and get n equations for n degrees of freedom system

$$Q_i = \frac{d}{dt}\left(\frac{\partial T}{\partial \dot{\varphi}_i}\right) - \frac{\partial T}{\partial \varphi_i} + \frac{\partial V_{s2}}{\partial \varphi_i}, \quad i = 1, 2, 3 \dots n \quad (6.11)$$

It should also be noted that T in Equation 6.11 should be the combination of the structure's kinetic energy and fluid's kinetic energy as

$$T = T_{s2} + T_f \quad (6.12)$$

As an example, let's consider a simple case similar to the example used in the previous chapter: a structure with three sections (i.e. $n = 3$), and one lumped mass block for each section. Mass m_i , added mass M_{ni} , Δm_i (i.e. $m_i - \rho_w V_i$) and length l_i for each section are the same. c_r is defined as a damping coefficient which is related to the viscous damping that happens when the springs are rotating. It is assumed as 70% of critical damping, hence

$$c_r = 70\% \cdot 2\sqrt{k_r m l^2} \quad (6.13)$$

Then the equations of motion for this three-DOF system are expressed as:

$$J\ddot{\Phi} + (C_s + C_f)\dot{\Phi} + (K_s + K_f)\Phi + con = Q \quad (6.14)$$

where

$$\ddot{\Phi} = [\ddot{\varphi}_1 \quad \ddot{\varphi}_2 \quad \ddot{\varphi}_3]^T \quad \dot{\Phi} = [\dot{\varphi}_1 \quad \dot{\varphi}_2 \quad \dot{\varphi}_3]^T \quad \Phi = [\varphi_1 \quad \varphi_2 \quad \varphi_3]^T \quad (6.15)$$

$$Q = [Q_1 \quad Q_2 \quad Q_3]^T \quad J = (m + M)l^2 \begin{bmatrix} 3 & 2 & 1 \\ 2 & 2 & 1 \\ 1 & 1 & 1 \end{bmatrix} \quad con = \Delta mgl [3 \quad 2 \quad 1]^T \quad (6.16)$$

$$K_s = k_r \begin{bmatrix} 2 & -1 & 0 \\ -1 & 2 & -1 \\ 0 & -1 & 1 \end{bmatrix} \quad K_f = -Mv_c^2 \begin{bmatrix} 1 & 0 & 0 \\ 0 & 1 & 0 \\ 0 & 0 & 1 \end{bmatrix} \quad (6.17)$$

$$C_s = c_r \begin{bmatrix} 2 & -1 & 0 \\ -1 & 2 & -1 \\ 0 & -1 & 1 \end{bmatrix} \quad C_f = Mv_c l \begin{bmatrix} 0 & 1 & 1 \\ -1 & 0 & 1 \\ -1 & -1 & 0 \end{bmatrix} \quad (6.18)$$

The stiffness matrix K_s (in Equation 6.17) is caused by the spring rotation that prompts the structure move back to its equilibrium position during a cycle. The matrix C_s (in Equation 6.18) is a viscous damping matrix that dissipates the energy of the system so that the vibration displacement is decreased. The matrices C_f and K_f are the damping and stiffness matrices respectively that are produced by the inviscid hydrodynamic force. Substantially, these two terms are generated by an external force, more specifically, inviscid hydrodynamic forces by the fluid. C_f plays a role of a more or less a negative damping that does positive work on the system. It means that the work done by the surrounding fluid during a cycle is converted into an extra kinetic energy that increases the extent of vibration. At the same time K_f is also negative sign matrix, which could be treated as a negative spring constant for each section. It has an opposite effect compared with K_s , that excites the model moving far away from the equilibrium position instead of restoring it back.

The matrix J (in Equation 6.16) is the inertial term, where m is related to the structure solid mass and M is the virtual or added mass that generated by surrounding fluid. The constant matrix shows the influence of the gravity, where Δm is equal to the difference of the solid mass and buoyancy contribution ($m_i - \rho_w V_i$).

6.4. Simulation results

Just like in Section 5.4 the whole structure is divided into seven sections (i.e. $n = 7$) in the second model. The model will be used to analyze the movement status and study the influence of the nonconservative force. The results are illustrated in this section.

6.4.1. Interface velocity between two models

In Chapter 5, we analyzed the first type of motion of surrogate in the experiment for the velocity from 0 to $0.42ms^{-1}$. The interface velocity from phase one motion to phase two motion is assumed around $0.57ms^{-1}$ (i.e. when the velocity reach $0.57ms^{-1}$, the structure gets into a fully horizontal position which is also the equilibrium position of the second model). And the forces from the results of two simulation models at $0.57ms^{-1}$ for the last four sections for the steady-state status are shown in the table below:

	Horizontal Force (N)	Vertical Force (N)
Model for phase 1	0.04462	0.006702
Model for phase 2	0.04460	0.006705

Table 6.2: Simulation results at interface velocity $0.57ms^{-1}$

Accordingly, as the similar results for the interface velocity point, two models can be transformed when current velocity $v_c = 0.57ms^{-1}$. However, the second model is also suitable for the velocity from 0 to $0.57ms^{-1}$ if we fix the body at the horizontal position from the beginning.

6.4.2. Movement analysis

The model was simulated in the velocity range from 0.57ms^{-1} to 2.5ms^{-1} , and the vibration characteristics were analyzed. The parameters that were used in this simulation are shown below:

Parameters	Mass (m)	length (l)	Δm	Added mass(M)
Unit	g	cm	g	g
Values	$\frac{17.1}{7}$	$\frac{30}{7}$	$\frac{2}{7}$	$\frac{11.97}{7}$
Parameters	k_r (first section)	k_r (other sections)	c_r (first section)	c_r (first section)
Unit	Nm	Nm	Nms	Nms
Values	5.804×10^{-02}	1.52×10^{-02}	6.6681×10^{-04}	3.4124×10^{-04}

Table 6.3: Parameters that are used when n is equal to seven in the second model

In Table 6.3, the stiffness constant (k) and damping constant (c) is different for the first section and other sections. This is because the stiffness of the studied object is different between the base part and other parts. The simulation results for the last section (tip) where the nonconservative inviscid force F_{nc} are acting upon are shown in Figure 6.3 (note that blue lines and orange lines in the graph are the results coming from $f = 1$ and $f = 0$ respectively).

From Figure 6.3a and 6.3b, we can know that the simulated structure is vibrating when the axial flow is coming and gradually goes into a steady-state position. On the other hand, if velocity v_c keeps increasing and exceeds 0.82ms^{-1} the structure will experience a flutter instability as Figure 6.3c, 6.3d and 6.3e show. The movement or vibration of the other sections (graphs in Appendix E) are similar as the last section vibration and their movement status also fits the velocity range for the stability which is described above.

Figure 6.4 is the vibration outlines observed from different velocities. It is clear that as the velocity increasing between 0.57ms^{-1} and 2.5ms^{-1} , the extent of vibration increases.

6.4.3. Influence of nonconservative inviscid force

As discussed before, the nonconservative force F_{nc} has not been taken into account in the first model but has been included in the second phase motion model. To understand how these forces influence the structure motions, case I: $f = 1$ (*i.e.* $F_{nc} = 0$) and case II: $f = 0$ (*i.e.* F_{nc} is maximum) were considered separately for the second model.

During the fluttering period as shown in Figure 6.3d, 6.3e and 6.3f, the difference of maximum displacement for the vibration between the two cases seems small, approximately less than 0.005rad . However, for the Figure 6.3c, which is when the smallest velocity that two cases are both fluttering, the displacement difference between them is larger than 0.01rad . On the other hand, as the velocity increases from 0.57ms^{-1} to 0.70ms^{-1} , the difference between vibration features such as the time spent to achieving a steady-state position for each case increases as well (Figure 6.3a and 6.3b), but the difference of their maximum displacements seems not increase too much. Overall, when considering F_{nc} , the extent of vibration predicted by the second model will decrease.

As F_{nc} is a force working in the direction opposite to the relative velocity direction for the structure and fluid, it can be considered to be a contribution of a positive damping. Therefore the case which considers this effects (case II) needs a larger velocity to transfer from stable movement to fluttering. This is proven by the fact that when velocity increases from $v_c = 0.75\text{ms}^{-1}$ to $v_c = 0.81\text{ms}^{-1}$, for case I flutter instability occurs, while and case II remains stable in the end. This is demonstrated in Figure 6.5, where the two velocities $v_c = 0.77\text{ms}^{-1}$ and $v_c = 0.80\text{ms}^{-1}$ are used as examples.

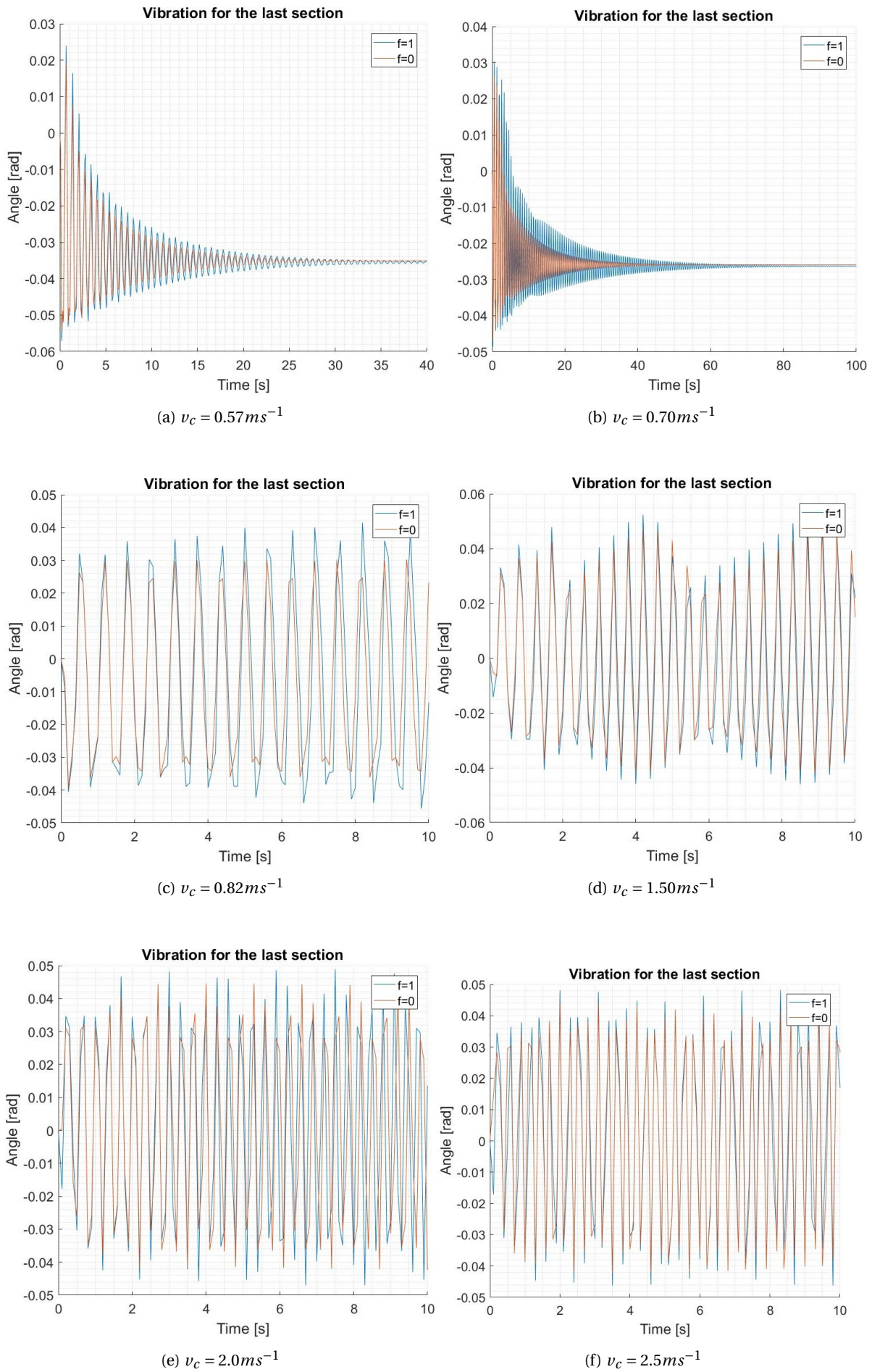


Figure 6.3: Vibration analysis (last section): case I: $f = 1$ (i.e. $F_{nc} = 0$) blue curves; case II: $f = 0$ (i.e. F_{nc} is maximum) red curves

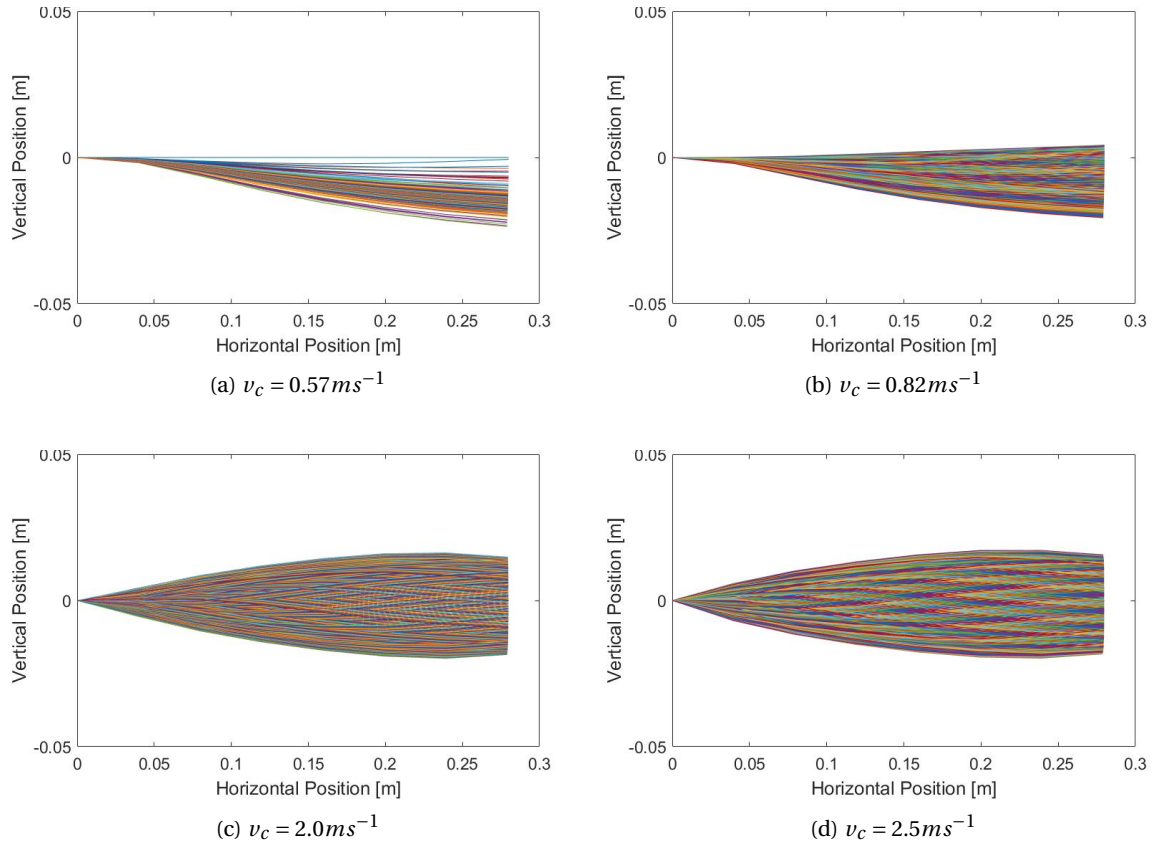


Figure 6.4: Structure fluttering outlines observed from different velocities

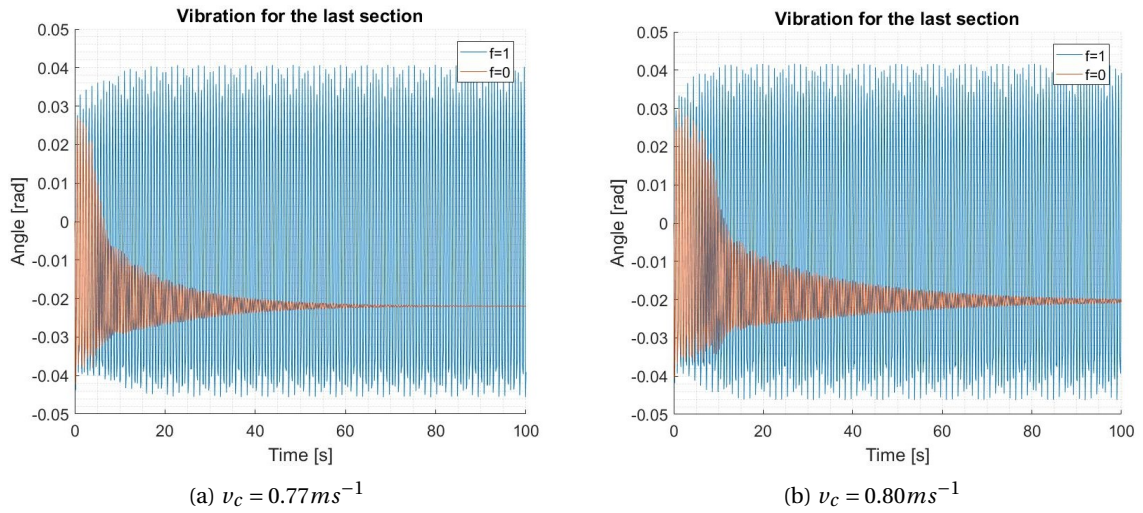


Figure 6.5: Vibration when Case I fluttering and Case II stable

Figure 6.6 displays the numbers for maximum displacement for both cases in order to understand the effect of F_{nc} specifically. The velocity interval in the graphs is $0.005 m s^{-1}$. The maximum displacement for two cases decreases gradually before velocity get $0.75 m s^{-1}$ and $0.81 m s^{-1}$ for case I and case II respectively in Figure 6.6a. These two velocities are the specific incoming current velocities for which the structure movements transform from stable to fluttering for each case. When the velocity lower than these two numbers, the

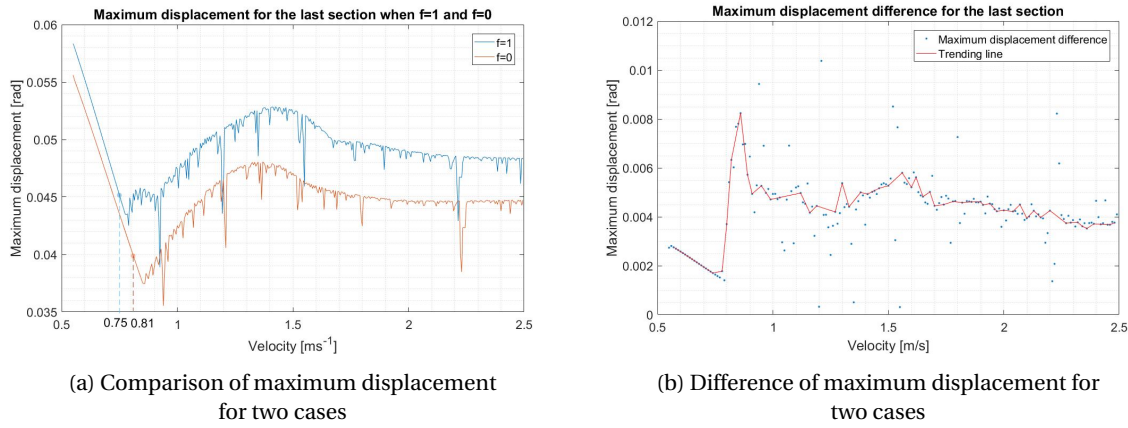


Figure 6.6: Maximum displacement analysis for two cases

maximum displacements are controlled by the influence of gravity . When the structure starts fluttering, the maximum displacement increases with increased velocity until $1.5 ms^{-1}$. Then the displacements are approximately remain unchanged. The difference of maximum displacement (blue dots) for two cases are shown in Figure 6.6. Because of the phase different for the two cases, several discrete points are observed. Red line is trending line that covers most of the data. The highest gap is around $0.01 rad$ (if taking all data into account) which occupies 26.5% of maximum displacement. Most of the gaps are less than $0.006 rad$, which is less than 15% of the maximum displacement.

Furthermore, the contributions of F_{nc} and other forces for the system are compared to understand how much this force influences the system. For example, based on results from case II, the ratio between the moments which are produced by nonconservative force F_{nc} and pressure drag force F_N ; nonconservative force F_{nc} and frictional drag force F_A for the whole structure are computed respectively for different velocities. The results are shown in Figure 6.7 where velocity interval is $0.005 ms^{-1}$.

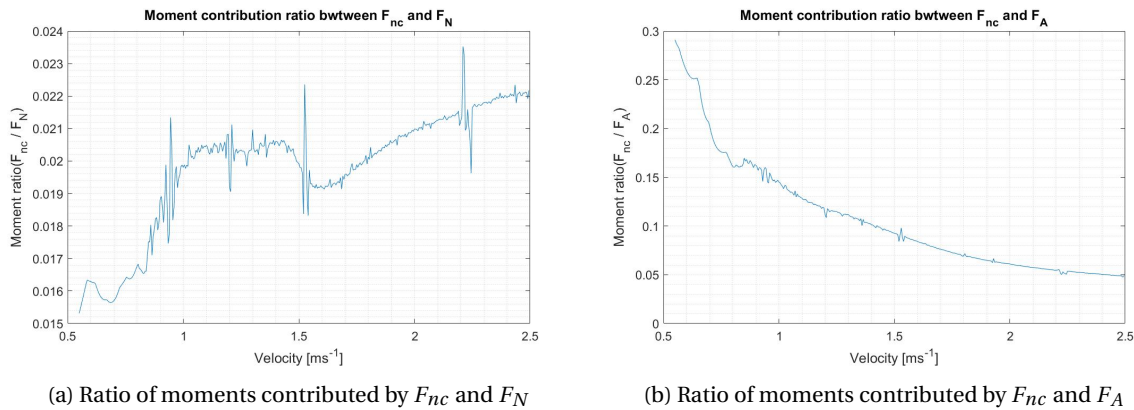


Figure 6.7: Comparison of moment contributions by different forces

From the curves, it is clear that the ratios of the contribution of F_{nc} and F_N increases with an increase in velocity. The peak ratio is approximate 2.35%. On the contrary, the ratio of the contribution of F_{nc} and F_A decreases with an increase of the velocity. The highest ratio is around 30% of the moment that generated by F_A .

7

Prediction of the moment on *Undaria pinnatifida* single blade

In Chapter 6, we discussed the movement status of the surrogate of our interested seaweed species, *Undaria pinnatifida* in axial flow. In this chapter, we will simulate and compare the maximum moment and forces that works on an individual kelp blade. In this process, the morphology of five different growing phases of *Undaria pinnatifida* is used. The data for each phase is referenced by former research and also by the measurement in the surrogate design experiment. As the size of the plant changes significantly, each growing phase should be simulated separately.

7.1. Ultimate loads on the surrogate

As we elaborated on in previous chapters, the first model is suitable for small current velocities. Considering that the moment and forces is also small when the velocity is small, we predicted that firstly the ultimate loading would be happen in the second phase motion (could be simulated by second model). Based on the second model, we can simulate the maximum moment on the whole blade for different velocities. In this simulation, the inviscid force F_{nc} is taken into account. As we discussed in Chapter 6, the surrogate turns to fluttering when the velocity of the incoming fluid exceeds 0.81 m s^{-1} (critical velocity) from a stable status.

In Figure 7.1a, the maximum moment and minimum moment (or we can call it maximum moment in the opposite direction) for different velocities is shown in blue line and orange line separately. The velocity interval is 0.01 m s^{-1} in the simulation. We can observe when the velocity exceeds the critical velocity of 0.81 m s^{-1} , maximum moment on the surrogate increases more quickly. It meaning that the increment of the maximum moment for flutter period is bigger than stable period. This could be proved by curve slope as 0.0043 and 0.1695 for stable and flutter period respectively. The maximum moment that works on the surrogate is predicted as 0.049 Nm when the largest velocity (2.5 m s^{-1}) is implemented in the simulation.

On the other hand, the ultimate vertical force on the structure has the similar trending with the ultimate moment as shown in Figure 7.1b. Before the velocity reaches critical velocity, the minimum vertical force keeps as 0 because only upward forces applied on the surrogate. Furthermore, when the velocity exceeds 0.81 m s^{-1} , maximum vertical force on the surrogate increases more quickly until reaches 0.307 N when the largest velocity (2.5 m s^{-1}) is implemented in the simulation.

The maximum and minimum horizontal force on the surrogate is shown in Figure 7.1c with small gap. In general, the horizontal force follows an exponential increase with the velocity increases. The maximum horizontal force occurs as 1.356 N when the velocity reaches 2.5 m s^{-1} . Different from moment and vertical force, there is no obviously different of trending of the horizontal force when the velocity lower or larger than the critical velocity.

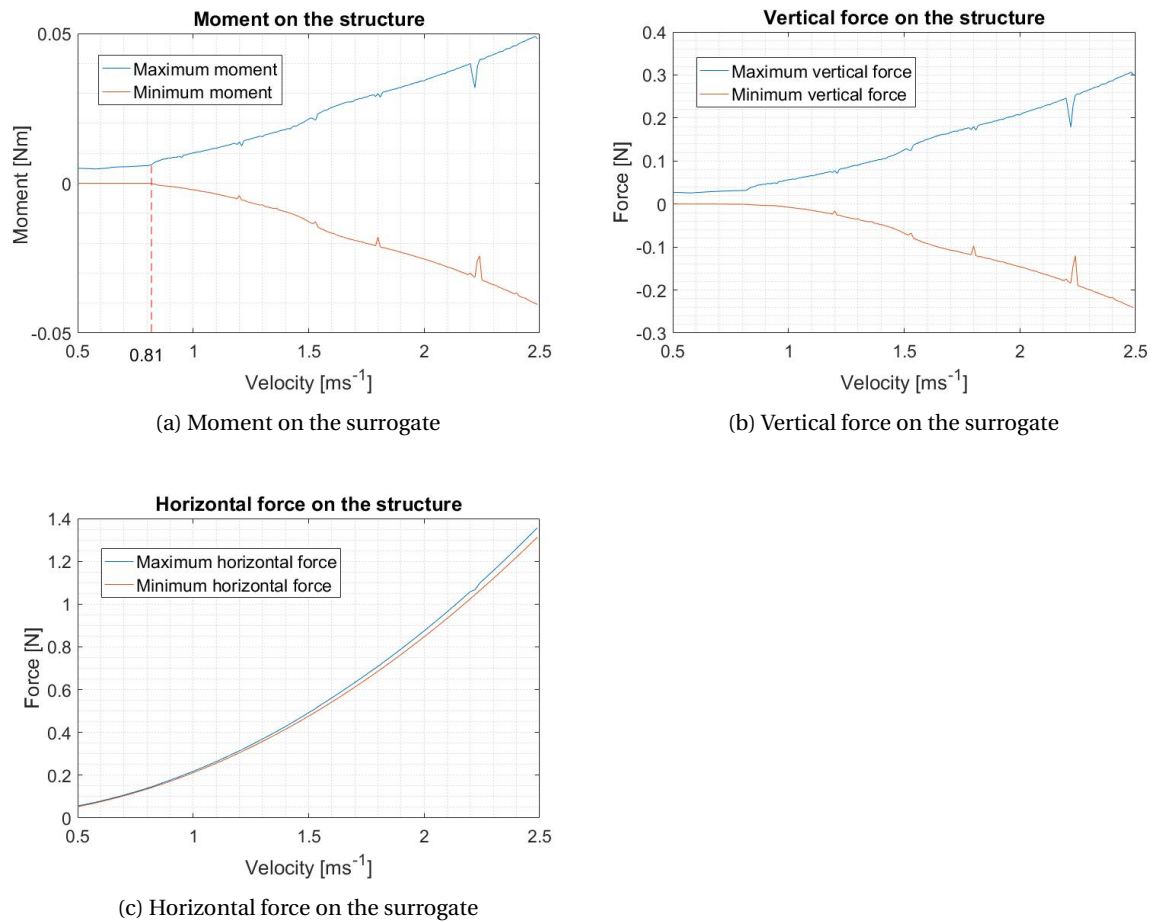


Figure 7.1: Ultimate loads on the surrogate for different velocities

7.2. Geometrical and mechanical properties of *Undaria pinnatifida* for typical growing phases

The geometry or morphology of *Undaria pinnatifida* changes quickly during its growing period. According to the research that had been done by [19], the total growing period of Wakame is around six month.

Growing phase	I	II	III	IV	V
Total length (<i>cm</i>)	40 [*]	120 ⁺	170 [*]	200 [*]	195 [*]
Base part length (<i>cm</i>)	5 [*]	20 ⁺	32 [*]	42 [*]	55 [*]
Ratio between total length and base part length	8	6	5.31	4.76	3.54
Width (<i>cm</i>)	6.13 [#]	18.4 ⁺	26.07 [#]	30.67 [#]	29.91 [#]
Weight (<i>g</i>)	20 [*]	68 ⁺	250 [*]	395 [*]	610 [*]
Density (<i>kg m</i> ⁻³)	1076.2 [#]	1076.2 ⁺	1076.2 [#]	1076.2 [#]	1076.2 [#]

Table 7.1: Morphology of *Undaria pinnatifida* for different growing phase (note: a. The numbers with superscript '^{*}' are cited from [19] b. The numbers with superscript '⁺' are as measured in the surrogate design experiment c. The numbers with superscript '[#]' are assumed, because of lack of information, by some specific reasons which are explained in the text)

Based on the research by [19] and our measurement in surrogate design experiment, the geometrical

parameters and weight of the cultured *Undaria pinnatifida* is summarized in Table 7.1. The data with superscript ‘*’ are cited from [19] who cultured and measured the Wakame in South Korea, and the numbers with superscript ‘+’ are coming from the results of the surrogate design experiment in the present study. From the second and third row of the table, our kelp specimen in the surrogate design experiment is the second phase of the growing period because its size suits of the trend of the measurement results by [19].

In the table, the fourth row, we calculated the ratio between the total length of the single thallus and the length of its base part (only the stem). The ratio decreases as the kelp grows. Furthermore, in the nature, the aspect ratio (length *vs.* width ratio) slightly changes throughout the different growing phases. An example is in the study of [5] for the seaweed *L.saccharina* which is described in Section 2.4. However, because of the lack of the information and studies of the aspect ratio for different growing phases for *Undaria pinnatifida*, and because we simplified the question, we assume this ratio for each growing phase is same as the one we tested for the second phase as 6.52. Then, we get the width in the fifth row in the table. Another property we assume is the density that keeps unchanged during the growth.

More assumptions that are used for the mechanical properties are explained next. So far, no research has been done about the stiffness of *Undaria pinnatifida* in different phases. However, during growth, if we consider the Wakame blade gets harder as the tissue matures and becomes chubbier, we can have a roughly assumption that the flexural rigidity has a 5% increase from the last phase number. The specific mechanical properties of *Undaria pinnatifida* is shown in Table 7.2.

Growing Phase		I	II	III	IV	V
Flexural rigidity ($\times 10^{-4} Nm^2$)	Base part	28.36 [#]	29.78 ⁺	31.27 [#]	32.83 [#]	34.47 [#]
	Other parts	2.55 [#]	2.68 ⁺	2.81 [#]	2.95 [#]	3.10 [#]

Table 7.2: Mechanical properties of *Undaria pinnatifida* for different growing phases (note: a. The numbers with superscript ‘+’ were measured in the surrogate design experiment b. The numbers with superscript ‘#’ are assumed, because of lack of information, by some specific reasons which are explained in the text)

7.3. Ultimate loads on *Undaria pinnatifida* for different growing phases

In this section, the simulation results of the ultimate moment and loads that work on the single blade of Wakame for the different growing phases are listed. During the simulation, the velocity interval is $0.01 ms^{-1}$.

Stichting Noordzeeboerderij has developed and trailed several types of seaweed cultivation platform in the recent years and has attained great harvest numbers. The Dutch coastal area is the main area of their trials for cultivating the kelp. To fulfill their needs, we will analyse the results of ultimate loads for the situation of the Dutch North Sea (DNS) in this section. The Netherlands is bordered by the North Sea and it has long sandy beaches. Dutch North Sea is a common designation for the south-east part of the North Sea, next to the coastal area of the Netherlands. Its abundant nutrient supplies the sea plant with a suitable growing environment.

First of all, the velocity range of the simulation is chosen. According to the research by [10], the seasonal maximum surface current velocity was predicted by a three-dimensional Circulation and Transport Model. The results show that the surface current velocity for the North Sea close to the Netherlands border is up to $1.25 ms^{-1}$.

We do not have information of the interface velocities for the plant throughout its different growing phases. Then what we did is only extend the second model for the velocity range to 0 but still set the horizontal position as its beginning or equilibrium position.

As also shown in Figure 7.1a earlier, the simulation results indicate that the maximum moment that works on an individual *Undaria pinnatifida* blade increases as the velocity increases. Figure 7.2 shows the specific moment (in positive direction) curves for five growing phases in the velocity range that we chose. We can observe from the figure that in each growing phase, a larger current velocity creates a larger moment on the seaweed blade. This is in line with the expectations, because the magnitude of the moment is positively correlated with velocity. The largest moment for each phase is pinpointed in the figure when the velocity is $1.25 ms^{-1}$.

On the other hand, with the plant growing, it will experience a larger moment as it gets larger in size. The exception is the fifth phase. It has a greater moment compared with the phase III and IV when the velocity is

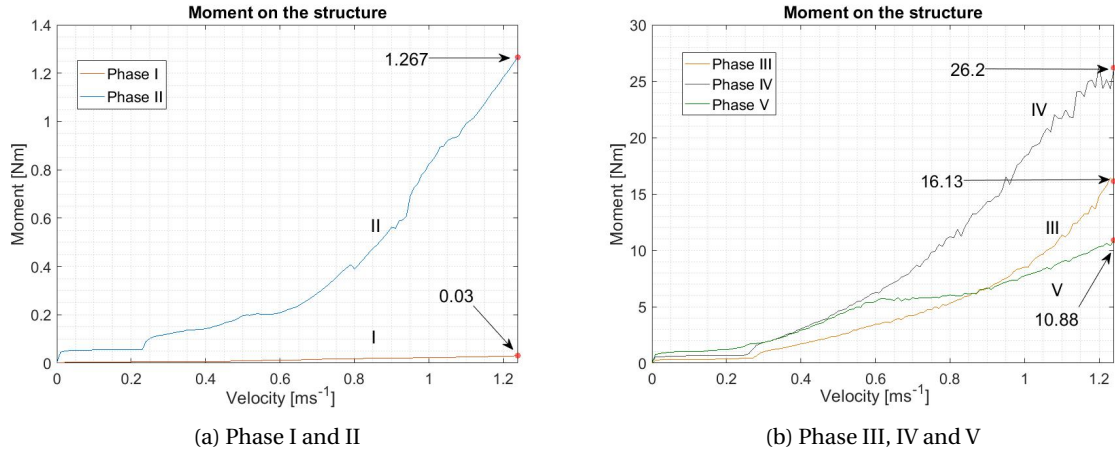


Figure 7.2: Ultimate moment on the single blade for different growing phases in DNS

smaller than 0.3ms^{-1} (approximately). However the moments in phase III and IV increase more rapidly than phase V as velocity increases. There are several explanations for this. First of all, in table 7.1, the Wakame body in phase V has a greater weight than others. Therefore, it has a lower position at the beginning because of gravity. It means that the plant has a larger frontal area facing the incoming fluid when the velocity is smaller, thus increasing the applied force or moment on the plant.

Furthermore, the fifth phase has a longer base part length but there is only a 5cm difference in total length compared with phase IV. As we know, the leaves part has a larger frontal area which helps to generate a larger moment than the base part. When the velocity increases, the influence of the plant's geometrical properties exceeds the influence of gravity. Thus the result shows that the moment for phase V is smaller than the moment for phase IV when the velocity increases. Another point of view is studying the critical velocity for different phases. Based on our assumption, the plant in phase V not only heavier but also stiffer. This influences the critical velocity between two motion status (*i.e.* stable and flutter). As we discussed in the Section 7.1, the maximum moment increment for the flutter period is larger than stable period. Therefore, this could be also an important factor that influences the moment results in the whole velocity range.

The forces on an individual Wakame blade are simulated in the same velocity range ($0\text{-}1.25 \text{ms}^{-1}$) as well. As we discussed in previous chapters, the simplification method that we used in this thesis divides the whole structure into several sections. During the simulation, the direction of the total force on each section is not the same because of the different positions of each section. Therefore, the ultimate total horizontal force and vertical force on the structure for different growing phases are simulated and the results are shown in Figure 7.3. The total force here means the summation of the form drag, the skin friction and the inviscid force on each section. The reason is that for both the form drag and the skin friction, magnitude depends on the area that faces the fluid as well as the current velocity (Equation 4.2 and 4.7). The results of both forces have the same trend as the ultimate moment and the largest forces for each phase are pinpointed in the figures when the velocity is 1.25ms^{-1} .

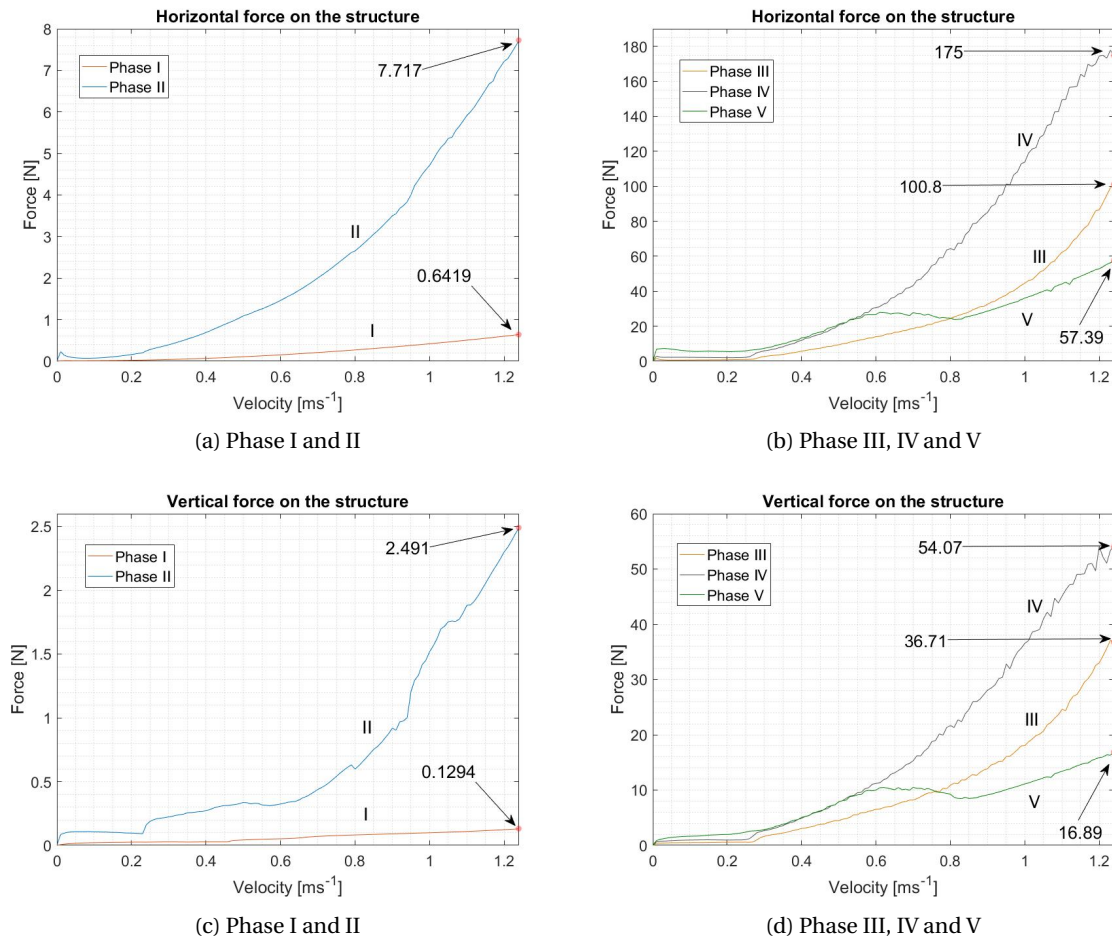


Figure 7.3: Ultimate forces on the single blade of Wakame in different growing phases in DNS

The prediction that we made of the ultimate loads happens in the second phase motion (second model) in the first section of this chapter will be discussed here. First of all, the simulation results that pinpointed in the above figures are listed in the Table 7.3 again. They are the maximum moments and loads that are predicted to happen in the second phase motion when the current velocity is reach 1.25 m s^{-1} .

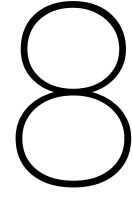
	Growing phase	I	II	III	IV	V
Moment (Nm)	0.1 m s^{-1} (transient)	0.0543	1.329	3.706	5.951	5.32
	0.2 m s^{-1} (transient)	0.2171	5.314	14.83	23.8	21.28
	1.25 m s^{-1}	0.03	1.267	16.13	26.2	10.88
Horizontal force (N)	0.1 m s^{-1} (transient)	0.2176	1.842	3.594	4.84	4.201
	0.2 m s^{-1} (transient)	0.8704	7.369	14.38	19.36	16.8
	1.25 m s^{-1}	0.6419	7.717	100.8	175	57.39

Table 7.3: Moment and horizontal force comparison of 0.2 m s^{-1} and 0.1 m s^{-1} (first model) and 1.25 m s^{-1} (second model)

Alternatively, the ultimate force from the first phase motion can be understood from the following. During the first motion, if there is no velocity, the plant will not moving, oriented down and straight forward. In this case, the highest loads (or the transient loads) on the plant will be happen if a certain current incidents (with a certain velocity) and contacts the body at the first moment. That is because at that instantaneous moment,

the effective contact area between them is the biggest. The area becomes smaller when the plant body starts swinging. In nature, the current velocity changes gradually, whereas we just need to check small current velocities to determine the ultimate loads in the first phase motion.

In the table, the results of the maximum moment and horizontal force are listed for different phases at the current velocity is 0.1ms^{-1} and 0.2ms^{-1} . This two circumstances mean that the current velocity immediately jumps from 0 to 0.1ms^{-1} and 0.2ms^{-1} respectively and impacts the plant that not moving. Because the loads applied on the last three phases are much larger than the loads applied on the first two phases, here we focus on those three groups of results. From the results, when the current velocity is 0.1ms^{-1} , the transient loads are all smaller than the ultimate loads that happen at 1.25ms^{-1} . Furthermore, the results are the same for the current velocity of 0.2ms^{-1} , except the transient moment on phase V. In this case, the transient moment is two times larger than the maximum moment that occurs at 1.25ms^{-1} . In addition, the horizontal forces at 1.25ms^{-1} are all larger than the transient forces. Therefore, our expectation is not totally correct. When one wants to predict the ultimate loads on the structure, it is worthwhile to check the transient force when the current suddenly hits the plant. Although the velocity is initially small, it could cause larger loads than great velocities.



Discussion and conclusion

8.1. Discussion

The fact that the specimens used in the experiment varied in size and shape influence the conclusions we can draw from the physical parameter measurements. This inhomogeneity of the seaweed will be enhanced by the place where it was growing (offshore, inter-tidal zone, etc.) or its growing phase when it was harvested. It is confusing or inaccurate to describe the characteristics of one species of seaweed by some simple parameters like diameters or thickness as used in this paper. This could be solved by increasing specimen quantity to get the results more generally or add other parameters to describe the morphology of the seaweed.

The Wakame surrogates designed for this paper are morphologically simplified, especially for the leaves parts. As shown in Figure 1.1a, the leaves are not continuous, which avoids forming vortexes by changing its position to a more streamlined form to comply with the fluid. Thus, the simplified leaf part is not strictly correct and could increase the force on the body. Furthermore, when designing the proxy as described in Chapter 3, the stalk of the plant was also simplified in this thesis. We assume that the surrogate of the stalk could be built by two parts with same stiffness for each, I. base part and II. others, because stiffness across other parts except the base parts are similar. In reality, stiffness in II is actually lower and get lowest stiffness at the tip, so the assumption for simplification is imprecise. However, considering our design strategy, if we subdivided II to subsections, the connecting point between two parts will also greatly influence stiffness. Therefore, we decided to use evenly stiffness for II in the end.

During the current experiment, there are some details may cause errors, for example, a wall effect. It is not taken into account when dealing with data coming from the trial and it is not precise. Due to the narrowness of the flume (45cm), the surrogate is installed near the wall, thereby the velocity on one edge of the surrogate which closer to the wall is smaller than another edge, and it will cause slight rotation and decrease frontal area face to incident flow. This means that the results for the measured point in Figure 4.6b are slightly larger. Other errors may be caused by (I) assumption of the same velocity around surrogate and (II) the reflection fluid from another end of the flume, but for both of them, the impact is minimal.

The methodology to get drag coefficients that obtained from the experiment is introduced in Chapter 4. The maximum coefficient $(C_D)_{90}$ is defined as 1.98 as suggested by [17] for a rectangular shape sheet with a high aspect ratio. However, concerning the characteristics of surrogate which is used in this experiment, the sheet part of the surrogate is less stiff, which is meaning that the corner (or edge) of the sheet may be rolled up a bit by the flow and then the force on it will decrease. Accordingly the coefficient $(C_D)_{90}$ should be slightly less than 1.98. Furthermore, when computing the horizontal and vertical drag coefficients, the current velocity was divided into two directions, and the coefficients were calculated by these separated velocities which are less accurate. It is advised to find a relationship (coefficient) between full current velocity and forces in a certain direction and divide the forces to horizontal and vertical directions after that.

In Chapter 7, we confirmed the geometrical and mechanical properties of the individual *Undaria pinnatifida* thallus. The morphology data is cited from previous research and our own experiment measurement results. At the same time, some assumptions are made because the existing research has not provided us with sufficient knowledge. For example, we assumed that the aspect ratio of the kelp is unchanged for different growing phases. However, like we talked about for *L.saccharina*, the ratio does change, which may influence the simulation results. On the other hand, due to the reason that we consider the tissue of the seaweed body

matures and turns chubby, we assumed the stiffness of the kelp increases 5% for each growing phase. However, this percentage is totally based on the ‘feeling’ and without any academic support. In reality, the stiffness may have a nonlinear increasing rate during growing period. More research about the exact geometrical and mechanical properties for the *Undaria pinnatifida* that in different growing phases is needed to produce more accurate estimations on its movement status and applied loads.

8.2. Main conclusions

In this paper, two species of seaweed, *Undaria pinnatifida* (Wakame) and *Laminaria saccharina* have been measured for their physical characteristics and also for surrogate materials. Surrogates were designed for both species of interest. These were tested in an experiment in a current flume, in order to research their hydrodynamic characteristics and behaviour in currents. Due to their behavior from the experiment, we can conclude that *Undaria pinnatifida* moves in planar motions, and that *Laminaria saccharina*’s movement is more three-dimensional. In the end, *Undaria pinnatifida* was chosen as a focus species and its pressure drag coefficient and frictional drag coefficient was obtained. Additionally, two numerical models were designed for simulating the movement and loads for the surrogate and Wakame in the current.

8.2.1. Hydrodynamic coefficients

The method used in this paper, which considers the changing project area to deviate drag coefficient, is more rigorous than previous research which only considers the full frontal area. Based on the pattern of horizontal and vertical drag coefficient curves, the maximum horizontal drag force on the seaweed blade happens at the time when the fluid hit the blade perpendicularly, and the maximum vertical drag force on the blade will occur when attack angle is around 55° .

8.2.2. Two numerical models

Two numerical models are designed to simulate motions of the surrogate in the experiment for different velocity ranges for two motion phases such as from 0ms^{-1} to 0.57ms^{-1} and from 0.57ms^{-1} to 2.5ms^{-1} separately. The results of the first model match well with the experiment results.

These two numerical models, which are based on MATLAB ordinary differential equations solver (ode45), could be further used on other engineering time-domain simulation software as a package to simulate and predict the movement of *Undaria pinnatifida* (Wakame) and the loads that work on it. It could be also used for other seaweed species with similar morphology. To be specific, this can be done by inputting stiffness and size parameters as well as the number of sections that separate the whole seaweed blade in the model. In this way, the motions of other, similar species could also be predicted by the models.

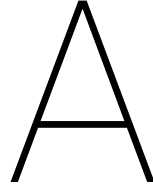
8.2.3. Influence of nonconservative force

As we observed from the experiment that was described in Section 4.2, the surrogate vibrated itself chaotically around its steady-state position. This vibration could be caused by the shedding vortex. Thus, through this phenomenon, we can see the effect of the nonconservative inviscid force F_{nc} in the first phase motion. However, the displacement of the vibration is very small, so it can not be observed clearly. It could be proved from the analyzation of the influences of the force F_{nc} in Section 6.4.3 by studying the simulation results. Both the difference of maximum displacement and generated moment because of force F_{nc} are small (or occupied less compared with pressure drag force F_N). This is true particularly when the velocity is too low to cause the structure to flutter, say, like $v_c < 0.81\text{ms}^{-1}$ shown in Figure 6.3a and 6.3b. Therefore, for the first phase model (velocity range is 0 to 0.57ms^{-1}) which omits inviscid force F_{nc} , the results are correct and reliable.

When velocity exceeds 0.57ms^{-1} , the second model will be implemented. Similarly, nonconservative inviscid force F_{nc} will not have a large influence when the velocity is smaller than $v_c = 0.81\text{ms}^{-1}$ which is the point that the structure changes movement status. However, when velocity increases further, although the maximum displacements trends to be stable, the difference of maximum displacement increases two times. In the meantime, as one of the restoring ‘damping force’, F_{nc} affects the critical velocity between two movement status (stable and flutter instability) and decreases the displacement for fluttering (although not severe). Also considering when the model be extended into real seaweed simulations, the difference in vibration displacement will consequently influence whether the plant tissue will be broken or not in specific situations. Accordingly, this force is worthwhile to be included in the second model.

8.2.4. Prediction of the ultimate moment and loads on *Undaria pinnatifida*

The moment and forces on *Undaria pinnatifida* for different growing phase is predicted in order to fulfill the aim of the Stichting Noordzeeboerderij. In a nutshell, the moment and forces that works on the individual kelp blade increases with the current velocity, as it increases ranging from 0 to 1.25m s^{-1} . The result shows us the ultimate moment, horizontal force and vertical force for the integral life of the plant is as 26.2Nm , 175N and 54.07N separately in the Dutch North Sea. For different growing phases, the ultimate moment and loads are depend on the the geometrical of the body (such as length, width etc.). It also depends on the weight and the stiffness of the plant body because these are important parameters that decide the moment status of the body.



Physics parameters for surrogate materials

In this appendix, the original measured data is listed here for materials such as tubes and plastic sheets which are shown in Figure 3.3. Data in this appendix is for tube samples with 15cm of length and plastic sheet samples with 15cm of length, 5cm of width. The standard deviation for tubes parameters is omitted here because, for silicon tubes, their morphology is homogeneous with small standard deviation. Density in the table is for one piece.

Parameters	Flexural rigidity	Bending modulus	Outer diameter	Inner diameter	Mass	Density
Symbols	J	E	D_o	D_i	m	ρ
Units	($\times 10^{-4} Nm^2$)	(Mpa)	(mm)	(mm)	(g)	(kg/m^3)
A	126.71	24.40	15.67	11.58	12.83	21.99
B (tube I)	26.70	31.77	10.13	7.79	5.36	24.41
C	10.01	27.58	8.00	5.81	3.41	21.53
D	7.95	39.47	6.90	5.00	2.72	22.98
E	3.59	163.47	4.11	3.21	1.00	28.99
G	2.76	25.56	6.28	5.10	1.73	24.60
D, B	34.26	28.18	10.13	5.00	8.08	19.88
B, A	350.63	50.47	15.67	7.79	18.19	18.79
E, D	9.64	36.36	4.11	3.21	3.72	107.84
F, E	4.02	116.91	4.11	1.53	1.43	18.77
E, G	3.80	21.35	6.28	5.10	2.73	38.83
G, B	27.94	23.11	10.13	5.10	7.09	12.71
G, B, E, F (tube II)	29.02	22.47	10.13	5.10	8.52	21.24
E, G, F (tube III)	3.80	19.97	6.28	1.53	3.16	16.27

Table A.1: Physics parameters for tubes and tubes combinations

Parameters	Flexural rigidity J	Bending modulus	Thickness
Symbols	J	E	t
Units	($\times 10^{-4} Nm^2$)	(Mpa)	(mm)
A	2.71± 0.43	11872.68±1860.92	0.19
B	4.48±1.15	39810.55±10232.05	0.15
C	2.12± 0.49	12920.92± 2971.12	0.17
D	3.32± 1.09	17099.38± 5614.46	0.18
E	4.16± 1.28	45489.41± 13948.72	0.14
F (Plastic sheet II)	2.18± 0.79	23885.98± 8628.78	0.14
Double A (Plastic sheet I)	41.75± 7.18	22825.00± 3925.20	0.38

Table A.2: Physics parameters for plastic sheets (\pm standard deviation)

Surrogates for two types of seaweed are designed and constructed. Figure A.1 shows two types of surrogate respectively. Their sizes are follow the numbers in Figure 3.4 and Table 3.1.

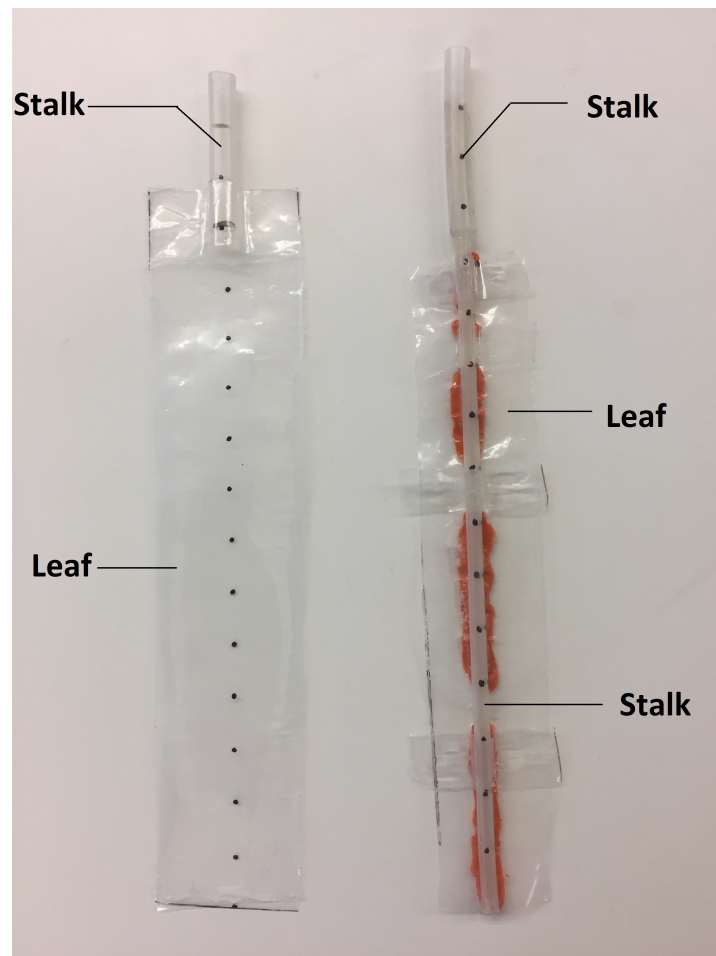


Figure A.1: Surrogate of seaweed *Laminaria saccharina* (Left) *Undaria pinnatifida* (right)

B

Raw data from the experiment

Several groups of the raw data from the experiment are showing here in figures to give an overview of the procedure of tests and relationship between velocity and measured forces. Such as in Figure B.1a and B.1c, contains the velocity recording during of experiment for each group. Also, the measured force as a function of velocity showing in Figure B.1b and B.1d.

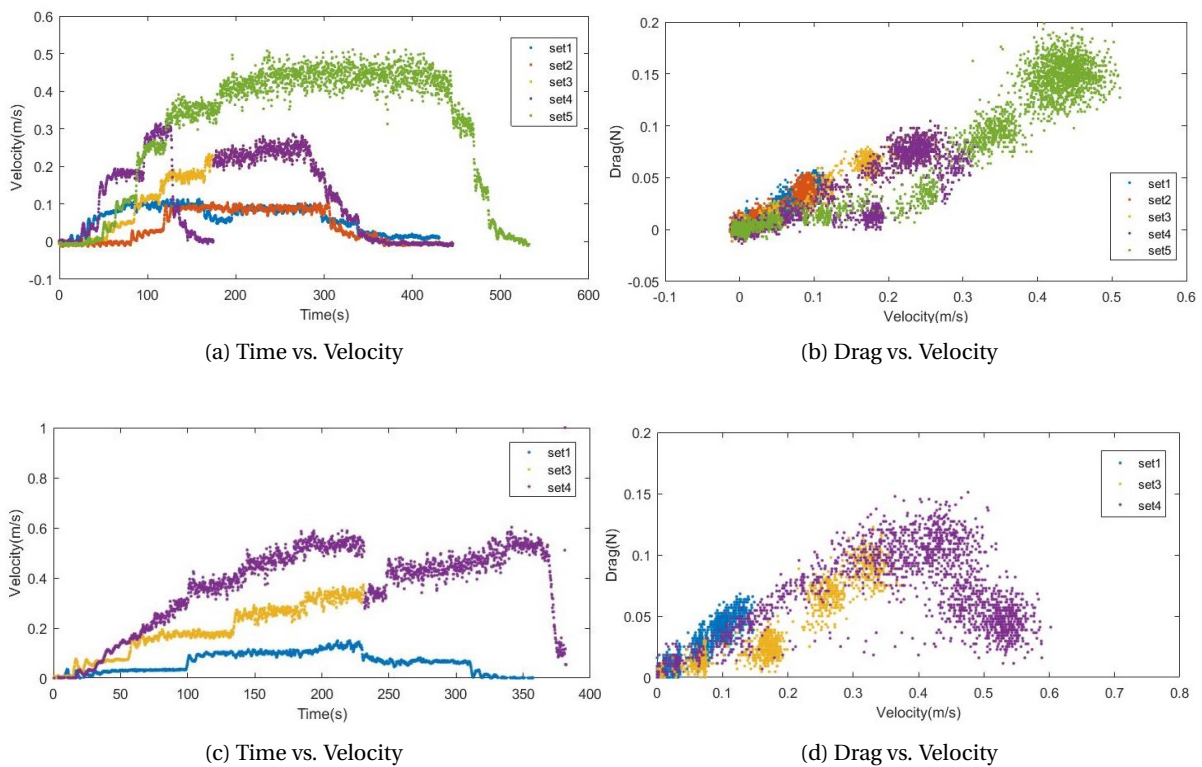


Figure B.1: Several groups raw data of the experiment

C

Matching between model results and experiment results

There are more simulation results for Chapter 5 of different experimental groups to proving the matching between the first model and experiment. The comparison form is as the same as Figure 5.7. In some groups, the velocity was changed fluctuation like Figure C.1, C.2 and C.3 or the other groups velocity increasing constantly like Figure C.5 for proving the well matching between the model results and experiment results. In group 4 after 200s, an apparent difference was observed. Difference results of the force could be caused by the high water level during the trial which hitting the force sensor. For others, the water level was controlled perfectly that submerging the surrogate but not contacting with force sensor.

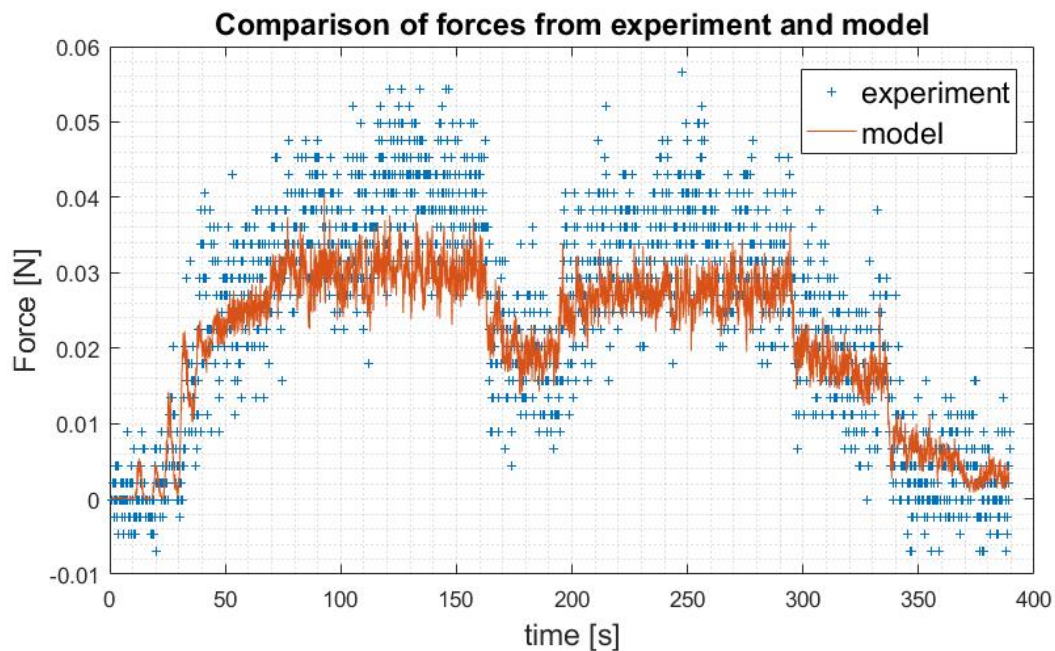


Figure C.1: Matching between model result and experiment (Group 1)

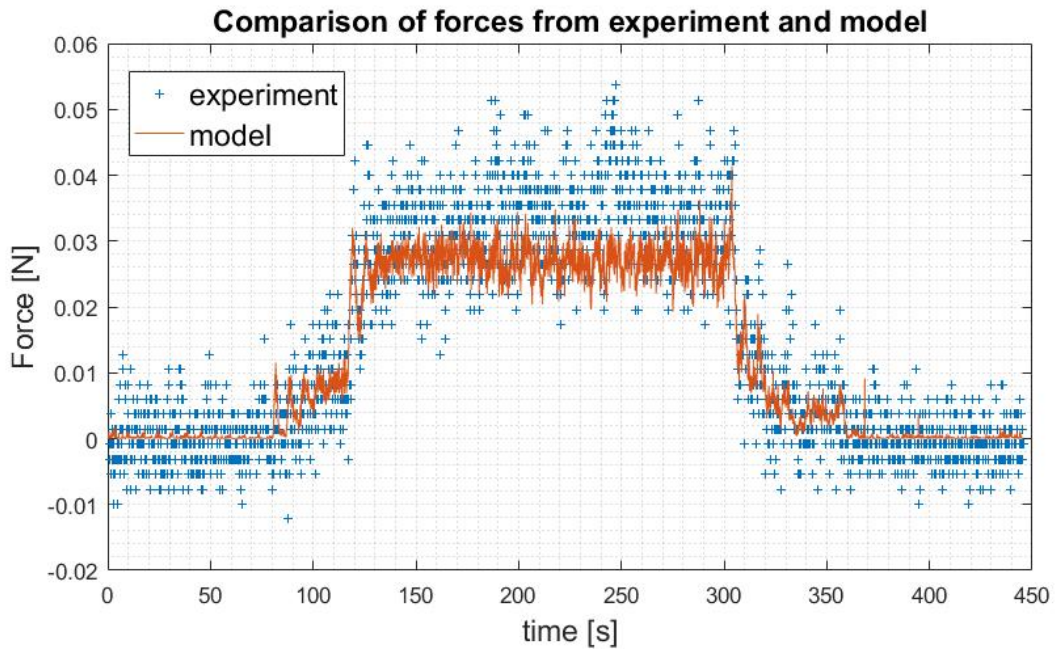


Figure C.2: Matching between model result and experiment (Group 2)

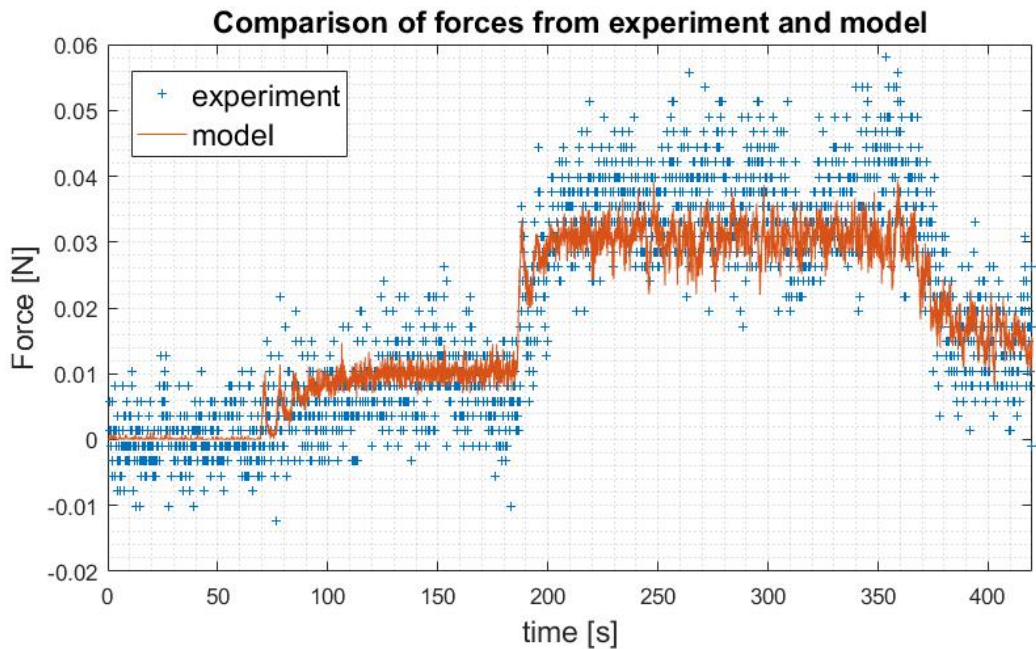


Figure C.3: Matching between model result and experiment (Group 3)

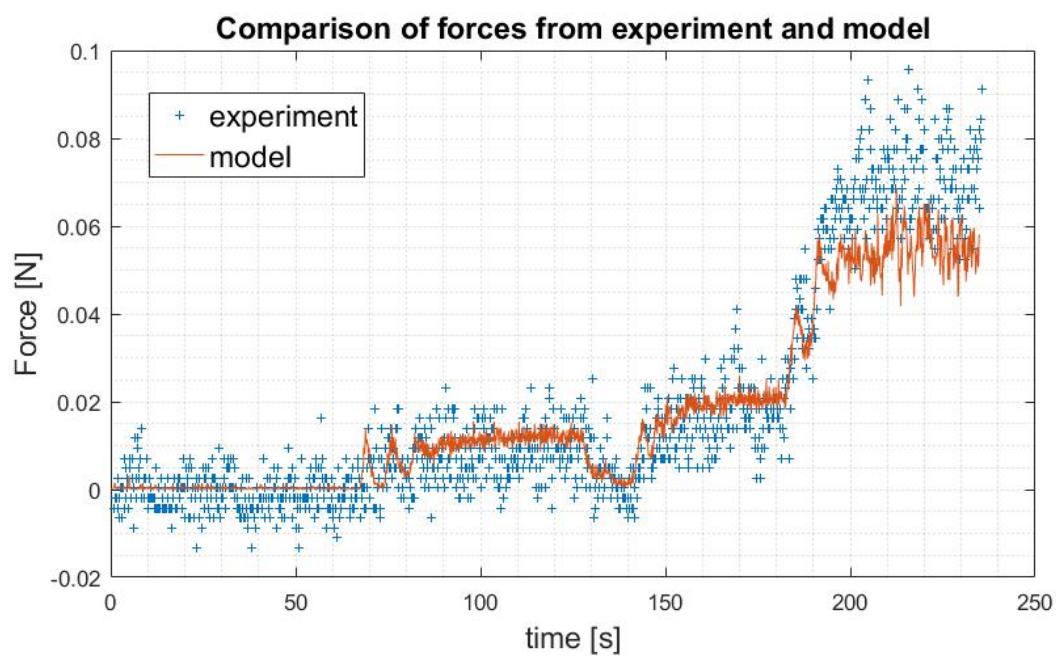


Figure C.4: Matching between model result and experiment (Group 4)

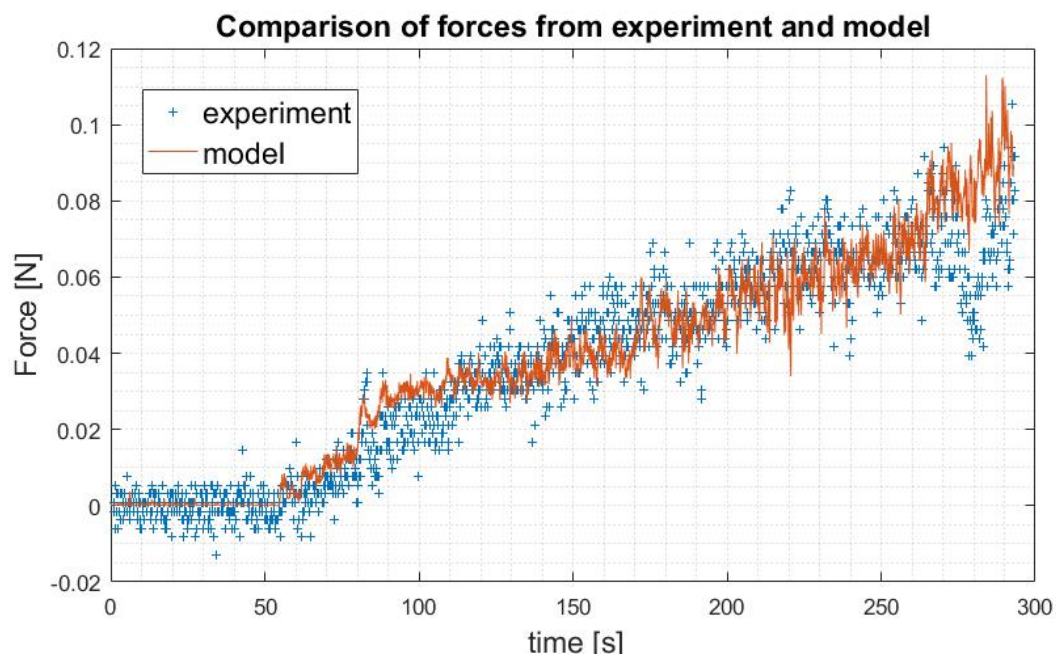
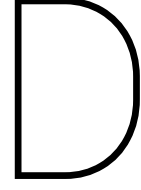


Figure C.5: Matching between model result and experiment (Group 5)



EOM derivation by Lagrangian mechanics

In Chapter 5 and Chapter 6, some summation equations were shown for Lagrangian mechanics for our models. In this appendix, the specific processes of the Lagrangian mechanics to derive equations of motion are shown in two sections. For simplification of the question, the process that shown here also focus on three masses system (i.e. dividing the structure into three sections) like the example in the chapters.

D.1. Lagrangian mechanism for the first model

As we discussed in Chapter 5, the coordinate system (θ) of the first model is shown in Figure 5.1. When the Lagrangian mechanics method is implemented to derived the equations of motion, the kinetic energy and potential energy should be figured out. Therefore, the velocity for each mass is required. It can be expressed as

$$v_1 = l_1 \dot{\theta}_1 \quad v_2 = l_1 \dot{\theta}_1 + l_2 \dot{\theta}_2 \quad v_3 = l_1 \dot{\theta}_1 + l_2 \dot{\theta}_2 + l_3 \dot{\theta}_3 \quad (D.1)$$

where l_i is the length of the i^{th} section. The term $\dot{\theta}$ is the rotational velocity for each mass. Then the kinetic energy T for the whole structure is:

$$T = \frac{1}{2} m_1 v_1^2 + \frac{1}{2} m_2 v_2^2 + \frac{1}{2} m_3 v_3^2 = \frac{1}{2} m_1 (l_1 \dot{\theta}_1)^2 + \frac{1}{2} m_2 (l_1 \dot{\theta}_1 + l_2 \dot{\theta}_2)^2 + \frac{1}{2} m_3 (l_1 \dot{\theta}_1 + l_2 \dot{\theta}_2 + l_3 \dot{\theta}_3)^2 \quad (D.2)$$

where m_i is the mass of the i^{th} section. The potential energy V for each mass is shown in three equations, where k_i is the rotational spring constant for the i^{th} spring.

$$\begin{aligned} V_1 &= m_1 g l_1 (1 - \cos \theta_1) + \frac{1}{2} k_1 \theta_1^2 \\ V_2 &= m_2 g [l_1 (1 - \cos \theta_1) + l_2 (1 - \cos \theta_2)] + \frac{1}{2} k_2 (\theta_2 - \theta_1)^2 \\ V_3 &= m_3 g [l_1 (1 - \cos \theta_1) + l_2 (1 - \cos \theta_2) + l_3 (1 - \cos \theta_3)] + \frac{1}{2} k_3 (\theta_3 - \theta_2)^2 \end{aligned} \quad (D.3)$$

The Lagrangian mathematical function L is equal to:

$$L = T - V = T - V_1 - V_2 - V_3 \quad (D.4)$$

Then the following equations are deviated:

$$\begin{aligned} \frac{dL}{d\theta_1} &= -m_1 g l_1 \sin(\theta_1) - m_2 g l_1 \sin(\theta_1) - m_3 g l_1 \sin(\theta_1) - k_1 \theta_1 + k_2 (\theta_2 - \theta_1) \\ \frac{dL}{d\theta_2} &= -m_2 g l_2 \sin(\theta_2) - m_3 g l_2 \sin(\theta_2) - k_2 (\theta_2 - \theta_1) + k_3 (\theta_3 - \theta_2) \\ \frac{dL}{d\theta_3} &= -m_3 g l_3 \sin(\theta_3) - k_3 (\theta_3 - \theta_2) \end{aligned} \quad (D.5)$$

$$\begin{aligned}
\frac{d}{dt} \left(\frac{dL}{d\dot{\theta}_1} \right) &= m_1 l_1^2 \ddot{\theta}_1 + m_2 (l_1 \ddot{\theta}_1 + l_2 \ddot{\theta}_2) l_1 + m_3 (l_1 \ddot{\theta}_1 + l_2 \ddot{\theta}_2 + l_3 \ddot{\theta}_3) l_1 \\
\frac{d}{dt} \left(\frac{dL}{d\dot{\theta}_2} \right) &= m_2 (l_1 \ddot{\theta}_1 + l_2 \ddot{\theta}_2) l_2 + m_3 (l_1 \ddot{\theta}_1 + l_2 \ddot{\theta}_2 + l_3 \ddot{\theta}_3) l_2 \\
\frac{d}{dt} \left(\frac{dL}{d\dot{\theta}_3} \right) &= m_3 (l_1 \ddot{\theta}_1 + l_2 \ddot{\theta}_2 + l_3 \ddot{\theta}_3) l_3
\end{aligned} \tag{D.6}$$

where the term $\ddot{\theta}$ is the acceleration for each mass. When we evenly separate the whole structure into three sections, the following parameters satisfies the relationship that is shown below:

$$m_1 = m_2 = m_3 = m \quad l_1 = l_2 = l_3 = l \quad k_1 = k_2 = k_3 = k \tag{D.7}$$

Then the final equations of motion can be derived as follows:

$$\begin{aligned}
EOM_1 : \frac{d}{dt} \left(\frac{dL}{d\dot{\theta}_1} \right) - \frac{dL}{d\theta_1} &= 3ml^2 \ddot{\theta}_1 + 2ml^2 \ddot{\theta}_2 + ml^2 \ddot{\theta}_3 + 3mgl \sin \theta_1 + 2k\theta_1 - k\theta_2 = Q_1 \\
EOM_2 : \frac{d}{dt} \left(\frac{dL}{d\dot{\theta}_2} \right) - \frac{dL}{d\theta_2} &= 2ml^2 \ddot{\theta}_1 + 2ml^2 \ddot{\theta}_2 + ml^2 \ddot{\theta}_3 + 2mgl \sin \theta_1 + 2k\theta_2 - k\theta_1 - k\theta_3 = Q_2 \\
EOM_3 : \frac{d}{dt} \left(\frac{dL}{d\dot{\theta}_3} \right) - \frac{dL}{d\theta_3} &= ml^2 \ddot{\theta}_1 + ml^2 \ddot{\theta}_2 + ml^2 \ddot{\theta}_3 + mgl \sin \theta_1 + k\theta_3 - k\theta_2 = Q_3
\end{aligned} \tag{D.8}$$

where Q_1, Q_2, Q_3 are external moments that are expressed in Section 5.2. After add the viscous damping terms (same formation as the stiffness terms), three equations are expressed as:

$$\begin{aligned}
EOM_1 : 3ml^2 \ddot{\theta}_1 + 2ml^2 \ddot{\theta}_2 + ml^2 \ddot{\theta}_3 + 2c\dot{\theta}_1 - c\dot{\theta}_2 + 2k\theta_1 - k\theta_2 + 3mgl \sin \theta_1 &= Q_1 \\
EOM_2 : 2ml^2 \ddot{\theta}_1 + 2ml^2 \ddot{\theta}_2 + ml^2 \ddot{\theta}_3 + 2c\dot{\theta}_2 - c\dot{\theta}_1 - c\dot{\theta}_3 + 2k\theta_2 - k\theta_1 - k\theta_3 + 2mgl \sin \theta_2 &= Q_2 \\
EOM_3 : ml^2 \ddot{\theta}_1 + ml^2 \ddot{\theta}_2 + ml^2 \ddot{\theta}_3 + c\dot{\theta}_3 - c\dot{\theta}_2 + k\theta_3 - k\theta_2 + mgl \sin \theta_3 &= Q_3
\end{aligned} \tag{D.9}$$

D.2. Lagrangian mechanism for the second model

The equations of motion that describe the movement of the model for the second phase motion which we considered in Chapter 6 are deviated in this section with detail steps. The coordinate system (φ) is shown in Figure 6.2. The processes that shown here also focus on three mass system like the example in the Chapter 6. The velocity of each mass is shown as follow:

$$v_{s1} = l_1 \dot{\varphi}_1 \quad v_{s2} = l_1 \dot{\varphi}_1 + l_2 \dot{\varphi}_2 \quad v_{s3} = l_1 \dot{\varphi}_1 + l_2 \dot{\varphi}_2 + l_3 \dot{\varphi}_3 \tag{D.10}$$

where l_i is the length of the i^{th} section. The term $\dot{\varphi}$ is the rotational velocity for each mass. The kinetic energy for each mass is given:

$$T_{s1} = \frac{1}{2} m_1 v_{s1}^2 \quad T_{s2} = \frac{1}{2} m_2 v_{s2}^2 \quad T_{s3} = \frac{1}{2} m_3 v_{s3}^2 \tag{D.11}$$

where m_i is the mass of the i^{th} section. Then the total kinetic energy for the structure is combined and shown as:

$$T_s = T_{s1} + T_{s2} + T_{s3} \tag{D.12}$$

The subscript 's' stands for 'structure'. The potential energy for each mass (V_i) and the whole structure (V_s) is shown as (the small angle assumption is applied):

$$\begin{aligned}
V_1 &= m_1 g l_1 \varphi_1 + \frac{1}{2} k_1 \varphi_1^2 \\
V_2 &= m_2 g (l_1 \varphi_1 + l_2 \varphi_2) + \frac{1}{2} k_2 (\varphi_2 - \varphi_1)^2 \\
V_3 &= m_3 g (l_1 \varphi_1 + l_2 \varphi_2 + l_3 \varphi_3) + \frac{1}{2} k_2 (\varphi_3 - \varphi_2)^2 \\
V_s &= V_1 + V_2 + V_3
\end{aligned} \tag{D.13}$$

The inviscid hydrodynamic forces acting on the cylinder could be expressed in terms of the kinetic energy of the fluid. Hence, the relative velocity of cylinder and fluid for each section is:

$$\begin{aligned} v_1 &= l_1 \dot{\varphi}_1 + v_c \varphi_1 \\ v_2 &= l_1 \dot{\varphi}_1 + l_2 \dot{\varphi}_2 + v_c \varphi_2 \\ v_3 &= l_1 \dot{\varphi}_1 + l_2 \dot{\varphi}_2 + l_3 \dot{\varphi}_3 + v_c \varphi_3 \end{aligned} \quad (D.14)$$

where v_c is the velocity of the incoming fluid, therefore, the kinetic energy of fluid is expressed as:

$$T_f = \frac{1}{2}(M_{n1} v_1^2 + M_{L1} v_c^2) + \frac{1}{2}(M_{n2} v_2^2 + M_{L2} v_c^2) + \frac{1}{2}(M_{n3} v_3^2 + M_{L3} v_c^2) \quad (D.15)$$

where M_{ni} is the virtual or added mass of the i^{th} section in the normal direction, and M_{Li} is the equivalent quantity for axial direction. The Lagrangian mathematical function L is equal to:

$$L = T_s + T_f - V_s \quad (D.16)$$

Then the following equations are deviated:

$$\begin{aligned} \frac{dL}{d\varphi_1} &= \frac{1}{2} M_{n1} (2l_1 \dot{\varphi}_1 v_c + 2v_c^2 \varphi_1) - k_1 \varphi_1 + k_2 (\varphi_2 - \varphi_1) - m_1 g l_1 - m_2 g l_1 - m_3 g l_1 \\ \frac{dL}{d\varphi_2} &= \frac{1}{2} M_{n2} (2l_1 \dot{\varphi}_1 v_c + 2l_2 \dot{\varphi}_2 v_c + 2v_c^2 \varphi_2) - k_2 (\varphi_2 - \varphi_1) + k_3 (\varphi_3 - \varphi_2) - m_2 g l_2 - m_3 g l_2 \\ \frac{dL}{d\varphi_3} &= \frac{1}{2} M_{n3} (2l_1 \dot{\varphi}_1 v_c + 2l_2 \dot{\varphi}_2 v_c + 2l_3 \dot{\varphi}_3 v_c + 2v_c^2 \varphi_3) - k_3 (\varphi_3 - \varphi_2) - m_3 g l_3 \end{aligned} \quad (D.17)$$

$$\begin{aligned} \frac{d}{dt} \left(\frac{dL}{d\dot{\varphi}_1} \right) &= l_1 [l_1 (M_{n1} + M_{n2} + M_{n3} + m_1 + m_2 + m_3) \ddot{\varphi}_1 + l_2 (M_{n2} + M_{n3} + m_2 + m_3) \ddot{\varphi}_2 \\ &\quad + l_3 (M_{n3} + m_3) \ddot{\varphi}_3 + v_c (M_{n1} \dot{\varphi}_1 + M_{n2} \dot{\varphi}_2 + M_{n3} \dot{\varphi}_3)] \\ \frac{d}{dt} \left(\frac{dL}{d\dot{\varphi}_2} \right) &= l_2 [l_1 (M_{n2} + M_{n3} + m_2 + m_3) \ddot{\varphi}_1 + l_2 (M_{n2} + M_{n3} + m_2 + m_3) \ddot{\varphi}_2 \\ &\quad + l_3 (M_{n3} + m_3) \ddot{\varphi}_3 + v_c (M_{n2} \dot{\varphi}_2 + M_{n3} \dot{\varphi}_3)] \\ \frac{d}{dt} \left(\frac{dL}{d\dot{\varphi}_3} \right) &= l_3 [l_1 (M_{n3} + m_3) \ddot{\varphi}_1 + l_2 (M_{n3} + m_3) \ddot{\varphi}_2 + l_3 (M_{n3} + m_3) \ddot{\varphi}_3 + M_{n3} \dot{\varphi}_3 v_c] \end{aligned} \quad (D.18)$$

When we evenly separate the whole structure to three sections, the follow parameters satisfies the relationship which is shown below:

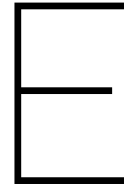
$$m_1 = m_2 = m_3 = m \quad l_1 = l_2 = l_3 = l \quad k_1 = k_2 = k_3 = k \quad M_{n1} = M_{n2} = M_{n3} = M_n \quad (D.19)$$

The equations of motion for the second model are written as:

$$\begin{aligned} EOM_1: \frac{d}{dt} \left(\frac{dL}{d\dot{\varphi}_1} \right) - \frac{dL}{d\varphi_1} &= 3l^2 (M_n + m) \ddot{\varphi}_1 + 2l^2 (M_n + m) \ddot{\varphi}_2 + l^2 (M_n + m) \ddot{\varphi}_3 + M_n \dot{\varphi}_2 v_c l \\ &\quad + M_n \dot{\varphi}_3 v_c l + (-M_n v_c^2 + 2k) \varphi_1 - k \varphi_2 + 3glm = Q_1 \\ EOM_2: \frac{d}{dt} \left(\frac{dL}{d\dot{\varphi}_2} \right) - \frac{dL}{d\varphi_2} &= 2l^2 (M_n + m) \ddot{\varphi}_1 + 2l^2 (M_n + m) \ddot{\varphi}_2 + l^2 (M_n + m) \ddot{\varphi}_3 - M_n \dot{\varphi}_1 v_c l \\ &\quad + M_n \dot{\varphi}_3 v_c l + (-M_n v_c^2 + 2k) \varphi_2 - k(\varphi_1 + \varphi_3) + 2glm = Q_2 \\ EOM_3: \frac{d}{dt} \left(\frac{dL}{d\dot{\varphi}_3} \right) - \frac{dL}{d\varphi_3} &= l^2 (M_n + m) \ddot{\varphi}_1 + l^2 (M_n + m) \ddot{\varphi}_2 + l^2 (M_n + m) \ddot{\varphi}_3 - M_n \dot{\varphi}_1 v_c l \\ &\quad - M_n \dot{\varphi}_2 v_c l + (-M_n v_c^2 + k) \varphi_3 - k \varphi_2 + glm = Q_3 \end{aligned} \quad (D.20)$$

where Q_1, Q_2, Q_3 are external moments that are expressed in Section 6.2. Again, after added viscous damping terms into equations, the final equations are derived.

$$\begin{aligned}
EOM_1 : & 3l^2(M_n + m)\ddot{\varphi}_1 + 2l^2(M_n + m)\ddot{\varphi}_2 + l^2(M_n + m)\ddot{\varphi}_3 + M_n\dot{\varphi}_2 v_c l + M_n\dot{\varphi}_3 v_c l \\
& + 2c\dot{\varphi}_1 - c\dot{\varphi}_2 + (-M_n v_c^2 + 2k)\varphi_1 - k\varphi_2 + 3glm = Q_1 \\
EOM_2 : & 2l^2(M_n + m)\ddot{\varphi}_1 + 2l^2(M_n + m)\ddot{\varphi}_2 + l^2(M_n + m)\ddot{\varphi}_3 - M_n\dot{\varphi}_1 v_c l + M_n\dot{\varphi}_3 v_c l \\
& + 2c\dot{\varphi}_2 - c\dot{\varphi}_1 - c\dot{\varphi}_3 + (-M_n v_c^2 + 2k)\varphi_2 - k(\varphi_1 + \varphi_3) + 2glm = Q_2 \\
EOM_3 : & l^2(M_n + m)\ddot{\varphi}_1 + l^2(M_n + m)\ddot{\varphi}_2 + l^2(M_n + m)\ddot{\varphi}_3 - M_n\dot{\varphi}_1 v_c l - M_n\dot{\varphi}_2 v_c l \\
& + c\dot{\varphi}_3 - c\dot{\varphi}_2 + (-M_n v_c^2 + k)\varphi_3 - k\varphi_2 + glm = Q_3
\end{aligned} \tag{D.21}$$



Vibration graphs for all sections

In Section 6.4.2, we analyzed the movement of the last sections of the structure. Sections before that have similar discipline as the last section. Here some figures show the displacements when velocity is 0.57ms^{-1} , 0.7ms^{-1} , 0.77ms^{-1} , 0.8ms^{-1} , 0.82ms^{-1} , 1.5ms^{-1} , 2ms^{-1} and 2.5ms^{-1} . Similarly, case I: $f = 1$ (i.e. $F_{nc} = 0$, blue curves) and case II: $f = 0$ (i.e. F_{nc} is maximum, orange curves).

- Velocity is equal to 0.57ms^{-1} , and both cases are vibrating until reach a steady-state position. Maximum displacements and their differences for each section are small.

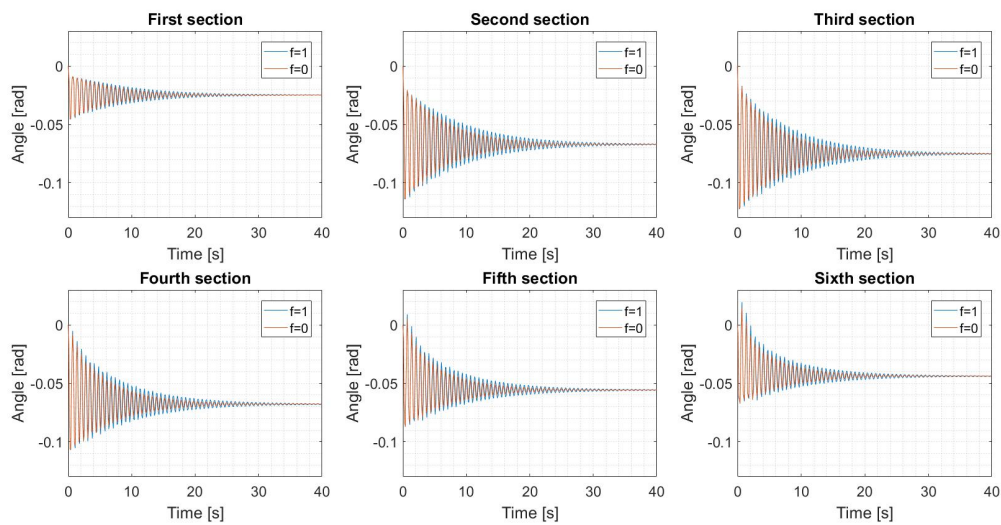


Figure E.1: Vibration of first six sections when $v_c = 0.57\text{ms}^{-1}$

- Velocity is equal to 0.7ms^{-1} , similar stable movement as $v_c = 0.57\text{ms}^{-1}$ situation.

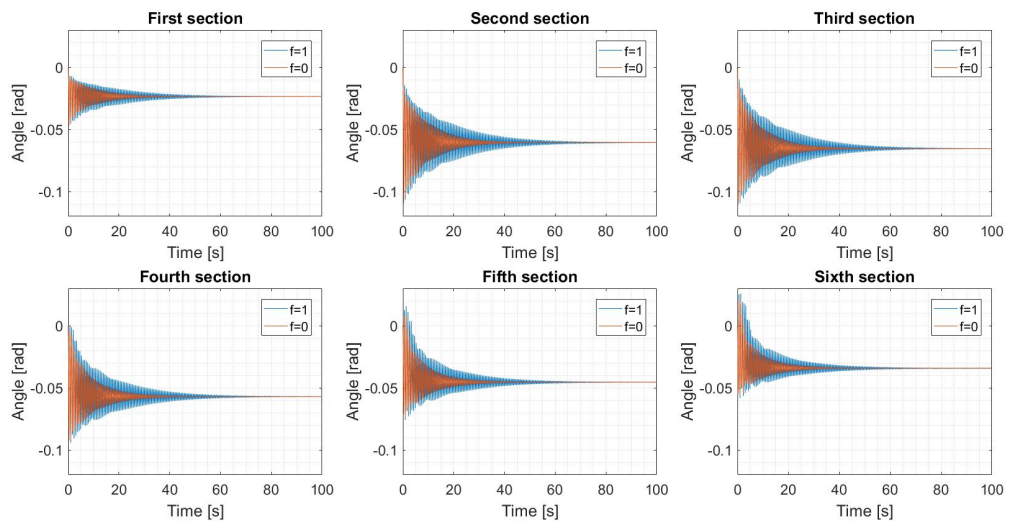


Figure E.2: Vibration of first six sections when $v_c = 0.70\text{ms}^{-1}$

- Velocity is equal to 0.77ms^{-1} . Case I has already converted to flutter instability but case II not. Correspondingly, maximum displacements and their differences for each section are small.

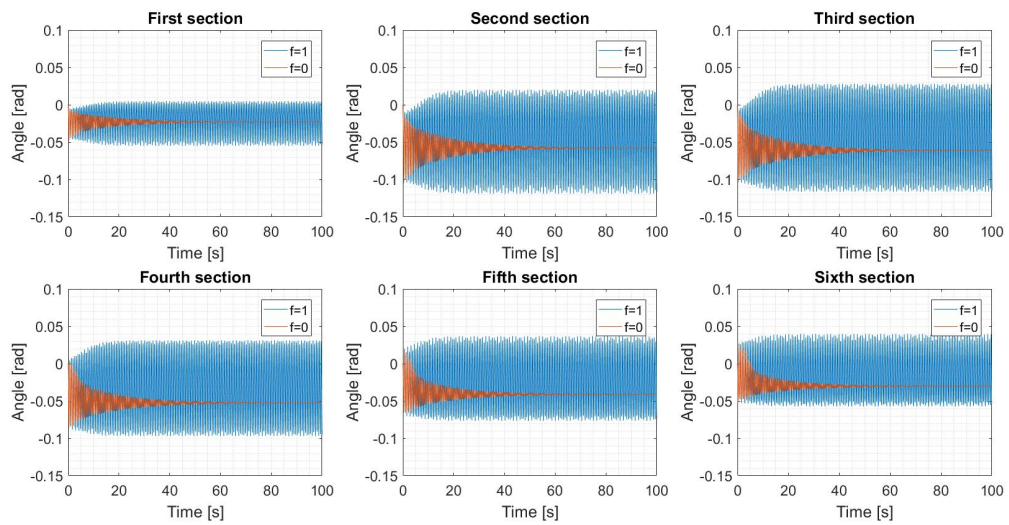


Figure E.3: Vibration of first six sections when $v_c = 0.77\text{ms}^{-1}$

- Velocity is equal to $0.8ms^{-1}$, similar stable movement as $v_c = 0.77ms^{-1}$ situation.

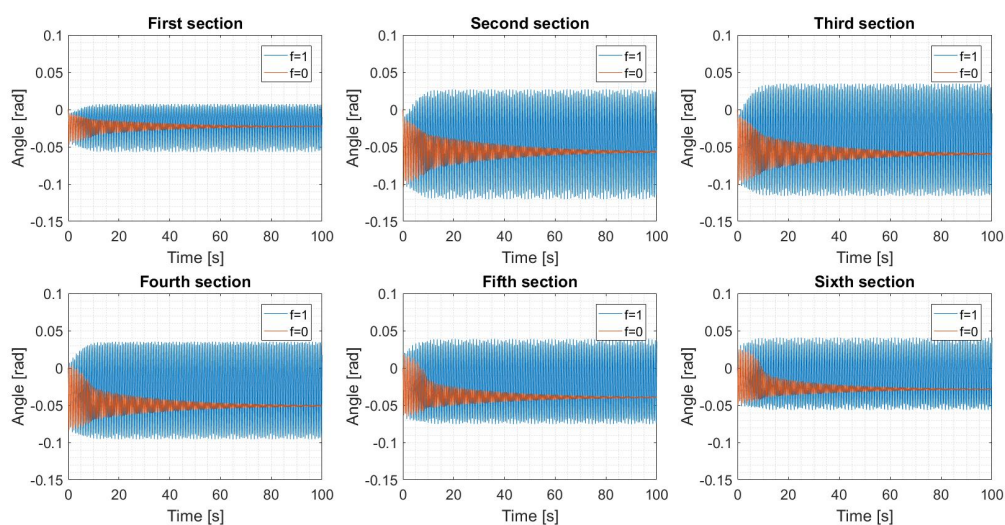


Figure E.4: Vibration of first six sections when $v_c = 0.80ms^{-1}$

- Velocity is equal to $0.82ms^{-1}$. Both cases convert to flutter instability at this time.

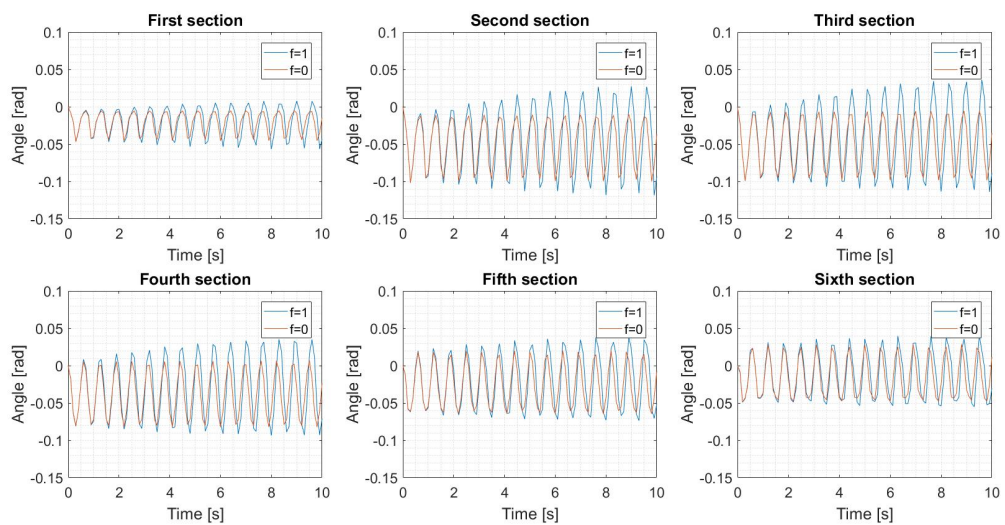


Figure E.5: Vibration of first six sections when $v_c = 0.82ms^{-1}$

- Velocity is equal to $1.5ms^{-1}$. With the velocity increasing, the maximum displacements are also increasing gradually.

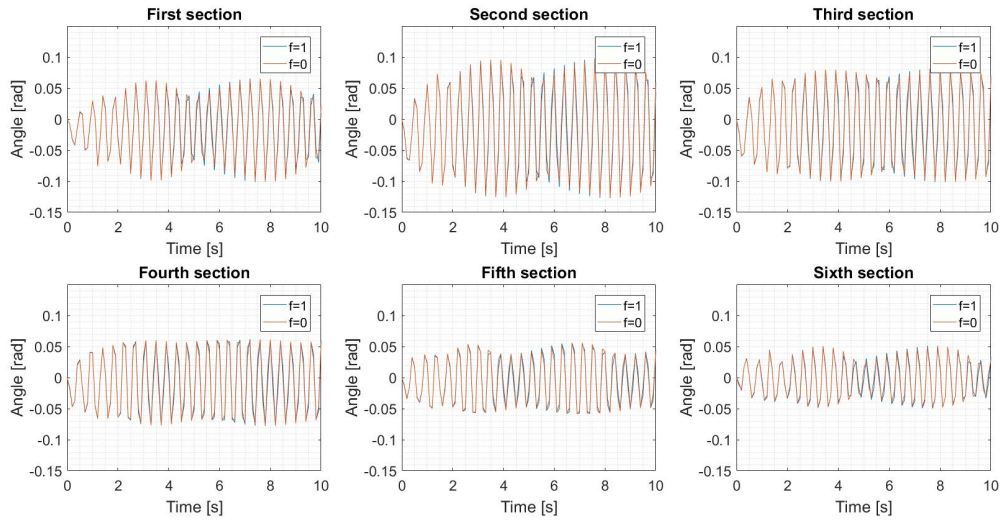


Figure E.6: Vibration of first six sections when $v_c = 1.50ms^{-1}$

- Velocity is equal to $2.0ms^{-1}$.

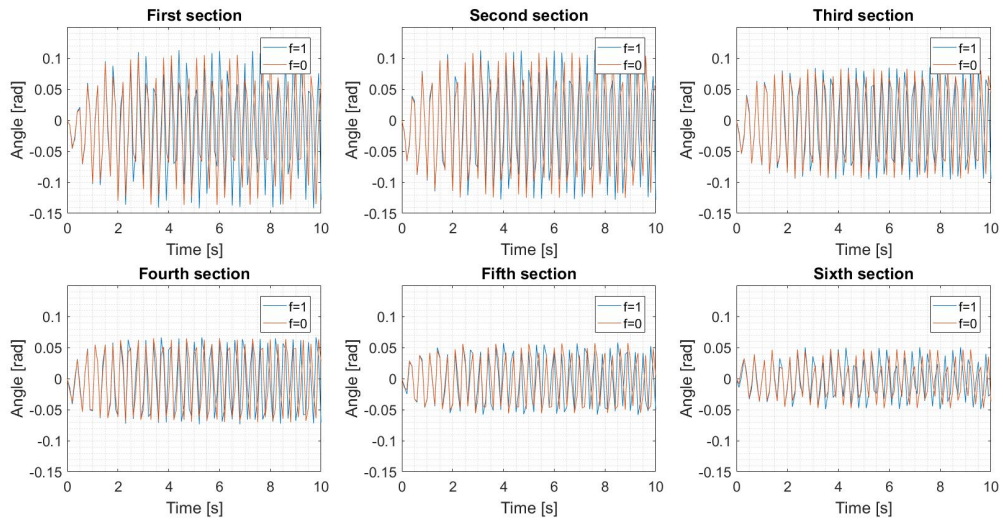


Figure E.7: Vibration of first six sections when $v_c = 2.00ms^{-1}$

- Velocity is equal to 2.5ms^{-1} .

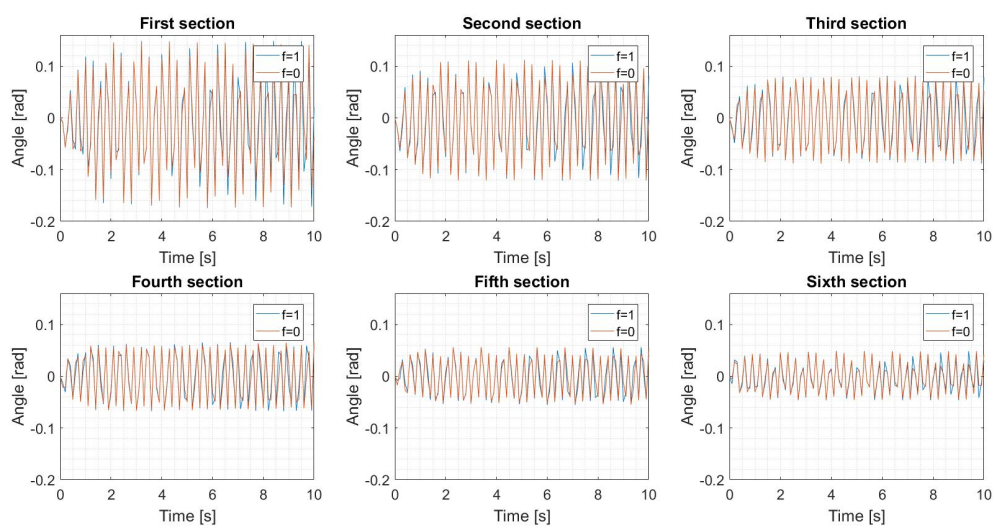
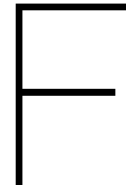


Figure E.8: Vibration of first six sections when $v_c = 2.50\text{ms}^{-1}$



User guide and the script of models

In this appendix, recommendations and explanations for practical use of the models are found. Specifically, MATLAB script for each model is shown here in detail for the practical use of the company. In the scripts, the requirement of the inputs, and other explanations are written after ‘%’ in green.

- The first model (7 sections) in this thesis is used for a swing motion which is suitable as the velocity is smaller than 0.57ms^{-1} . The first model is not generated to n sections model cause the ultimate moment and loads are not expected in this period. This model requires a specific velocity input and predicts the motions of the structure. The data in the scripts that is shown below is the input that based on the surrogate information. For the theoretical part of this, please consult Chapter 5. The main part of the script is shown below:

```
1 % This script is a numerical model that based on ode45 with function
2 % called 'odefun_firstmodel_7sections'.
3 %
4 % The introduction of the theory such as simplification method, the derivation
5 % process and some simulation results are shown in Chapter 5. It calculates
6 % the displacements for the aimed structure for each simulation second.
7 %
8 % This script calculates the displacements, velocities, and accelerations for
9 % each time spans and they will be used again as an input for the computation
10 % of the next time interval.
11 %
12 % This script is used in the condition that the model is influenced by current
13 % and the whole model are separated into 7 sections (1 section for base part,
14 % 6 sections for other parts) which are connected by rotational springs and
15 % damping dash pot.
16 %
17 % For each section, the length, the mass and the damping constant is same.
18 % Rotational spring constant is different between base part and other parts.
19
20 clc;
21 clear;
22
23 %% Input basic parameters
24
25 P.l      = 0.28/7;           % [m] Length of each section
26 P.m      = 17.1/1000/7;     % [kg] mass of each section
27 P.kts    = 0.05804;         % [Nm] Rotational spring constant of base part
28 P.ktl    = 0.0152;         % [Nm] Rotational spring constant of other parts
29 P.minwater = 2/1000/7;     % [kg] Mass minus buoyancy
30 P.ct     = 0.013;          % [Nms] Damping constant of each section
31 P.d      = 0.01013;        % [m] Diameter of the base part
32 P.w      = 0.046;          % [m] Width of other parts
33 P.F_amp_s = 0.5*1000*P.d*P.l*1.98;
34 % External force constant for base part F_amp_s=1/2*rho*d*l*cd90; water density
35 % rho=1000kg/m^3; drag coefficient constant cd90=1.98
36 P.F_amp_l = 0.5*1000*P.w*P.l*1.98;
```

```

37 % External force constant for other parts F_amp_l=1/2*rho*w*l*cd90
38 P.g      = 9.81;          % [m/s^2] Gravity acceleration
39 P.v      = 0.57;          % [m/s] current velocity
40 % Time span
41 tspan    = 0:0.1:10;
42
43 %% Model initial conditions, M K K1 C matrix and implement odefunction
44 % Iintial conditions: 7 sections 14 initial conditions (initial displacements and
45 % velocities). Tested in the experiment when the current velocity is 0
46 init_disp1 = (0.064);
47 init_velo1  = (0);
48 init_disp2 = (0.100);
49 init_velo2  = (0);
50 init_disp3 = (0.351);
51 init_velo3  = (0);
52 init_disp4 = (0.397);
53 init_velo4  = (0);
54 init_disp5 = (0.477);
55 init_velo5  = (0);
56 init_disp6 = (0.504);
57 init_velo6  = (0);
58 init_disp7 = (0.631);
59 init_velo7  = (0);
60
61 % Initial conditions matrix
62 q_0 = [init_disp1;init_disp2;init_disp3;init_disp4;init_disp5;init_disp6;init_disp7;
63        init_velo1;init_velo2;init_velo3;init_velo4;init_velo5;init_velo6;init_velo7];
64
65 % M matrix
66 P.M=P.m*P.l^2*[7 6 5 4 3 2 1;
67                6 6 5 4 3 2 1;
68                5 5 5 4 3 2 1;
69                4 4 4 4 3 2 1;
70                3 3 3 3 3 2 1;
71                2 2 2 2 2 2 1;
72                1 1 1 1 1 1 1];
73
74 % Damping matrix
75 P.C=P.ct*[2 -1 0 0 0 0 0;
76           -1 2 -1 0 0 0 0;
77           0 -1 2 -1 0 0 0;
78           0 0 -1 2 -1 0 0;
79           0 0 0 -1 2 -1 0;
80           0 0 0 0 -1 2 -1;
81           0 0 0 0 0 -1 1];
82
83 % Spring constant matrix (stiffness)
84 P.K=[P.kts+P.ktl -P.ktl 0 0 0 0 0;
85      -P.ktl 2*P.ktl -P.ktl 0 0 0 0;
86      0 -P.ktl 2*P.ktl -P.ktl 0 0 0;
87      0 0 -P.ktl 2*P.ktl -P.ktl 0 0;
88      0 0 0 -P.ktl 2*P.ktl -P.ktl 0;
89      0 0 0 0 -P.ktl 2*P.ktl -P.ktl;
90      0 0 0 0 0 -P.ktl P.ktl];
91
92 % Gravity matrix
93 P.K1=P.minwater*P.g*P.l*[7 0 0 0 0 0 0;
94                          0 6 0 0 0 0 0;
95                          0 0 5 0 0 0 0;
96                          0 0 0 4 0 0 0;
97                          0 0 0 0 3 0 0;
98                          0 0 0 0 0 2 0;
99                          0 0 0 0 0 0 1];
100
101 % Internal moment matrix:
102 % (Due to the initial shape of the surrogate, it is not perfectly straight and
103 % contains initial moment. Therefore a initial moment matrix is implemented
104 % here to vanish this internal moment influence.)
105 P.K0=[-P.kts P.ktl 0 0 0 0 0;
106       0 -P.ktl P.ktl 0 0 0 0;
107       0 0 -P.ktl P.ktl 0 0 0;

```

```

108     0 0 0 -P.ktl P.ktl 0 0;
109     0 0 0 0 -P.ktl P.ktl 0;
110     0 0 0 0 0 -P.ktl P.ktl
111     0 0 0 0 0 0 -P.ktl];
112
113 % Initial angle matrix which is produced by internal moment
114 P.initialangle=[0.3;0;0;0;0;0;0];
115
116 % Call ode function: odefun_firstmodel_7sections
117 [T,Y] = ode45(@(t,q_n)odefun_firstmodel_7sections(t,q_n,P),tspan,q_0);

```

The further analysis for the output of the model such as, the movie of the motion for the simulation period, comparison between the model results and the experiment result (steady-state position, force, etc.), are not listed here. For this part please check the original scripts. The ode function that used in the main script (*odefun_firstmodel_7sections*) is shown below:

```

1 % Ode function that used for the first model
2
3 function [q_n_dot] = odefun_firstmodel_7sections(t, q_n, P)
4
5 % Force arm for the vertical force
6 P.FLarm (1) = P.l*sin(q_n(1)); P.FDarm (1) = P.l*cos(q_n(1))+0.02;
7 for i = 2:7
8     P.FLarm (i) = P.l*sin(q_n(i)) + P.FLarm(i-1);
9     P.FDarm (i) = P.l*cos(q_n(i)) + P.FDarm(i-1);
10 end
11
12 % Form drag for each section
13 P.F = [P.F_amp_s*(P.v)^2; P.F_amp_l*(P.v)^2;
14        P.F_amp_l*(P.v)^2; P.F_amp_l*(P.v)^2;
15        P.F_amp_l*(P.v)^2; P.F_amp_l*(P.v)^2;
16        P.F_amp_l*(P.v)^2];
17
18 % Skin friction for each section
19 P.Ff = [P.F_amp_s/1.98*0.037*(P.v).^2; P.F_amp_l/1.98*0.037*(P.v).^2;
20        P.F_amp_l/1.98*0.037*(P.v).^2; P.F_amp_l/1.98*0.037*(P.v).^2;
21        P.F_amp_l/1.98*0.037*(P.v).^2; P.F_amp_l/1.98*0.037*(P.v).^2;
22        P.F_amp_l/1.98*0.037*(P.v).^2];
23
24 % For the sign of terms
25 for j = 1:7
26     if q_n(j,1) > 1.5708
27         con(j) = -1;
28     else
29         con(j) = 1;
30     end
31 end
32
33 end
34 q_n_dot = [q_n(8:14,1);
35           P.M(...
36           - P.K * q_n(1:7,1) ...
37           - P.K1 * sin(q_n(1:7,1)) ...
38           - P.C * q_n(8:14,1) ...
39           - P.K0 * P.initialangle ...
40           + abs((P.F.*(cos(q_n(1:7,1))).^3 + P.Ff.*(sin(q_n(1:7,1)).^3)) .* P.FDarm') ...
41           + con'.*abs( P.F.*(cos(q_n(1:7,1))).^3.*tan(q_n(1:7,1)) ...
42           - P.Ff.*(sin(q_n(1:7,1))).^3./tan(q_n(1:7,1)) .* P.FLarm') ...
43           )];
44
45 end

```

- The second model (n sections) in this thesis is used for a potential flutter motion which is suitable for larger velocities. This model also requires a specific velocity input and predicts the motions of the structure. The data in the scripts that is shown below is the input based on the information of Wakame in growing Phase V. For the theoretical part of this, please consult Chapter 6. The main part of the script is shown below:

```

1 % This script is a numerical model that based on ode45 with function called
2 % 'odefun_secondmodel_nsections_f0 and odefun_secondmodel_nsections_f1'.
3 %
4 % The introduction of the theory such as simplification method, the derivation
5 % process and some simulation results are shown in Chapter 6. It calculates
6 % the displacements for the aimed structure for each simulation second.
7 %
8 % This script calculates the displacements, velocities, and accelerations for
9 % each time spans and they will be used again as an input for the computation
10 % of the next time interval.
11 %
12 % This script is used in the condition that the model is influenced by current
13 % and the whole model are separated into n sections (sn sections for base part,
14 % ln sections for other parts) which are connected by rotational springs and
15 % damping dash pot.
16 %
17 % The base part is recommended to be used as similar length of the other parts'
18 % section. The other parts is advised to be divided for sections which as 5-6cm
19 % cause of the influence of the Fnc.
20 %
21 % For each section in the base part and other parts separately, the length
22 % is the same.
23 % For each section of the model, the mass is the same.
24 %
25 % The added mass is assumed as 80% of the solid mass.
26 %
27 % Rotational spring constant and damping constant (70% of critical damping) is
28 % different between sections base part and other parts.
29 %
30 %% The inputs in this script is:
31 % The length of the base part (base_length) of the kelp and the total length
32 % (total_length) of the plant.
33 %
34 % How many sections are preferred to be divided for the base part (P.sn) and other
35 % parts (P.ln) respectively.
36 %
37 % The flexural rigidity for base part (Js) and other parts (Jl).
38 %
39 % The diameter of the base part (P.d) and the width of the other parts (P.w).
40 %
41 % The mass of the plant (P.m). The density of the plant.
42 %
43 clc;
44 clear;
45 %% Basic parameters input
46
47 %input the base length and the total length of the body.
48 base_length = 0.55; % [m] Length of base part
49 total_length = 1.95; % [m] Total length
50
51 %input the separation method
52 P.sn = 10; P.ln = 24; % P.sn sections for base part P.ln sections for other parts
53 P.n = P.ln + P.sn; % Sumation of sections for the whole blade
54 P.ls = base_length / P.sn;
55 % [m] Length for each section of base part
56 P.ll = (total_length - base_length) / P.ln;
57 % [m] Length for each section of other parts
58
59 %input flexural rigidity
60 Js = 34.47e-4; % [Nm^2] Flexural rigidity of base part
61 Jl = 3.10e-4; % [Nm^2] Flexural rigidity of other parts
62 P.kts = Js / P.ls;
63 % [Nm] Rotational spring constant of each section of the base part
64 P.ktl = Jl / P.ll;
65 % [Nm] Rotational spring constant of each section of the other parts
66
67 %input the sizes
68 P.w = 0.299; % [m] Width of the other parts
69 P.d = 0.01013; % [m] Diameter of the base part
70

```

```

71 %input the mass and density
72 P.m      = 610/1000/P.n;          % [kg] mass of each section
73 P.Mn     = 0.8*P.m;              % [kg] Added mass
74 P.rho    = 1076.2;              % [kg/m^3] Density
75 P.minwater = (P.rho-1000)*P.m/P.rho; % [kg] Mass minus buoyancy
76
77
78 P.cts    = 0.7*2*sqrt(P.kts*P.m*P.ls^2);
79 % [Nms] Damping for the base part.
80 % 70% of critical damping P.cts= 0.7*2*sqrt(P.kts*P.m*P.ls^2)
81 P.ctl    = 0.7*2*sqrt(P.ktl*P.m*P.ll^2);
82 % [Nms] Damping for other parts.
83 % 70% of critical damping P.cts= 0.7*2*sqrt(P.ktl*P.m*P.ll^2)
84
85
86 P.F_amp_s = 0.5*1000*P.d*P.ls*1.98;
87 % External force constant for base part F_amp_s=1/2*rho*d*ls*cd90;
88 % water density rho=1000kg/m^3; drag coefficient constant cd90=1.98
89 P.F_amp_l = 0.5*1000*P.w*P.ll*1.98;
90 % External force constant for other parts F_amp_l=1/2*rho*w*ll*cd90
91
92
93 P.g      = 9.81;                  % [m/s^2] Gravity acceleration
94 P.f0     = 0;   P.fl=1;          % Parameter f in Fnc formulation
95 P.v      = 1;                    % [m/s] current velocity
96 % Time span
97 tspan    =0:0.1:100;
98
99 %% Matrix J
100 P.J=zeros(P.n);
101 for i=1:P.n
102 P.J(1:i,1:i)=P.J(1:i,1:i)+1;
103 end
104 P.J=P.J*(P.m+P.Mn);
105
106 V=zeros(P.n,1);
107 for j=1:P.sn
108 V(j)=V(j)+P.ls;
109 end
110 for j=P.sn+1:P.n
111 V(j)=V(j)+P.ll;
112 end
113
114 for i=1:P.n
115     for j=1:P.n
116         P.J(i,j)=P.J(i,j)*V(i)*V(j);
117     end
118 end
119
120 %% initial condition matrix q_0, gravity matrix con and hydrodynamic force ...
121     stiffness matrix Kf
122 q_0 = [];P.con=[];P.Kf=zeros(P.n,P.n);
123 for i=1:P.n
124 q_0(i,1)=0;
125 q_0(i+P.n,1)=0;
126
127 P.con(i,1)=P.minwater*P.g*V(i).*(P.n-i+1);
128 P.Kf(i,i)=-P.Mn.*P.v^2;
129 end
130 %% Stiffness matrix Ks, viscous damping matrix Cs
131 K1=P.kts*[1 -1;-1 1];K2=P.ktl*[1 -1;-1 1];P.Ks=zeros(P.n,P.n);
132 C1=P.cts*[1 -1;-1 1];C2=P.ctl*[1 -1;-1 1];P.Cs=zeros(P.n,P.n);
133 for i=1:P.sn-1
134 P.Ks(i:i+1,i:i+1)=P.Ks(i:i+1,i:i+1)+K1;
135 P.Cs(i:i+1,i:i+1)=P.Cs(i:i+1,i:i+1)+C1;
136 end
137 for i=P.sn:P.n-1
138 P.Ks(i:i+1,i:i+1)=P.Ks(i:i+1,i:i+1)+K2;
139 P.Cs(i:i+1,i:i+1)=P.Cs(i:i+1,i:i+1)+C2;
140 end

```

```

141 if P.sn>1
142 P.Ks(1,1)=2*P.kts;P.Cs(1,1)=2*P.cts;
143 else
144 P.Ks(1,1)=P.kts+P.ktl;P.Cs(1,1)=P.cts+P.ctl;
145 end
146 %% Hydrodynamic force damping matrix Cf
147
148 P.Cf=[];
149 for i=1:P.n
150     for j=1:P.n
151         if i>j
152             P.Cf(i,j)=-1;
153         elseif i<j
154             P.Cf(i,j)=1;
155         else
156             P.Cf(i,j)=0;
157         end
158     end
159 end
160 P.Cf=P.Cf*P.Mn*P.v*P.ll;
161 for i=1:P.sn
162     P.Cf(i,i:end)=P.Cf(i,i:end)/P.ll*P.ls;
163     P.Cf(i:end,i)=P.Cf(i:end,i)/P.ll*P.ls;
164 end
165
166 %% Call ode function odefun_secondmodel_nsections_f0 and ...
167     odefun_secondmodel_nsections_f1
167 [T,Y] = ode45(@(t,q_n)odefun_secondmodel_nsections_f0(t,q_n,P),tspan,q_0);
168 [Tf1,Yf1] = ode45(@(t,q_n)odefun_secondmodel_nsections_f1(t,q_n,P),tspan,q_0);

```

The analysis part of this model is not shown here. It includes the codes that drawing a graph for comparing the results with or without the inviscid force F_{nc} that is aimed at studying its influence. Please check the original files for the detail. The ode function called *odefun_secondmodel_nsections_f0* that used in this main script is shown below. For the function *odefun_secondmodel_nsections_f1*, the only thing need to be changed is that changing *P.f0* that located in line 31 to *P.f1*.

```

1  % Ode function that used for the second model n sections f=0
2
3  function [q_n_dot] = odefun_secondmodel_nsections_f0(t, q_n, P)
4  % Form drag and frictional drag for each section
5  P.F=[];P.Ff=[];
6  for i=1:P.sn
7      P.F(i,1)=P.F_amp_s*(P.v).^2;P.Ff(i,1)=P.F_amp_s/1.98*0.037*(P.v).^2;
8  end
9  for i=P.sn+1:P.n
10     P.F(i,1)=P.F_amp_l*(P.v).^2;P.Ff(i,1)=P.F_amp_l/1.98*0.037*(P.v).^2;
11 end
12
13 % Tip velocity for each section
14 P.Vtip(1)=P.ls*q_n(1+P.n);
15 if P.sn>1
16     for i=2:P.sn
17         P.Vtip(i)=P.Vtip(i-1)+P.ls*q_n(i+P.n);
18     end
19     for i=P.sn+1:P.n
20         P.Vtip(i)= P.Vtip(i-1)+P.ll*q_n(i+P.n);
21     end
22
23 else
24     for i=2:P.n
25         P.Vtip(i)=P.Vtip(i-1)+P.ll*q_n(i+P.n);
26     end
27 end
28
29 % Force Fnc
30 P.Fnc = zeros(P.n,1);
31 P.Fnc(P.n,1)=(1-P.f0)*P.Mn*P.v;
32

```

```

33 % Force arm for skin frictional drag (armforA)
34 R(1)=0;
35 if P.sn>1
36     for i=2:P.sn+1
37         R(i)=R(i-1)-q_n(i-1)*P.ls;
38     end
39     for i=P.sn+2:P.n
40         R(i)=R(i-1)-q_n(i-1)*P.ll;
41     end
42 else
43     R(2)=-q_n(1)*P.ls;
44     for i=3:P.n
45         R(i)=R(i-1)-q_n(i-1)*P.ll;
46     end
47 end
48 armforA=zeros(P.n,1);
49
50 if P.sn>1
51     for i=2:P.sn
52         armforA(i)=R(i)+q_n(i)*(i-1)*P.ls;
53     end
54     for i=P.sn+1:P.n
55         armforA(i)=R(i)+q_n(i)*(P.sn*P.ls+(i-1-P.sn)*P.ll);
56     end
57 else
58     for i=2:P.n
59         armforA(i)=R(i)+q_n(i)*(P.ls+(i-2)*P.ll);
60     end
61 end
62
63 % For the sign of terms
64 for j = 1:P.n
65     if q_n(j,1) > 0
66         con(j)=1;
67     else
68         con(j)=-1;
69     end
70 end
71
72 % Force arm of form drag and Fnc
73 P.larm(1)=P.ls;
74 if P.sn>1
75     for i=2:P.sn
76         P.larm(i)=P.larm(i-1)+P.ls;
77     end
78     for i=P.sn+1:P.n
79         P.larm(i)=P.larm(i-1)+P.ll;
80     end
81 else
82     for i=2:P.n
83         P.larm(i)=P.larm(i-1)+P.ll;
84     end
85 end
86
87 q_n_dot = [q_n(P.n+1:2*P.n,1);
88     P.J\(...
89     - P.Ks * q_n(1:P.n,1)-P.Kf * q_n(1:P.n,1)...
90     - P.con...
91     - P.Cf * q_n(P.n+1:2*P.n,1)...
92     - P.Cs* q_n(P.n+1:2*P.n,1)...
93     + P.Ff.*armforA -con' .*P.F.*q_n(1:P.n,1).^2.*P.larm'...
94     -P.Fnc.*(P.Vtip'+P.v.*q_n(1:P.n,1)).*P.larm');];
95
96 end

```

- The ultimate moment and loads are predicted based on the second model as velocity ranging from 0 to 1.25ms^{-1} . The script shown below is aimed at calculating the maximum and minimum moments and forces on the plant for each velocity interval. The inputs in the scripts below based on the data of the Wakame plant that in Phase IV and the velocity interval is set as 0.01ms^{-1} . The ode function that used

in this part is explained and listed above. In the end of the script, the curves are drawn for illustrating the trending of the results.

```

1 % This script is a numerical model that based on ode45 with function
2 % called odefun_secondmodel_nsections_f0.
3 %
4 % The introduction of the theory such as simplification method, the derivation
5 % process and some simulation results are shown in Chapter 6 and 7. It
6 % calculates the displacements for the aimed structure for each simulation second.
7 %
8 % This script calculates the maximum moment horizontal and vertical force on
9 % the model for a series of velocities and plot it.
10 %
11 % This script is used in the condition that the model is influenced by current
12 % and the whole model are separated into n sections (sn sections for base part,
13 % ln sections for other parts) which are connected by rotational springs and
14 % damping dash pot.
15 %
16 % The base part is recommended to be used as similar length of the other parts'
17 % section. The other parts is advised to be divided for sections which as 5-6cm
18 % cause of the influence of the Fnc.
19 %
20 % For each section for base part or other parts separately, the length
21 % is the same.
22 % For each section of the model, the mass is the same.
23 % The added mass is assumed as 80% of the solid mass.
24 % Rotational spring constant and damping constant (70% of critical damping) is
25 % different between base part and other parts.
26 %
27 % The simulation current velocity range is form 0 to 2.5m/s.
28 % This simulation is based on f=0.
29
30 %% The inputs in this script is:
31 % The length of the base part (base_length) of the kelp and the total length
32 % (total_length) of the plant.
33 %
34 % How many sections are preferred to be divided for the base part (P.sn) and other
35 % parts (P.ln) respectively.
36 %
37 % The flexural rigidity for base part (Js) and other parts (Jl).
38 %
39 % The diameter of the base part (P.d) and the width of the other parts (P.w).
40 %
41 % The mass of the plant (P.m). The density of the plant.
42 %
43 clc;
44 clear;
45 %% Basic parameters input
46
47 %input the base length and the total length of the body.
48 base_length = 0.42; % [m] Lenght of base part
49 total_length= 2; % [m] Total length
50
51 %input the separation method
52 P.sn =8; P.ln= 28; % P.sn sections for base part P.ln sections for other parts
53 P.n=P.ln+P.sn; % Sumation of sections for the whole blade
54 P.ls = base_length/P.sn;
55 % [m] Length for each section of base part
56 P.ll = (total_length-base_length)/P.ln;
57 % [m] Length for each section of other parts
58
59 %input Flexural rigidity
60 Js=32.83e-4; % [Nm^2] Flexural rigidity of base part
61 Jl=2.95e-4; % [Nm^2] Flexural rigidity of other parts
62 P.kts = Js/P.ls;
63 % [Nm] Rotational spring constant of each section of the base part
64 P.ktl = Jl/P.ll;
65 % [Nm] Rotational spring constant of each section of the other parts
66

```



```

67 %input the sizes
68 P.w=0.3067; % [m] width of the other parts
69 P.d=0.01013; % [m] Diameter of the base part
70
71 %input the mass and density
72 P.m = 395/1000/P.n; % [kg] Mass of each section
73 P.Mn = 0.8*P.m; % [kg] Added mass
74 P.rho = 1076.2; % [kg/m^3] Density
75 P.minwater = (P.rho-1000)*P.m/P.rho; % [kg] Mass minus buoyancy
76
77
78 P.cts = 0.7*2*sqrt(P.kts*P.m*P.ls^2);
79 % [Nms] Damping for the base part.
80 % 70% of critical damping P.cts= 0.7*2*sqrt(P.kts*P.m*P.ls^2)
81 P.ct1 = 0.7*2*sqrt(P.ktl*P.m*P.ll^2);
82 % [Nms] Damping for other parts.
83 % 70% of critical damping P.cts= 0.7*2*sqrt(P.ktl*P.m*P.ll^2);
84
85
86 P.F_amp_s = 0.5*1000*P.d*P.ls*1.98;
87 % External force constant for base part F_amp_s=1/2*rho*d*ls*cd90
88 % water density rho=1000kg/m^3; drag coefficient constant cd90=1.98
89 P.F_amp_l = 0.5*1000*P.w*P.ll*1.98;
90 % External force constant for other parts F_amp_l=1/2*rho*w*ll*cd90
91
92
93 P.g = 9.81; % [m/s^2] Gravity acceleration
94 P.f0 = 0; P.f1=1; % Parameter f in Fnc fomulation
95 % Time span
96 tspan =0:0.1:100;
97
98 %% loop for velocity from 0 to 2.5m/s the velocity interval could be set in Δ
99 vbase(1)=0;
100 Δ=0.01;
101 for n=1:1:(1.25-vbase(1))/Δ
102 P.v =vbase(n);
103 %% Matrix J
104 P.J=zeros(P.n);
105 for i=1:P.n
106 P.J(1:i,1:i)=P.J(1:i,1:i)+1;
107 end
108 P.J=P.J*(P.m+P.Mn);
109
110 V=zeros(P.n,1);
111 for j=1:P.sn
112 V(j)=V(j)+P.ls;
113 end
114 for j=P.sn+1:P.n
115 V(j)=V(j)+P.ll;
116 end
117
118 for i=1:P.n
119 for j=1:P.n
120 P.J(i,j)=P.J(i,j)*V(i)*V(j);
121 end
122 end
123
124 %% Initial condition matrix q_0, gravity matrix con and hydrodynamic force ...
125 % stiffness matrix Kf
126 q_0 =[];P.con=[];P.Kf=zeros(P.n,P.n);
127 for i=1:P.n
128 q_0(i,1)=0;
129 q_0(i+P.n,1)=0;
130
131 P.con(i,1)=P.minwater*P.g*V(i).*(P.n-i+1);
132 P.Kf(i,i)=-P.Mn.*P.v^2;
133 end
134
135 %% Stiffness matrix Ks, viscous damping matrix Cs
136 K1=P.kts*[1 -1;-1 1];K2=P.ktl*[1 -1;-1 1];P.Ks=zeros(P.n,P.n);
137 C1=P.cts*[1 -1;-1 1];C2=P.ct1*[1 -1;-1 1];P.Cs=zeros(P.n,P.n);

```

```

137 for i=1:P.sn-1
138     P.Ks(i:i+1,i:i+1)=P.Ks(i:i+1,i:i+1)+K1;
139     P.Cs(i:i+1,i:i+1)=P.Cs(i:i+1,i:i+1)+C1;
140 end
141 for i=P.sn:P.n-1
142     P.Ks(i:i+1,i:i+1)=P.Ks(i:i+1,i:i+1)+K2;
143     P.Cs(i:i+1,i:i+1)=P.Cs(i:i+1,i:i+1)+C2;
144 end
145
146 if P.sn>1
147     P.Ks(1,1)=2*P.kts;P.Cs(1,1)=2*P.cts;
148 else
149     P.Ks(1,1)=P.kts+P.ktl;P.Cs(1,1)=P.cts+P.ctl;
150 end
151 %% Hydrodynamic force damping matrix Cf
152
153 P.Cf=[];
154 for i=1:P.n
155     for j=1:P.n
156         if i>j
157             P.Cf(i,j)=-1;
158         elseif i<j
159             P.Cf(i,j)=1;
160         else
161             P.Cf(i,j)=0;
162         end
163     end
164 end
165 P.Cf=P.Cf*P.Mn*P.v*P.ll;
166 for i=1:P.sn
167     P.Cf(i,i:end)=P.Cf(i,i:end)/P.ll*P.ls;
168     P.Cf(i:end,i)=P.Cf(i:end,i)/P.ll*P.ls;
169 end
170 %% Call function
171 [T,Y] = ode45(@(t,q_n)odefun_secondmodel_nsections_f0(t,q_n,P),tspan,q_0);
172 %% Calculate moments by the output displacements
173 % Form drag and frictional drag
174 P.F=[];P.Ff=[];
175 for i=1:P.sn
176     P.F(i,1)=P.F_amp_s*(P.v).^2;P.Ff(i,1)=P.F_amp_s/1.98*0.037*(P.v).^2;
177 end
178 for i=P.sn+1:P.n
179     P.F(i,1)=P.F_amp_l*(P.v).^2;P.Ff(i,1)=P.F_amp_l/1.98*0.037*(P.v).^2;
180 end
181 % Force Fnc
182 P.Fnc = zeros(P.n,1);
183 P.Fnc(P.n,1)=(1-P.f0)*P.Mn*P.v;
184
185
186 for index = 1:length(Y)
187     for j = 1:P.n
188         if Y(index,j) > 0
189             con(j)=1;
190         else
191             con(j)=-1;
192         end
193     end
194
195
196 % Tip velocity for each section
197 P.Vtip(1)=P.ls*Y(index,P.n+1);
198 if P.sn>1
199     for i=2:P.sn
200         P.Vtip(i)=P.Vtip(i-1)+P.ls*Y(index,i+P.n);
201     end
202     for i=P.sn+1:P.n
203         P.Vtip(i)= P.Vtip(i-1)+P.ll*Y(index,i+P.n);
204     end
205
206 else
207     for i=2:P.n

```

```

208     P.Vtip(i)=P.Vtip(i-1)+P.ll*Y(index,i+P.n);
209     end
210 end
211
212
213 % Force arm for friction drag (armforA)
214 R(1)=0;
215 if P.sn>1
216     for i=2:P.sn+1
217         R(i)=R(i-1)-Y(index,i-1)*P.ls;
218     end
219     for i=P.sn+2:P.n
220         R(i)=R(i-1)-Y(index,i-1)*P.ll;
221     end
222 else
223     R(2)=-Y(index,1)*P.ls;
224     for i=3:P.n
225         R(i)=R(i-1)-Y(index,i-1)*P.ll;
226     end
227 end
228 armforA=zeros(P.n,1);
229
230 if P.sn>1
231     for i=2:P.sn
232         armforA(i)=R(i)+Y(index,i)*(i-1)*P.ls;
233     end
234     for i=P.sn+1:P.n
235         armforA(i)=R(i)+Y(index,i)*(P.sn*P.ls+(i-1-P.sn)*P.ll);
236     end
237 else
238     for i=2:P.n
239         armforA(i)=R(i)+Y(index,i)*(P.ls+(i-2)*P.ll);
240     end
241 end
242
243 % Force arm of form drag and Fnc
244 P.larm(1)=P.ls;
245 if P.sn>1
246     for i=2:P.sn
247         P.larm(i)=P.larm(i-1)+P.ls;
248     end
249     for i=P.sn+1:P.n
250         P.larm(i)=P.larm(i-1)+P.ll;
251     end
252 else
253     for i=2:P.n
254         P.larm(i)=P.larm(i-1)+P.ll;
255     end
256 end
257
258 % Calculate total moment and the moment that produced by each force
259 M_model(index)=sum(P.Ff'.*armforA' - con.*P.F'.*Y(index,1:P.n).^2.*P.larm - ...
260     P.Fnc'.*(P.Vtip + P.v.*Y(index,1:P.n)).*P.larm);
261
262 F_H(index)= sum (P.Ff' + con.*P.F'.*Y(index,1:P.n).^3 + P.Fnc'.*(P.Vtip + ...
263     P.v.*Y(index,1:P.n)).*Y(index,1:P.n));
264
265 F_V(index)= sum (P.Ff'.*Y(index,1:P.n) - con.*P.F'.*Y(index,1:P.n).^2 - ...
266     P.Fnc'.*(P.Vtip + P.v.*Y(index,1:P.n)));
267
268 end
269
270 % Extract maximum moment
271 maxmoment(n)=max(M_model); minmoment(n)=min(M_model);
272
273 % Extract maximum force
274 MaximumHforce(n)=max(F_H);
275 MaximumVforce(n)=max(F_V);
276
277 MinimumHforce(n)=min(F_H);
278 MinimumVforce(n)=min(F_V);
279

```

```
276 vbase(n+1)=vbase(n)+Δ;
277
278 end
279
280 %% graphing
281
282 % moment that contribution ratios
283 figure(1)
284 plot(vbase(1:end-1),maxmoment);hold on; grid minor;
285 plot(vbase(1:end-1),minmoment);
286 title('Moment on the structure');
287 xlabel('Velocity [m/s]')
288 ylabel('Moment [Nm]')
289 ax = gca;
290 ax.FontSize = 14;
291
292 figure(2)
293 plot(vbase(1:end-1),MaximumHforce);hold on; grid minor;
294 plot(vbase(1:end-1),MinimumHforce);
295 title('Horizontal force on the structure');
296 xlabel('Velocity [m/s]')
297 ylabel('Force [N]')
298 ax = gca;
299 ax.FontSize = 14;
300
301 figure(3)
302 plot(vbase(1:end-1),MaximumVforce);hold on; grid minor;
303 plot(vbase(1:end-1),MinimumVforce);
304 title('Vertical force on the structure');
305 xlabel('Velocity [m/s]')
306 ylabel('Force [N]')
307 ax = gca;
308 ax.FontSize = 14;
```

G

Notation and acronyms

- Chapter 1

SVC	Seaweed Value Chain
CO_2	Carbon dioxide
θ	Coordination for the first motion model
φ	Coordination for the second motion model
ODE	Ordinary differential equations

- Chapter 2

USD	United States dollar
A_a	Full frontal area of the individual seaweed frontal thallus
C_d	Drag coefficient
v	unidirectional current velocity

- Chapter 3

D_o, D_i	Outer and inner diameter for seaweed stalks or surrogate tubes
t	Thickness for seaweed leaves or surrogate sheets
w	Width of seaweed and surrogate materials
l	Length of seaweed and surrogate materials
ρ	Density of seaweed or surrogate
m	Mass of seaweed or surrogate
PVC	Polyvinyl chloride (a common raw material for producing synthetic plastic polymer such a pipes)
δ_{max}, h	Deflection and resulting vertical deflection
P	Applied force
J	Flexural rigidity
E	Bending modulus
s	Distance between clamped ends of the sample
I_e, I_r, I_c	Area second moment of inertia for ellipse, rectangular and hollow circular
a, b	Major radius and minor radius for ellipse cross-section

- Chapter 4

EMS	Electro magnetic flow velocity sensor
$v_c(t)$	Generated current velocity
h_1, h_2, h_3, \dots	Depth of each points on surrogate
F_N, F_{Af}	Normal force and axial force
ρ_w	Water density
F_d	Drag force
A	Area
$A(h)$	Project area which is changing with the attack angle α variation
A_{full}	Full thallus area
C_d	Drag coefficient
α, α_n	Attack angles
$(C_D)_{90}$	Drag coefficient when surrogate hanging straight down
C_{HD}	Horizontal drag coefficient
C_{VL}	Vertical drag coefficient
C_f	Frictional drag coefficient
F_D, F_L	Horizontal drag force and vertical drag force
F_{Hf}, F_{Vf}	Horizontal skin frictional drag and vertical skin frictional drag
n	The quantities of attack angles that were taken into account
F_m	The measured force from force sensor

- Chapter 5

DOF	Degrees of freedom
n	The total number of sections of the structures
E	Bending modulus
I	Area second moment of inertia
i	The i^{th} mass block
t	Area second moment of inertia
$\theta_i (\Theta)$	Rotational angle of the i^{th} section (displacement matrix)
$\dot{\theta}_i (\dot{\Theta})$	Line velocity of the i^{th} section (velocity matrix)
$\ddot{\theta}_i (\ddot{\Theta})$	Acceleration of the i^{th} section (acceleration matrix)
x_i, y_i	Coordinate of the i^{th} mass block
\dot{x}_i, \dot{y}_i	Velocities for the i^{th} mass block
m_i, l_i	Mass and length for the i^{th} section
k_{ri}	Rotational stiffness for the i^{th} section
c_{ri}	Viscous damping for the i^{th} section
T_{si}	Kinetic energy for the i^{th} mass block
T_s, V_s	Kinetic energy and potential energy for the structure
F_{Ln}, F_{Dn}	Horizontal and vertical component of form drag on the n^{th} section
F_{Hfn}, F_{Vfn}	Horizontal and vertical component of skin frictional drag on the n^{th} section
F_{Nsn}, F_{Asn}	Normal and axial hydrostatic forces on the n^{th} section
F_{Hi}, F_{Vi}	Total horizontal and vertical forces on the i^{th} mass block
D	Diameter of the cross-section
$(C_D)_0$	Maximum drag coefficient when $\theta = 0^\circ$
$Q_i (Q)$	Generated moments on the i^{th} mass block (moment matrix)
a_{hi}, a_{vi}	Arms for horizontal and vertical forces
L	Lagrangian
q	Coordination in the configuration space of the system
\dot{q}	Generalized velocities that comes from the time derivatives of the generalized coordinates
J	Inertia matrix
C	Damping matrix
K_1, K_2	Stiffness matrices

- Chapter 6

φ (Φ)	Rotational angle (displacement matrix)
$\dot{\varphi}$ ($\dot{\Phi}$)	Line velocity for the i^{th} mass block (velocity matrix)
$\ddot{\varphi}$ ($\ddot{\Phi}$)	Acceleration on the i^{th} mass block (acceleration matrix)
T_{s2}, V_{s2}	Kinetic energy and potential energy for the structure in model 2
T_f	Kinetic energy of surrounding flow in model 2
T	Total kinetic energy in model 2
M_{ni}, M_{Li}	Added mass of the i^{th} section in the normal and longitude direction
D	Diameter of tube
F_{Ni}, F_{Ai}	Pressure drag forces in normal direction and frictional drag forces in axial direction for small angles
F_{nc}	Nonconservative inviscid hydrodynamic force on tip
f	Streamline parameter
V_i	Volume of the i^{th} section
Δm_i	Difference of structure mass and fluid mass
Q_i (Q)	Generated moments on the i^{th} mass block (moment matrix)
J	Inertia matrix
k_{ri}	Rotational stiffness for the i^{th} section
c_{ri}	Viscous damping for the i^{th} section
K_s	Stiffness matrix
C_s	Viscous damping matrix
K_f	Stiffness matrix generated by inviscid hydrodynamic force
C_f	Viscous damping matrix caused by generated hydrodynamic force

- Chapter 7

DNS	Dutch North Sea
F_{nc}	Nonconservative inviscid hydrodynamic force on tip

Bibliography

- [1] K. Anastasakis and A. B. Ross. Hydrothermal liquefaction of the brown macro-alga laminaria saccharina: effect of reaction conditions on product distribution and composition. *Bioresource technology*, 102(7): 4876–83, 2011. ISSN 0960-8524.
- [2] T. B. Benjamin. Dynamics of a system of articulated pipes conveying fluid. i. theory. *Proceedings of the Royal Society of London. Series A, Mathematical and Physical Sciences*, 261(1307):457–486, 1961. ISSN 0080-4630.
- [3] I. Brown. Diary of a fashion mister. URL <http://diaryofafashionmister.blogspot.nl>.
- [4] B. H. Buck and C. M. Buchholz. The offshore-ring: A new system design for the open ocean aquaculture of macroalgae. *Journal of Applied Phycology*, 16(5):355–368, 2004. ISSN 0921-8971.
- [5] B. H. Buck and C. M. Buchholz. Response of offshore cultivated laminaria saccharina to hydrodynamic forcing in the north sea. *Aquaculture*, 250(3):674–691, 2005. ISSN 0044-8486.
- [6] I. K. Chung, J. Beardall, S. Mehta, D. Sahoo, and S. Stojkovic. Using marine macroalgae for carbon sequestration: a critical appraisal. *Journal of Applied Phycology*, 23(5):877–886, 2011. ISSN 0921-8971.
- [7] Kurakon Foods Corporation. Different parts of wakame and it's characteristics. URL http://www.kurakonusa.com/wakame/different_parts_of_wakame_and_its_characteristics.html.
- [8] M. Denny. Predicting physical disturbance: Mechanistic approaches to the study of survivorship on wave-swept shores. *Ecological Monographs*, 65(4):371–418, 1995. ISSN 0012-9615.
- [9] Merriam-Webster Dictionary. *The Merriam-Webster Dictionary*. Merriam-Webster, Incorporated, 2006.
- [10] M. Dobrynin, G. Gayer, A. Pleskachevsky, and H. Günther. Effect of waves and currents on the dynamics and seasonal variations of suspended particulate matter in the north sea. *Journal of Marine Systems*, 82(1):1–20, 2010. ISSN 0924-7963.
- [11] R. Dvorak, F. Freistetter, and J. Kurths. *Chaos and stability in planetary systems*, volume 683. Springer Science & Business Media, 2006.
- [12] F. Fernand, A. Israel, J. Skjermo, T. Wichard, K. R. Timmermans, and A. Golberg. Offshore macroalgae biomass for bioenergy production: Environmental aspects, technological achievements and challenges. *Renewable and Sustainable Energy Reviews*, 75:35–45, 2017. ISSN 1364-0321.
- [13] L. E. Frostick, R. E. Thomas, M. F. Johnson, S. P. Rice, and S. J. McLelland. *Users Guide to Ecohydraulic Modelling and Experimentation: Experience of the Ecohydraulic Research Team (PISCES) of the HYDRALAB Network*. CRC Press, 2014. ISBN 9781315778839.
- [14] B. Gaylord, C. A. Blanchette, and M. W. Denny. Mechanical consequences of size in wave-swept algae. *Ecological Monographs*, 64(3):287–313, 1994. ISSN 0012-9615.
- [15] B. Gaylord, M. W. Denny, and M. A. R. Koehl. Flow forces on seaweeds: Field evidence for roles of wave impingement and organism inertia. *The Biological Bulletin*, 215(3):295–308, 2008. ISSN 0006-3185.
- [16] F. C. Groenendijk, P. Bikker, R. Blaauw, W. A. Brandenburg, van den S. W. K. Burg, P. F. H. Harmsen, R. G. Jak, P. Kamermans, van M. M. Krimpen, H. Prins, M. Stuiver, van der A. K. Werf, M. M. Scholl, and J. Wald. *North-Sea-Weed-Chain: sustainable seaweed from the North Sea; an exploration of the value chain*. IMARES, 2016.
- [17] S. F. Hoerner. *Fluid-dynamic drag : theoretical, experimental and statistical information*. Hoerner Fluid Dynamics, 1992. ISBN 9998831636 9789998831636.

- [18] C. L. Hurd. Water motion, marine macroalgal physiology, and production. *Journal of Phycology*, 36(3): 453–472, 2000. ISSN 0022-3646.
- [19] E. K. Hwang, Y. G. Gong, and C. S. Park. Cultivation of a hybrid of free-living gametophytes between *Undaria pinnatifida* and *Undaria pinnatifida*: morphological aspects and cultivation period. *Journal of Applied Phycology*, 24(3):401–408, 2012. ISSN 0921-8971.
- [20] R. E. Kalaba and F. E. Udawadia. Lagrangian mechanics, gauss' principle, quadratic programming, and generalized inverses: new equations for non-holonomically constrained discrete mechanical systems. *Quarterly of Applied Mathematics*, 52(2):229–241, 1994. ISSN 0033-569X.
- [21] M. N. Khan, J. Y. Cho, M. C. Lee, J. Y. Kang, N. G. Park, H. Fujii, and Y. K. Hong. Isolation of two anti-inflammatory and one pro-inflammatory polyunsaturated fatty acids from the brown seaweed *Undaria pinnatifida*. *Journal of Agricultural and Food Chemistry*, 55(17):6984–8, 2007. ISSN 0021-8561.
- [22] M. A. R. Koehl. Seaweeds in moving water: form and mechanical function. In *On the economy of plant form and function: proceedings of the Sixth Maria Moors Cabot Symposium, Evolutionary Constraints on Primary Productivity, Adaptive Patterns of Energy Capture in Plants, Harvard Forest, August 1983*. Cambridge [Cambridgeshire]: Cambridge University Press, c1986.
- [23] L. Korzen, A. Abelson, and A. Israel. Growth, protein and carbohydrate contents in *Ulva rigida* and *Gracilaria bursa-pastoris* integrated with an offshore fish farm. *Journal of Applied Phycology*, 28(3):1835–1845, 2016. ISSN 0921-8971.
- [24] J. L. Lagrange. *Mécanique analytique*. Cambridge Univ Press, 2009. ISBN 1108001742 9781108001748.
- [25] Y. Lehahn, K. N. Ingle, and A. Golberg. Global potential of offshore and shallow waters macroalgal biorefineries to provide for food, chemicals and energy: feasibility and sustainability. *Algal Research*, 17: 150–160, 2016. ISSN 2211-9264.
- [26] D. Liu, J. K. Keesing, Z. Dong, Y. Zhen, B. Di, Y. Shi, P. Fearn, and P. Shi. Recurrence of the world's largest green-tide in 2009 in yellow sea, china: *Porphyra yezoensis* aquaculture rafts confirmed as nursery for macroalgal blooms. *Marine pollution bulletin*, 60(9):1423–32, 2010. ISSN 0025-326X.
- [27] H. Maeda, M. Hosokawa, T. Sashima, K. Funayama, and K. Miyashita. Fucoxanthin from edible seaweed, *Undaria pinnatifida*, shows antiobesity effect through ucp1 expression in white adipose tissues. *Biochemical and Biophysical Research Communications*, 332(2):392–397, 2005. ISSN 0006-291X.
- [28] D. J. McHugh. *A guide to the seaweed industry*. FAO fisheries technical paper, 0429-9345 ; 441; FAO fisheries technical paper ; no. 441. Food and Agriculture Organization of the United Nations Rome, 2003. ISBN 9251049580.
- [29] H. Mitchell. *Sweeteners and sugar alternatives in food technology*. Oxford; Ames, Iowa: Blackwell Pub., 2006. ISBN 1405134348 9781405134347.
- [30] J. R. Morison, J. W. Johnson, and S. A. Schaaf. The force exerted by surface waves on piles. *Journal of Petroleum Technology*, 2(05):149–154, 1950.
- [31] M. Neushul, J. Benson, B. W. W. Harger, and A. C. Charters. Macroalgal farming in the sea: water motion and nitrate uptake. *Journal of Applied Phycology*, 4(3):255–265, 1992. ISSN 0921-8971.
- [32] K. J. Niklas. *Plant biomechanics : an engineering approach to plant form and function*. University of Chicago Press, Chicago, 1992. ISBN 0226586308 9780226586304 0226586316 9780226586311.
- [33] L. Nikolaisen, P. Daugbjerg Jensen, K. Svane Bech, J. Dahl, J.; Busk, T. Brødsgaard, M. B. Rasmussen, A. Bruhn, A. B. Bjerre, H. Bangsø Nielsen, K. R. Albert, P. Ambus, Z. Kádár, S. Heiske, B. Sander, and E. R. Schmidt. Energy production from marine biomass (*Ulva lactuca*). Report PSO Project No. 2008-1-0050, Danish Technological Institute, 2011.
- [34] M. P. Paidoussis. Dynamics of flexible slender cylinders in axial flow part 1. theory. *Journal of Fluid Mechanics*, 26(04):717–736, 1966. ISSN 0022-1120.

- [35] M. P. Païdoussis. *Fluid-structure interactions: slender structures and axial flow*, volume 1. Academic press, 1998.
- [36] M. P. Païdoussis and R. M. Botez. Chaotic dynamics of articulated cylinders in confined axial flow. *Journal of Fluids and Structures*, 7(7):719–750, 1993. ISSN 0889-9746.
- [37] M. Paul and P. Y. T. Henry. Evaluation of the use of surrogate laminaria digitata in eco-hydraulic laboratory experiments. *Journal of Hydrodynamics, Ser.B*, 26(3):374–383, 2014. ISSN 1001-6058.
- [38] M. Paul, P. Y. T. Henry, and R. E. Thomas. Geometrical and mechanical properties of four species of northern european brown macroalgae. *Coastal Engineering*, 84:73–80, 2014. ISSN 0378-3839.
- [39] M. Paul, E. Penning, J. Dijkstra, and M. F. Johnson. Using surrogate organisms in hydraulic research: Guidance on their design and implementation. In *11th International Symposium on Ecohydraulics (ISE 2016)*, page 51. Engineers Australia, 2016.
- [40] C. Peteiro and Ó. Freire. Outplanting time and methodologies related to mariculture of the edible kelp undaria pinnatifida in the atlantic coast of spain. *Journal of Applied Phycology*, 24(6):1361–1372, 2012. ISSN 0921-8971.
- [41] J. L. Pérez-Cirera, J. M. Salinas, J. Cremades, I. Bárbara, A. Granja, A. J. Veiga, and C. Fuertes. Cultivo de undaria pinnatifida (laminariales, phaeophyta) en galicia. *Nova Acta Científica Compostelana (Biología)*, (7):3–28, 1997. ISSN 1130-9717.
- [42] S. Vogel. Drag and flexibility in sessile organisms. *American Zoologist*, 24(1):37–44, 1984. ISSN 0003-1569.
- [43] S. Wang, X. M. Jiang, Q. Wang, H. S. Ji, L. F. Wu, J. F. Wang, and S. N. Xu. Research of specific heat capacities of three large seaweed biomass. *Journal of Thermal Analysis and Calorimetry : An International Forum for Thermal Studies*, 115(3):2071–2077, 2014. ISSN 1388-6150.
- [44] D. I. Weiss, R. N. Shaffer, and B. L. Wise. Mannitol infusion to reduce intraocular pressure. *Archives of Ophthalmology*, 68(3):341–347, 1962. ISSN 0003-9950.
- [45] Wikipedia. Drag (physics) — wikipedia, the free encyclopedia, 2017. URL [https://en.wikipedia.org/w/index.php?title=Drag_\(physics\)&oldid=787777917](https://en.wikipedia.org/w/index.php?title=Drag_(physics)&oldid=787777917).